

**Dynamic Model of a Planetary Gearbox considering Sun Gear Crack  
with Effects of Clearance for Carrier, Planet and Sun Gear Bearings**

by

Xianhua Chen

A thesis submitted in partial fulfillment of the requirements for the degree of

Master of Science

Department of Mechanical Engineering

University of Alberta

© Xianhua Chen, 2020

## ABSTRACT

Planetary gearbox systems are widely used in many heavy machineries such as mining machines, wind turbines, and automobiles. Although well designed, planetary gearboxes may suffer various failure modes, such as sun-gear tooth crack, due to the harsh working environment such as high torque. Gear tooth crack can affect the vibration responses of planetary gearboxes. Furthermore, bearings in planetary gearboxes have clearance, which can also affect the vibration responses.

Dynamic modeling is often used to simulate the vibration responses of planetary gearboxes. Many researchers have studied the effects of different levels of sun-gear tooth crack on the planetary gear set. Considerable literatures focused on bearing clearance in a planetary gearbox. However, very few studies considered sun-gear tooth crack and bearing clearance together to analyse their combined effect on vibration characteristics of planetary gearboxes.

According to the real planetary gear set located in the Reliability Research Lab at the University of Alberta, this thesis simulates the planetary gearbox through dynamic modeling with sun-gear tooth crack and bearing clearance to discuss their comprehensive effects. This thesis assumes that, the crack width is unchanging as the length increases, and the bearing clearance is a constant. As a result, four key works in this thesis are listed as follows:

- (1) The planetary gearbox focused in this thesis has three kinds of bearings, including sun-gear, planet-gear, and carrier bearings, because the ring gear is fixed. Furthermore, 8 cases for the combinations of bearing clearance are discussed in this thesis.
- (2) The sun-gear crack level considered ranges from 0% to 50%, with an increment of 0.5%. The tooth crack can reduce the mesh stiffness. The impulse caused by the tooth crack can

be found in the time domain, and the magnitude of gear mesh frequency is decreased as the tooth crack grows.

- (3) Three kinds of bearing clearances are considered. It is found that the planet-gear bearing clearance increases by 1.6% of the highest value of the displacement sum for the planetary gearbox, which means that the planet-gear bearing clearance could be neglected. However, the effects of carrier and sun-gear bearing clearances cannot be ignored, because the differences can be obviously found in both the time and the frequency domains after considering carrier or sun-gear bearing clearance.

The simulation results have revealed that if the bearing clearance is much smaller than the displacement of its corresponding gear, the clearance does not affect much the dynamic response of this gear. Otherwise, the clearance can increase the displacement of its corresponding gear and also change the dynamic response of other gears. In conclusion, researchers may choose to focus only on the clearance which is bigger than the displacement of its corresponding gear in simulations.

## ACKNOWLEDGEMENTS

I am very grateful to my supervisor, Dr. Ming J. Zuo, for the careful guidance of my master's thesis, which taught me a lot of specific research skills and greatly improved my understanding of academic writing. My sincere gratefulness also goes to the members of my examining committee: Dr. Zhigang Tian and Dr. Albert Vette.

I am grateful to all the members of Reliability Research Lab for their help in my research and life. I am also grateful to all the people who have helped me during the master's program.

Furthermore, I am very grateful to my father and mother. Although they are not in Canada, their support and encouragement are indispensable for my research and life during the past two and a half years.

## PREFACE

The material presented in this thesis is based on original work by Xianhua Chen under the supervision of Dr. Ming J Zuo. The focus of this research is to investigate the effects of bearing clearances on the dynamic response of a planetary gearbox. The topic is a continuation of the PhD work of Dr. Xihui Liang who is a former member of Dr. Zuo's research group. Dr. Liang's PhD thesis did not consider the effects of bearing clearance. The improved motion equations on bearing clearance effects to be provided in Chapter 3 are my original work. Dr. Liang's work on meshing stiffness evaluation, dynamic modeling of planetary gearboxes, crack modeling, and generation of dynamic responses is referenced and utilized in my thesis work.

Dr. Liang has provided me with the Matlab code for meshing stiffness evaluation, which is used in Section 4.1 of this thesis. Dr. Liang has also provided the Matlab code for dynamic modeling to generate the displacement signals of the planetary gearbox, which is used in Section 4.2 of this thesis. I have made necessary modifications and additions to these Matlab codes to consider the effects of bearing clearances.

When the bearing clearances for the sun gear, all planet gears, and the ring gear are considered simultaneously, the research results are documented as Case 8 in Section 4.5.1 of this thesis. These results have been submitted as the following conference paper:

- Xianhua Chen, Xingkai Yang, Ming J. Zuo, and Zhigang Tian, "Dynamic model of a planetary gearbox considering sun gear crack with effects of clearance for carrier, planet, and sun gear bearings," The 9th Asia-Pacific International Symposium on Advanced Reliability and Maintenance Modelling (APARM 2020), Vancouver, British Columbia, Canada, August 20-23, 2020. Accepted May 15, 2020 for conference presentation.

For this conference paper, Dr. Ming J. Zuo contributed in conceptualization, review & editing, and providing resources while co-authors Mr. Xingkai Yang and Dr. Zhigang Tian provided comments and suggestions and helped editing the paper.

# TABLE OF CONTENTS

<b>Chapter 1 Introduction.....</b>	<b>1</b>
1.1. Planetary Gearboxes .....	2
1.2. Failure Modes of Planetary Gearboxes.....	5
1.3. Dynamic Modeling .....	6
1.4. Research Objectives.....	7
<b>Chapter 2 Fundamentals of Gearbox Dynamic Modeling and Literature</b>	
<b>Review .....</b>	<b>8</b>
2.1. Planetary Gearboxes .....	8
2.2. Reported Studies on Dynamic Modeling of Planetary Gearboxes considering Sun Gear tooth Crack and Bearing Clearances .....	16
2.2.1. Damage Modeling of Gear Crack.....	17
2.2.2. The operating environment of a planetary gearbox .....	24
2.3. Summary.....	27
<b>Chapter 3 Structure of the Planetary Gearbox and its Dynamic Model</b>	
<b>Considering Sun Gear Crack and Bearing Clearance.....</b>	<b>29</b>
3.1. Introduction of the Planetary Gearbox System.....	29
3.2. Gear Crack Modeling.....	35
3.3. Bearing Clearance Modeling .....	37
3.4. Motion Equations in Dynamic Model .....	40
3.5. Summary.....	44
<b>Chapter 4 Effect of the Bearing Clearance for the Dynamic Response .....</b>	<b>46</b>
4.1. Mesh Stiffness with Sun Gear Tooth Crack .....	47

4.2. Case 1: Dynamic Modeling without Bearing Clearance .....	52
4.3. Dynamic Modeling with only One Type of Bearing Clearance .....	61
4.3.1. Case 2: Planet-Gear Bearing Clearance.....	61
4.3.2. Case 3: Sun-Gear Bearing Clearance .....	69
4.3.3. Case 4: Carrier Bearing Clearance .....	75
4.3.4. Summary.....	81
4.4. Dynamic Modeling with Two Types of Bearing Clearance .....	82
4.4.1. Case 5: Sun-Gear and Planet-Gear Bearing Clearance.....	82
4.4.2. Case 6: Planet-Gear and Carrier Bearing Clearance.....	86
4.4.3. Case 7: Sun-Gear and Carrier Bearing Clearance .....	90
4.4.4. Summary.....	95
4.5. Dynamic Modeling with Three Types of Bearing Clearance .....	96
4.5.1. Case 8: Sun-Gear, Planet-Gear, and Carrier Bearing Clearances.....	96
4.5.2. Summary.....	100
4.6. Summary and Conclusion.....	101
<b>Chapter 5 Summary and Future Work.....</b>	<b>104</b>
5.1. Summary.....	104
5.2. Future work.....	105
<b>Appendix .....</b>	<b>107</b>
<b>Bibliography .....</b>	<b>110</b>

## LIST OF TABLES

Table 2.1 Parameters about dynamic model of the planetary gearbox .	14
Table 3.1 Number of teeth and the reduction ratio of each gearbox in the test rig.	31
Table 3.2 Parameters of two carrier bearings and planet gear bearings for the two-stage planetary gearboxes.	33
Table 3.3 Clearance for carrier bearing based on Timken document .	35
Table 3.4 Clearance for planet gear bearing based on NTN document .	35
Table 3.5 Crack levels and length.	37
Table 3.6 Parameters setting of the modeled planetary gearbox.	38

## LIST OF FIGURES

Figure 1.1 Planetary gearbox including four planet gears with the ring gear fixed. ....	4
Figure 1.2 Bearing with clearance .....	4
Figure 1.3 Tooth (a) crack (b) pitting (c) chipped.....	5
Figure 1.4 A spring mass system. ....	6
Figure 1.5 Displacement of spring when (a) $k = 0\text{N/cm}$ , (b) $k = 0.5\text{N/cm}$ . ....	7
Figure 2.1 Two coordinate systems for a planetary gearbox: (a) the fixed coordinate system; (b) the rotating coordinate system. ....	9
Figure 2.2 Dynamic model of the planetary gearbox .....	13
Figure 2.3 Dynamic response of the carrier for a healthy planetary gearbox with rotating coordinate system .....	16
Figure 2.4 Cracked tooth model .....	20
Figure 2.5 Mesh stiffness of sun-planet 1 for healthy (0%) and 50% tooth crack gear. ....	23
Figure 2.6 Non-linear model for the bearing. ....	25
Figure 2.7 Coordinate system for carrier and planet gear .....	26
Figure 2.8 The relationship between bearing force and relative displacement. ....	27
Figure 3.1 Planetary gearbox test rig in RRL, University of Alberta . ....	30
Figure 3.2 The structure of real planetary gearbox system. ....	32
Figure 3.3 The installation diagram of the stages one and two planetary gearboxes.....	32
Figure 3.4 Location and structure of bearings. ....	32
Figure 3.5 The structure of the roller bearing with the tapered bore. ....	33
Figure 3.6 The sun-gear tooth crack modeling . ....	36
Figure 3.7 Length and width propagation (a) model, (b) the related scenario .....	36
Figure 3.8 Lumped parameter model of the planetary gear set.....	38
Figure 4.1 Planetary gearbox with four planet gears. ....	48
Figure 4.2 Meshing stiffness of (a) ring-planet 1, (b) ring-planet 2, (c) ring-planet 3, and (d) ring-planet 4 .....	48
Figure 4.3 Meshing stiffness of sun-planet 1 with (a) 0%, (b) 10%, (c) 20%, (d) 30%, (e) 40%, and (f) 50% sun-gear tooth crack.....	50
Figure 4.4 Meshing stiffness of sun-planet 2 with (a) 0%, (b) 10%, (c) 20%, (d) 30%, (e) 40%, and (f) 50% sun-gear tooth crack.....	50

Figure 4.5 Meshing stiffness of sun-planet 3 with (a) 0%, (b) 10%, (c) 20%, (d) 30%, (e) 40%, and (f) 50% sun-gear tooth crack.....	51
Figure 4.6 Meshing stiffness of sun-planet 4 with (a) 0%, (b) 10%, (c) 20%, (d) 30%, (e) 40%, and (f) 50% sun-gear tooth crack.....	51
Figure 4.7 Vibration displacement signal of each component with a 50% sun-gear crack without clearance. ....	53
Figure 4.8 Vibration displacement signal in the $x_g$ direction with a 50% sun-gear crack without clearance. ....	54
Figure 4.9 Vibration signal of the planetary gearbox in the $x_g$ direction with (a) 0%, (c) 10%, (e) 20%, (g) 30%, (i) 40%, and (k) 50% sun-gear tooth cracks; in the $y_g$ direction with (b) 0%, (d) 10%, (f) 20%, (h) 30%, (j) 40%, and (l) 50% sun-gear tooth cracks.....	55
Figure 4.10 Different locations of tooth crack at (a) 0.07 s, (b) 0.47 s, (c) 0.84 s, (d) 1.24 s, (e) 1.64 s, (f) 2.04 s, (g) 2.44 s, and (h) 2.84 s. ....	56
Figure 4.11 Schematic diagram of displacement decomposition when $t = 0.47s$ .....	57
Figure 4.12 Vibration signal of the planet gear with a 50% sun-gear crack without clearance in (a) the $x_g$ direction and (b) the $y_g$ direction. ....	58
Figure 4.13 Frequency spectrum in $x_g$ direction with (a) 0%, (c) 10%, (e) 20%, (g) 30%, (i) 40%, and (k) 50% sun-gear tooth crack; and in $y_g$ direction with (b) 0%, (d) 10%, (f) 20%, (h) 30%, (j) 40%, and (l) 50% sun-gear tooth crack.....	60
Figure 4.14 (a) RMS and (b) kurtosis of the vibration signal for the planetary gearbox with 0%, 10%, 20%, 30%, 40%, and 50% crack levels. ....	61
Figure 4.15 Schematic diagram of relative displacement between the planet gear and the carrier. ....	62
Figure 4.16 Relative displacement between the carrier and (a, b) planet 1, (c, d) planet 2, (e, f) planet 3, and (g, h) planet 4 with 0% and 50%. ....	63
Figure 4.17 Simulated results of the displacement differential $l$ for carrier–planet 1 considering no clearance with (a) 0% and (c) 50% crack levels; considering planet-gear bearing clearance with (b) 0% and (d) 50% crack levels.....	63
Figure 4.18 Vibration displacement signal of each component with a 50% sun-gear crack with a planet-gear bearing clearance.....	64

Figure 4.19 Vibration displacement signal in the $x_g$ direction with a 50% sun-gear crack without clearance. ....	65
Figure 4.20 Vibration signal of the planetary gearbox in the $x_g$ direction with (a) 0%, (c) 10%, (e) 20%, (g) 30%, (i) 40%, and (k) 50% sun-gear tooth crack; in the $y_g$ direction with (b) 0%, (d) 10%, (f) 20%, (h) 30%, (j) 40%, and (l) 50% sun-gear tooth crack considering the planet-gear bearing clearance. ....	67
Figure 4.21 Frequency spectrum in the $x_g$ direction with (a) 0%, (c) 10%, (e) 20%, (g) 30%, (i) 40%, and (k) 50% sun-gear tooth crack; in the $y_g$ direction with (b) 0%, (d) 10%, (f) 20%, (h) 30%, (j) 40%, and (l) 50% sun-gear tooth crack.....	68
Figure 4.22 (a) RMS and (b) kurtosis of the planetary gearbox vibration signal with 0%, 10%, 20%, 30%, 40%, and 50% crack level considering the planet-gear bearing clearance. ....	69
Figure 4.23 Schematic diagram of the relative displacement for the sun gear. ....	69
Figure 4.24 Relative displacement of the sun gear (a, c) without a bearing clearance for 0% and a 50% crack level and (b, d) with a sun-gear bearing clearance for 0% and 50% crack levels....	70
Figure 4.25 Vibration displacement of each component with a 50% sun-gear crack with a sun-gear bearing clearance.....	71
Figure 4.26 Vibration signal of the planetary gearbox in the $x_g$ direction with (a) 0%, (c) 10%, (e) 20%, (g) 30%, (i) 40%, and (k) 50% sun-gear tooth crack; in the $y_g$ direction with (b) 0%, (d) 10%, (f) 20%, (h) 30%, (j) 40%, and (l) 50% sun-gear tooth crack, considering a sun-gear bearing clearance. ....	72
Figure 4.27 Frequency spectrum in the $x_g$ direction with (a) 0%, (c) 10%, (e) 20%, (g) 30%, (i) 40%, and (k) 50% sun-gear tooth crack; in the $y_g$ direction with (b) 0%, (d) 10%, (f) 20%, (h) 30%, (j) 40%, and (l) 50% sun-gear tooth crack.....	73
Figure 4.28 (a) RMS and (b) kurtosis of the vibration signal for the planetary gearbox with 0%, 10%, 20%, 30%, 40%, and 50% crack level considering the sun-gear bearing clearance. ....	74
Figure 4.29 Relative displacement of the carrier. ....	75
Figure 4.30 Relative displacement of the carrier (a, c) without a bearing clearance for 0% and 50% crack levels and (b, d) with a carrier bearing clearance for 0% and 50% crack levels. ....	76
Figure 4.31 Vibration displacement signal of each component with a 50% sun-gear crack with a carrier bearing clearance. ....	77

Figure 4.32 Vibration signal of the planetary gearbox in the  $x_g$  direction with (a) 0%, (c) 10%, (e) 20%, (g) 30%, (i) 40%, and (k) 50% sun-gear tooth crack; in the  $y_g$  direction with (b) 0%, (d) 10%, (f) 20%, (h) 30%, (j) 40%, and (l) 50% sun-gear tooth crack considering a carrier bearing clearance. .... 78

Figure 4.33 Frequency spectrum in the  $x_g$  direction with (a) 0%, (c) 10%, (e) 20%, (g) 30%, (i) 40%, and (k) 50% sun-gear tooth crack; in the  $y_g$  direction with (b) 0%, (d) 10%, (f) 20%, (h) 30%, (j) 40%, and (l) 50% sun-gear tooth crack. .... 79

Figure 4.34 (a) RMS and (b) kurtosis of the vibration signal for the planetary gearbox with 0%, 10%, 20%, 30%, 40%, and 50% crack level considering the carrier bearing clearance. .... 80

Figure 4.35 (a) RMS and (b) kurtosis of the vibration signal for the planetary gearbox with 0%, 10%, 20%, 30%, 40%, and 50% crack levels for Cases 1, 2, 3, and 4. .... 82

Figure 4.36 Vibration signal of the planetary gearbox in the  $x_g$  direction with (a) 0%, (c) 10%, (e) 20%, (g) 30%, (i) 40%, and (k) 50% sun-gear tooth crack; in the  $y_g$  direction with (b) 0%, (d) 10%, (f) 20%, (h) 30%, (j) 40%, and (l) 50% sun-gear tooth crack considering the sun-gear and planet-gear bearing clearances. .... 84

Figure 4.37 Frequency spectrum in the  $x_g$  direction with (a) 0%, (c) 10%, (e) 20%, (g) 30%, (i) 40%, and (k) 50% sun-gear tooth crack; in the  $y_g$  direction with (b) 0%, (d) 10%, (f) 20%, (h) 30%, (j) 40%, and (l) 50% sun-gear tooth crack. .... 85

Figure 4.38 (a) RMS and (b) kurtosis of the vibration signal for the planetary gearbox with 0%, 10%, 20%, 30%, 40%, and 50% crack level considering the sun-gear and planet-gear bearing clearances. .... 86

Figure 4.39 Vibration signal of the planetary gearbox in the  $x_g$  direction with (a) 0%, (c) 10%, (e) 20%, (g) 30%, (i) 40%, and (k) 50% sun-gear tooth crack; in the  $y_g$  direction with (b) 0%, (d) 10%, (f) 20%, (h) 30%, (j) 40%, and (l) 50% sun-gear tooth crack considering planet-gear and carrier bearing clearances. .... 88

Figure 4.40 Frequency spectrum in the  $x_g$  direction with (a) 0%, (c) 10%, (e) 20%, (g) 30%, (i) 40%, and (k) 50% sun-gear tooth crack; in the  $y_g$  direction with (b) 0%, (d) 10%, (f) 20%, (h) 30%, (j) 40%, and (l) 50% sun-gear tooth crack. .... 89

Figure 4.41 (a) RMS and (b) kurtosis of the vibration signal for the planetary gearbox with 0%, 10%, 20%, 30%, 40%, and 50% crack level considering the carrier and planet-gear bearing clearances. .... 90

Figure 4.42 Vibration displacement signal of each component with a 50% sun-gear crack with the carrier and sun-gear bearing clearances. ....	91
Figure 4.43 Vibration signal of the planetary gearbox in the $x_g$ direction with (a) 0%, (c) 10%, (e) 20%, (g) 30%, (i) 40%, and (k) 50% sun-gear tooth crack; in the $y_g$ direction with (b) 0%, (d) 10%, (f) 20%, (h) 30%, (j) 40%, and (l) 50% sun-gear tooth crack considering the sun-gear and carrier bearing clearances. ....	92
Figure 4.44 Frequency spectrum in the $x_g$ direction with (a) 0%, (c) 10%, (e) 20%, (g) 30%, (i) 40%, and (k) 50% sun-gear tooth crack; in the $y_g$ direction with (b) 0%, (d) 10%, (f) 20%, (h) 30%, (j) 40%, and (l) 50% sun-gear tooth crack. ....	94
Figure 4.45 (a) RMS and (b) kurtosis of the vibration signal for the planetary gearbox with 0%, 10%, 20%, 30%, 40%, and 50% crack level considering the carrier and sun-gear bearing clearances. ....	95
Figure 4.46 (a) RMS and (b) kurtosis of the vibration signal for the planetary gearbox with 0%, 10%, 20%, 30%, 40%, and 50% crack level for Cases 1, 5, 6, and 7. ....	96
Figure 4.47 Vibration signal of the planetary gearbox in the $x_g$ direction with (a) 0%, (c) 10%, (e) 20%, (g) 30%, (i) 40%, and (k) 50% sun-gear tooth crack; in the $y_g$ direction with (b) 0%, (d) 10%, (f) 20%, (h) 30%, (j) 40%, and (l) 50% sun-gear tooth crack considering the carrier, sun-gear, and planet-gear bearing clearances. ....	98
Figure 4.48 Frequency spectrum in the $x_g$ direction with (a) 0%, (c) 10%, (e) 20%, (g) 30%, (i) 40%, and (k) 50% sun-gear tooth crack; in the $y_g$ direction with (b) 0%, (d) 10%, (f) 20%, (h) 30%, (j) 40%, and (l) 50% sun-gear tooth crack. ....	99
Figure 4.49 (a) RMS and (b) kurtosis of the vibration signal for the planetary gearbox with 0%, 10%, 20%, 30%, 40%, and 50% crack level considering the carrier, sun-gear, and planet-gear bearing clearances. ....	100
Figure 4.50 (a) RMS and (b) kurtosis of the vibration signal for the planetary gearbox with 0%, 10%, 20%, 30%, 40%, and 50% crack level for Cases 1, 5, 6, and 7. ....	101

# Chapter 1

## Introduction

Engineering systems are widely used in meeting the needs of our society. These include transportation systems such as railways, trucks, automobiles and conveyor belts, communication systems such as cellular networks and the internet, and power generation systems such as wind farms and hydro stations. The reliable and cost-effective operation of such systems is critical to our society. For example, from 75% to 90% of the investment costs for 750 kW wind turbines might be the operations and maintenance [1].

Mechanical systems play critical roles in many engineering systems. For example, engines are used to provide power for vehicles, ships, and airplanes. Bearings are used to provide the needed support to rotating shafts. Gearboxes are often needed to regulate speed and torque for the target applications. For the gear set in a wind turbine, Barszcz and Randall [2] analysed a real case of a wind turbine failure caused by a tooth crack. The accident can result in technical failures, financial losses or human injuries [3]. Thus, ensuring the reliable operation of engineering systems and mechanical systems is a must.

Many methods have been developed by engineers and researchers to ensure the reliable operation of engineering systems. These include reliability design and analysis tools such as fault tree analysis (FTA) [4, 5], failure modes [6], effects and criticality analysis (FMECA) [7, 8], system reliability theory [9], design approaches for reliability [10], and maintenance optimization strategies [11, 12]. More recent tools focus on condition monitoring [13, 14], signal processing [15, 16], and machine learning methods [17, 18] that utilize condition monitoring data such as vibration data to assess the health condition of running mechanical systems.

To develop condition monitoring tools for reliability assurance of mechanical systems, researchers have analysed machine dynamics [19], seeded faults into laboratory mechanical systems [20], developed effective signal processing methods [21], and utilized degradation prediction approaches [22]. This thesis aims to make further advances in the category of dynamic

modeling of a mechanical system, namely, the planetary gearboxes. We will introduce the target study object planetary gearboxes next.

## 1.1. Planetary Gearboxes

Planetary gearboxes have been widely used in various industries and heavy machineries. For example, in the wind turbines, planetary gearboxes are used to increase the speed of the rotor of the generator driven by rotating blades. In general, a planetary gear set consists of a ring gear, a sun gear, and a few planet gears, which contact with two gears (sun and ring gears) simultaneously. This structure gives the planetary gearbox advantages of large load capacity, compact size, and high-power density. Among the three types of gears used in a planetary gearbox (see Figure 1.1), depending on which ones are rotating while the system is in operation, they can be divided into the following categories.

### #1 Fixed ring gear:

When the ring gear is fixed, the output rotational direction is the same as the input shaft.

(a) Sun gear is the input device, while the carrier is the output. The gearbox is used to decrease speed and increase torque. Applications of this structure include mining applications where a motor drives the sun gear and the planet carrier drives a slow moving conveyor belt [23].

(b) The carrier is used as the input and the sun gear is used as the output. This gearbox increases speed and decreases torque. Applications of this structure include wind turbines where the slow rotating blades driven by natural wind drive the carrier, and the high speed from the sun gear transfers to the generator [2].

### #2 Fixed sun gear:

When the sun gear is fixed, the output rotational direction is also the same as the input shaft.

(c) The ring gear is input, and carrier is the output. This gearbox reduces the speed, and the effectiveness of this speed reduction is lower than type (a) described above. Automatic transmissions in automobiles use this structure to reduce the speed from engine satisfying the desired travel speed for a car [24, 25]. The output speed from carrier is about 70% of the input speed from ring gear in an automatic transmission [24].

(d) The carrier is input and ring is the output. Cars use this structure to achieve high driving speed where the carrier links the engine, and ring gear outputs high speed to the wheel [24, 25]. This structure is commonly used for overdriving because the output speed is about 1.4 times of input speed [24].

### #3 Fixed carrier

When the carrier is fixed, the obvious change is that the output rotational direction is opposite to the input, whatever the input and output devices are.

(e) Sun gear is the input and ring gear is the output. This gearbox reduces the input speed. Automatic transmissions use this structure to achieve car reversing due to the opposite direction between the input and output shaft [24, 25].

(f) Ring gear is the input and sun gear is the output. This structure is usually used with another planetary gearbox structure (e) discussed above in the automatic transmission [24]. The final output speed is about 38% of the input, and the final direction is same as the input direction [24].

In a car, there may be two planetary gearboxes, including a front gear set and a rear gear set [24]. In the front gear set, when the ring gear is input, the output is sun gear with the carrier fixed (f) or the output is the carrier with sun gear fixed (c). In the rear gear set, when the sun gear is the input, the output is the ring gear with carrier fixed (e). When the rear gear set fixes the sun gear with the carrier as the input, the car can overdrive, which means that the output speed is higher than the input speed (d). In conclusion, cars can achieve different speeds due to the combinations of different planetary gearbox structures [24].

An example planetary set including 4 planet gears with the ring gear non-rotating is shown in Figure 1.1. The names of the key components of this gear set are provided in the figure. We will focus on this type of planetary gearbox, as we have a test rig in our lab that is of this structure where the sun gear is the input and the carrier is the output. This structure is used in the mining conveyor belt system and automatic transmissions mentioned above.

In the planetary gearbox, bearings are used to support rotating parts. There are bearings supporting the sun gear shaft, each of the four planet gear shafts, and the carrier shaft. The

components of a rolling element bearing include the inner race, the outer race, rollers, and the cage holding many rollers, as shown in Figure 1.2.

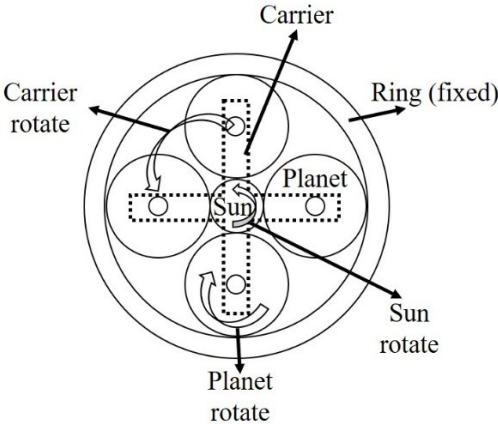


Figure 1.1 Planetary gearbox including four planet gears with the ring gear fixed.

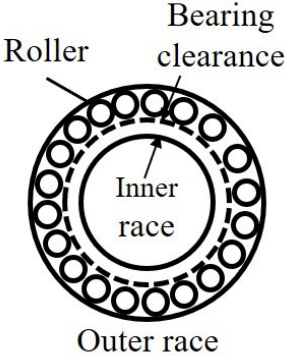


Figure 1.2 Bearing with clearance [26].

A bearing as an assembly has the following main components: inner race, rollers, the cage holding the rollers, and the outer race. The inner race is attached to a shaft that rotates together with the inner race inside the bearing. As shown in Figure 1.2, the rollers may not be simultaneously in contact with both the outer race and the inner race. This means that there may be a gap of non-zero value before the inner race gets in touch with a roller which in turn gets in touch with the outer race. This gap is called the bearing clearance. Many researchers have considered this clearance in the dynamic model of planetary gearbox only when gearboxes are healthy [26, 27]. However, no studies have reported the effects of clearance when the gearbox has

faults. This thesis considers the bearing clearance for the sun gear, the carrier, and four planet gears. The detail will be given in Chapter 2.

## 1.2. Failure Modes of Planetary Gearboxes

Although the planetary gearbox is powerful, it is vulnerable to some failure modes because of the complex structure and the high loads. Tooth crack, tooth pitting and tooth chip may develop that affect the health of a planetary gearbox. Tooth crack as shown in Figure 1.3(a) is commonly caused by excessive loads transmitted and the material fatigue [28]. Tooth pitting is a failure mode representing pits forming in the tooth surface shown in Figure 1.3(b) caused by the long-term tooth contact. Tooth chip describes the situation when part of a tooth is chipped off as shown in Figure 1.3(c), which is also a common failure mode for gears.

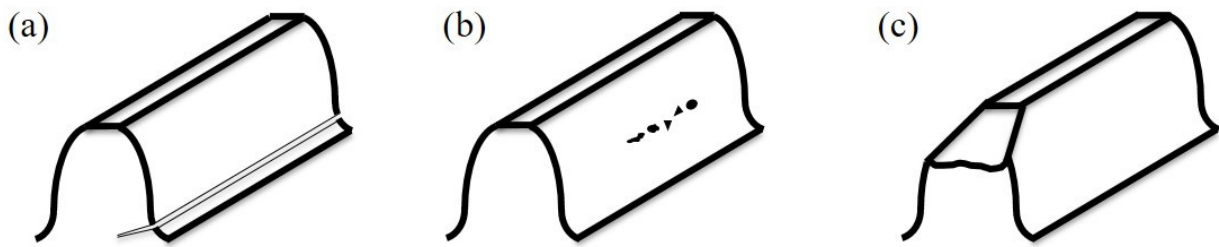


Figure 1.3 Tooth (a) crack (b) pitting (c) chipped.

All these faults are about tooth damage, which is frequently encountered [29]. For example, Gelman et al. [30] reported that gear faults accounted for approximately 60% of gearbox failures. The tooth damage can reduce the strength of the tooth, which seriously decreases the ability and durability of the planetary gearbox [31]. When the ring gear is fixed, the sun gear is an important component to transmit high speed from the input shaft to the carrier through the planet gears in mining conveyor belt mentioned above. The long-term high load operation could trigger tooth crack [28]. Many researchers have focused on the tooth crack in sun gear for a planetary gearbox [32-35]. This thesis targets the planetary gearbox with fixed ring gear, and the input shaft is sun gear due to the structure of gearbox in the lab to be further discussed in Chapter 3. Thus, the planetary gearbox is similar to the mining gearbox application mentioned above. Furthermore, this thesis discusses the effects of bearing clearance for different tooth crack levels in sun gear.

### 1.3. Dynamic Modeling

Dynamic modeling is widely used to simulate the mechanical motions, such as a simple spring mass system shown as Figure 1.4. Unlike experimental research, dynamic modeling uses parameters to simulate the motion trajectory of the spring, rather than using actual measurements. Then, in the dynamic model we can change relevant parameters arbitrarily to simulate the motion for different springs, rather than replacing the springs through operators in physical experiments.

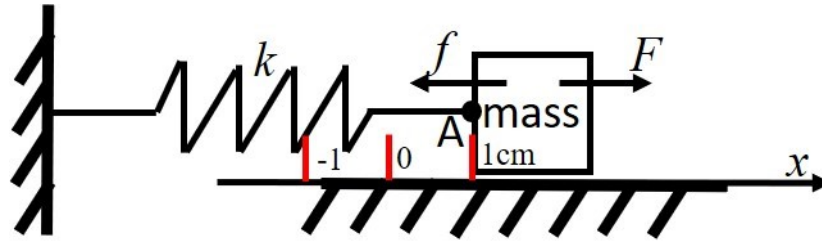


Figure 1.4 A spring mass system.

For example, the motion equation for the spring mass system in Figure 1.4 is

$$m\ddot{x} = \sum F_x = F - kx - f, \quad (1.1)$$

where  $m$  is the mass of the object in Figure 1.4,  $F_x$  is the total force in the  $x$ -direction,  $F$  is the input force,  $f$  denotes the friction force,  $k$  is the stiffness of the spring, while the mass of the spring is assumed as 0, and  $x$  denotes the displacement of the object in the  $x$ -direction.

Dynamic model solves this equation to get the displacement  $x$  through simulating different situations. For example, if we assume the spring system with  $M = 0.1\text{kg}$ ,  $F = 0$ ,  $f = 0$ , initial displacement is 1cm, initial velocity is 0, and two different kinds of  $k$ , including  $k = 1\text{N/cm}$  and  $k = 0.5\text{N/cm}$ . Figure 1.5 illustrates the displacement of the A point shown in Figure 1.4 with different stiffness  $k$  values. From Figure 1.5(a), one period of this signal is about 2s when  $k = 0.5\text{N/cm}$ , while this period changes to about 2.8s when  $k = 0.5\text{N/cm}$  as shown in Figure 1.5(b). The dynamic model can easily get the vibration signal of the spring and analyse its displacement with different spring stiffness  $k$ . This approach is what this thesis uses for the planetary gearbox to be discussed in Chapter 2.

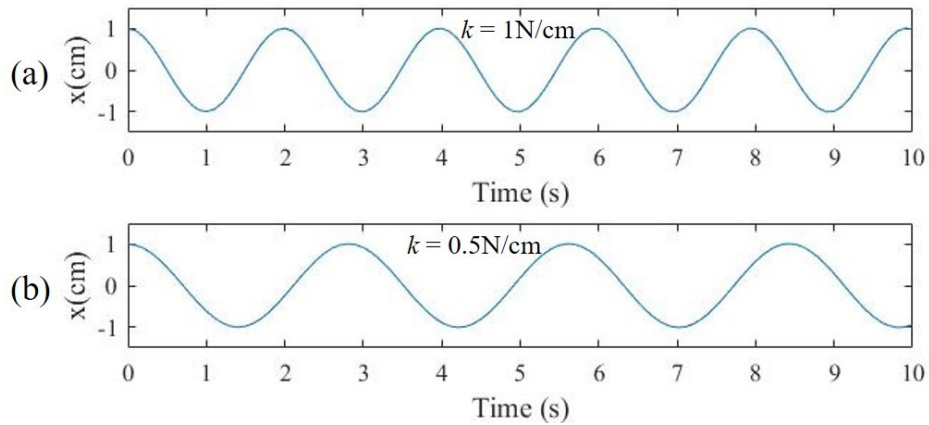


Figure 1.5 Displacement of spring when (a)  $k = 0\text{N/cm}$ , (b)  $k = 0.5\text{N/cm}$ .

In conclusion, there are two advantages for the dynamic model. Firstly, this simulation can save much time on design for a real system, such as spring system, through the computer program. Secondly, the simulation result can help researchers to analyse the status of a real system. For example, dynamic model can simulate a spring mass system. Then, the researchers can analyse the limitation of this spring system, such as the maximum cycle of back and forth movement.

#### 1.4. Research Objectives

As reviewed earlier in this chapter, in the field of dynamic simulation, researchers have considered multiple factors, but not the bearing clearance for a planetary gearbox with a tooth crack in sun gear [32]. Then, the bearing clearance is considered in a healthy planetary gear set [36]. However, the influence of bearing clearances has not been studied adequately for a tooth crack in sun gear. Thus, this thesis will aim at simulating the dynamic responses of a planetary gear set with a tooth crack in the sun gear considering bearing clearances. No physical experimental work is included in this study.

The thesis is organized as follows. Chapter 2 presents the fundamentals of dynamic modeling and provides a detailed literature review of dynamic model for a planetary gearbox with a sun-gear tooth crack and the effect of bearing clearance. Chapter 3 presents the structure of the target planetary gearbox. Chapter 4 presents the effect of bearing clearance for a dynamic model of a planetary gear set with different sun-gear crack levels. Chapter 5 summarizes the results, limitations of the research, and outlines prospects for future studies.

## Chapter 2

### Fundamentals of Gearbox Dynamic Modeling and Literature Review

As we have introduced in Chapter 1, planetary gearboxes are widely used in industrial applications, and critical components in gearboxes degrade as they work in loaded conditions. Researchers have made efforts to understand the motion dynamics, and to develop early fault detection techniques utilizing condition monitoring data. In this thesis, the focus is on modeling the dynamic response of planetary gearboxes as the sun gear experiences crack considering the effects of bearing clearance.

In this chapter, we will first provide the fundamentals of dynamic modeling for gearboxes and then conduct a detailed literature review of dynamic model for a planetary gearbox with a sun-gear tooth crack. Finally, the detailed issues to be addressed in this thesis will be summarized at the end of this chapter.

#### 2.1. Planetary Gearboxes

A single-stage planetary gearbox with the ring gear fixed and four planet gears is discussed. All rotating components are supported by bearings. Thus, there are bearings for the sun gear, each of the planet gears, and the carrier. In this section, we consider an ideal planetary gearbox wherein all components are perfectly healthy, that is, there is no crack at all.

For an ideal planetary gearbox, the basic motion equation is given as follows [32]

$$\mathbf{M}\ddot{\mathbf{q}} + \mathbf{C}\dot{\mathbf{q}} + \mathbf{K}\mathbf{q} + \mathbf{f}_m(t, q) = \mathbf{F}(t), \quad (2.1)$$

where  $\mathbf{q}$  is a displacement vector for components including carrier, ring, sun and planet gears given as

$$\mathbf{q} = \left[ \underbrace{x_c, y_c, u_c}_{\text{Carrier}}, \underbrace{x_r, y_r, u_r}_{\text{Ring}}, \underbrace{x_s, y_s, u_s}_{\text{Sun}}, \underbrace{x_{pn}, y_{pn}, u_{pn}}_{\text{Planet } n \text{ for } n \text{ from } 1 \text{ to } N} \right]^T, \quad (2.2)$$

where the subscripts  $c$ ,  $r$ ,  $s$  and  $pn$  denote carrier, ring gear, sun gear, and the  $n$ th planet gear, respectively, and  $N$  is the number of planet gears in the system. In this thesis, our  $N$  value is 4. This means that the dimension of vector  $\mathbf{q}$  is  $9+3N$ . The  $x$ ,  $y$ , and  $u$  denote the displacement in the  $x$ -axis direction, the  $y$ -axis direction, and the rotation direction.

Based on other investigations [26, 32], one may choose to use one of two possible coordinate systems for dynamic modeling of a planetary gearbox. The first coordinate system is fixed to the ground and we will call it the fixed coordinate system. The second coordinate system is fixed to the carrier. Since the carrier rotates as the system operates, we will call this second coordinate system the rotating coordinate system. These two coordinate systems are shown in Figure 2.1. In this figure,  $x$  denotes the initial direction of the  $x$ -direction when the system starts operation, while  $x'$  is the new  $x$ -direction after the system has operated for a certain length of time. Similarly,  $y$  denotes the initial direction of the  $y$ -direction when the system starts operation, while  $y'$  is the new  $y$ -direction after the system has operated for a certain length of time. In Figure 2.1 (b),  $\beta$  denotes the angle of rotation for carrier.

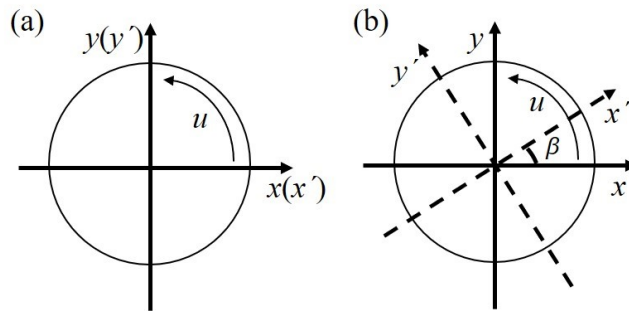


Figure 2.1 Two coordinate systems for a planetary gearbox: (a) the fixed coordinate system; (b) the rotating coordinate system.

In the fixed coordinate system shown in Figure 2.1 (a), the  $x$ -direction is parallel to the ground and does not change with the rotation of any components. In this fixed coordinate system, this  $x$ -direction is perpendicular to the enter line of the shaft. The  $y$ -direction points away from the center of the earth.

In the rotating coordinate system shown in Figure 2.1 (b), the coordinates are fixed to the carrier. Thus, as the carrier rotates, the  $x$ -direction and the  $y$ -direction rotate with the carrier. At the beginning of a simulation run, the initial position of the  $x$ -direction is parallel to the ground and

perpendicular to the center line of the shaft, while the initial position of the  $y$ -direction is pointing away from the center of the earth.

Different researchers have used different coordinate systems. For example, Guo and Parker used the fixed coordinate system (Figure 2.1 (a)) for the carrier, the sun, and the ring gears; and the rotating coordinate system (Figure 2.1 (b)) for each planet gear [26]. Liang et al. used the rotating system (Figure 2.1(b)) for all components including the carrier, the sun, the ring, and the planet gears [32]. In the discussions of this thesis, we will stick to the rotating coordinate system as used by Liang et al. [32].

In Eq. (2.1),  $\mathbf{M}$  is a diagonal matrix representing the masses  $m$  and inertia  $J$  for the carrier, ring, sun and planet gears. Eq. (2.3) shows the expression of  $\mathbf{M}$ . The dimension of matrix  $\mathbf{M}$  is  $(9+3N) \times (9+3N)$ .  $\mathbf{M}(1, 1) = m_c$ ,  $\mathbf{M}(2, 2) = m_c$ ,  $\mathbf{M}(3, 3) = J_c$ ,  $\mathbf{M}(4, 4) = m_r$ ,  $\mathbf{M}(5, 5) = m_r$ ,  $\mathbf{M}(6, 6) = J_r$ ,  $\mathbf{M}(7, 7) = m_s$ ,  $\mathbf{M}(8, 8) = m_s$ ,  $\mathbf{M}(9, 9) = J_s$ ,  $\mathbf{M}(7+3n, 7+3n) = m_{pn}$ ,  $\mathbf{M}(8+3n, 8+3n) = m_{pn}$ ,  $\mathbf{M}(9+3n, 9+3n) = J_{pn}$  for  $n = 1, 2, \dots, N$ , and all other entries of matrix  $\mathbf{M}$  are 0.

$$\mathbf{M} = \text{diag}(\underbrace{m_c, m_c, J_c}_{\text{Carrier}}, \underbrace{m_r, m_r, J_r}_{\text{Ring}}, \underbrace{m_s, m_s, J_s}_{\text{Sun}}, \underbrace{m_{pn}, m_{pn}, J_{pn}}_{\text{Planet } n \text{ for } n \text{ from } 1 \text{ to } N}), \quad (2.3)$$

where the subscripts  $c$ ,  $r$ ,  $s$ , and  $pn$  denote the carrier, the ring, the sun, and the  $n$ th planet gear, respectively. The  $J$  is the mass moment of inertia which is calculated through

$$J = \frac{1}{2} mr^2, \quad (2.4)$$

where  $m$  and  $r$  denote the mass and radius for the carrier, the sun, the planet, or the ring gear. The Eq. (2.4) is used in [32] to get the  $J$  of the carrier, the ring, the sun, and the planet gears.

In Eq. (2.1),  $\mathbf{C}$  is a matrix for bearing damping. The literature [37] describes three kinds of bearing damping. First is generated between the rolling elements such as rollers and their raceway (Figure 2.6). Second is generated through the deformation of rolling bodies. Third is generated between the bearing outer race and the housing; or the inner ring and the shaft. Eq. (2.5) shows the  $\mathbf{C}$  in [32]. The dimension of matrix  $\mathbf{C}$  is  $(9+3N) \times (9+3N)$ .  $\mathbf{C}(1, 1) = c_{cx} + \sum_{n=1}^N c_{pnx}$ ,  $\mathbf{C}(1, 7+3N) = -c_{pnx}$ ,  $\mathbf{C}(2, 2) = c_{cy} + \sum_{n=1}^N c_{pny}$ ,  $\mathbf{C}(2, 8+3N) = -c_{pny}$ ,  $\mathbf{C}(3, 3) = c_{cu} + \sum_{n=1}^N c_{pnu}$ ,  $\mathbf{C}(3, 9+3N) = -c_{pnu}$ ,  $\mathbf{C}(4, 4) = c_{rx}$ ,  $\mathbf{C}(5, 5) = c_{ry}$ ,  $\mathbf{C}(6, 6) = c_{ru}$ ,  $\mathbf{C}(7, 7) = c_{sx}$ ,  $\mathbf{C}(8, 8) = c_{sy}$ ,  $\mathbf{C}(9, 9) = c_{su}$ ,

$\mathbf{C}(7+3N, 1) = \sum_{n=1}^N c_{pnx}$ ,  $\mathbf{C}(7+3N, 7+3N) = -c_{pnx}$ ,  $\mathbf{C}(8+3N, 2) = \sum_{n=1}^N c_{pny}$ ,  $\mathbf{C}(8+3N, 8+3N) = -c_{pny}$ ,  $\mathbf{C}(9+3N, 3) = \sum_{n=1}^N c_{pnu}$ ,  $\mathbf{C}(9+3N, 9+3N) = -c_{pnu}$ , and all other entries of  $\mathbf{C}$  are 0. The matrix  $\mathbf{C}$  is shown in Appendix.

The subscript  $x$ ,  $y$ , and  $u$  represent only the different directions. For the same component, its bearing damping coefficient is the same in the  $x$  and  $y$  directions, that is,  $c_{cx}=c_{cy}=\text{constant}$ ,  $c_{rx}=c_{ry}=\text{constant}$ ,  $c_{sx}=c_{sy}=\text{constant}$ , and  $c_{pnx}=c_{pny}=\text{constant}$ . The  $c_{cu}$ ,  $c_{ru}$ ,  $c_{su}$ , and  $c_{pnu}$  in the literature [32] can be calculated through

$$\begin{aligned} c_{cu} &= \frac{c_{cx}\dot{x}_c \sin(\Psi_n) - c_{cy}\dot{y}_c \cos(\Psi_n)}{\dot{u}_c} \\ c_{ru} &= \frac{c_{rx}\dot{x}_r \sin(\Psi_n) - c_{ry}\dot{y}_r \cos(\Psi_n)}{\dot{u}_r} \\ c_{su} &= \frac{c_{sx}\dot{x}_s \sin(\Psi_n) - c_{sy}\dot{y}_s \cos(\Psi_n)}{\dot{u}_s} \quad , \\ c_{pnu} &= \frac{c_{pnx}\dot{x}_{pn} \sin(\Psi_n) - c_{pny}\dot{y}_{pn} \cos(\Psi_n)}{\dot{u}_{pn}} \end{aligned} \quad (2.5)$$

where the  $\dot{x}$ ,  $\dot{y}$ , and  $\dot{u}$  are the speed in the  $x$ -direction,  $y$ -direction, and  $u$ -direction, the  $\Psi_n$  represents the circumferential angle of the  $n$ th planet. The circumferential angle is the angle between the center of the  $n$ th planet and that of the first planet gear, while this angle for the first planet gear is 0.

In Eq. (2.1),  $\mathbf{K}$  donates a matrix of bearing stiffness which is the resistance to deflection or deformation. The  $k_{cx}=k_{cy}=\text{constant}$ ,  $k_{rx}=k_{ry}=\text{constant}$ ,  $k_{sx}=k_{sy}=\text{constant}$ , and  $k_{pnx}=k_{pny}=\text{constant}$  [32]. Similar to the bearing damping  $\mathbf{C}$ , the dimension of matrix  $\mathbf{K}$  is  $(9+3N) \times (9+3N)$ .  $\mathbf{K}(1, 1) = k_{cx} + \sum_{n=1}^N k_{pnx}$ ,  $\mathbf{K}(1, 7+3N) = k_{pnx}$ ,  $\mathbf{K}(2, 2) = k_{cy} + \sum_{n=1}^N k_{pny}$ ,  $\mathbf{K}(2, 8+3N) = -k_{pny}$ ,  $\mathbf{K}(3, 3) = k_{cu} + \sum_{n=1}^N k_{pnu}$ ,  $\mathbf{K}(3, 9+3N) = -k_{pnu}$ ,  $\mathbf{K}(4, 4) = k_{rx}$ ,  $\mathbf{K}(5, 5) = k_{ry}$ ,  $\mathbf{K}(6, 6) = k_{ru}$ ,  $\mathbf{K}(7, 7) = k_{sx}$ ,  $\mathbf{K}(8, 8) = k_{sy}$ ,  $\mathbf{K}(9, 9) = k_{su}$ ,  $\mathbf{K}(7+3N, 1) = \sum_{n=1}^N k_{pnx}$ ,  $\mathbf{K}(7+3N, 7+3N) = -k_{pnx}$ ,  $\mathbf{K}(8+3N, 2) = \sum_{n=1}^N k_{pny}$ ,  $\mathbf{K}(8+3N, 8+3N) = -k_{pny}$ ,  $\mathbf{K}(9+3N, 3) = \sum_{n=1}^N k_{pnu}$ ,  $\mathbf{K}(9+3N, 9+3N) = -k_{pnu}$ , and all other entries of  $\mathbf{K}$  are 0. The matrix  $\mathbf{K}$  is shown in Appendix. Similar to the matrix  $\mathbf{C}$ , the  $k_{cu}$ ,  $k_{ru}$ ,  $k_{su}$ , and  $k_{pnu}$  can be calculated through [32]

$$\begin{aligned}
k_{cu} &= \frac{k_{cx}x_c \sin(\Psi_n) - k_{cy}y_c \cos(\Psi_n)}{u_c} \\
k_{ru} &= \frac{k_{rx}x_r \sin(\Psi_n) - k_{ry}y_r \cos(\Psi_n)}{u_r} \\
k_{su} &= \frac{k_{sx}x_s \sin(\Psi_n) - k_{sy}y_s \cos(\Psi_n)}{u_s} \\
k_{pnu} &= \frac{k_{pnx}x_{pn} \sin(\Psi_n) - k_{pny}y_{pn} \cos(\Psi_n)}{u_{pn}}
\end{aligned} \tag{2.6}$$

In a planetary gearbox, the carrier contacts two bearings, one is carrier bearing, and another is planet-gear bearing during rotating. Therefore, the **C** and **K** matrix entries are more complex for the carrier and the planet gears than other components shown in Appendix.

During the rotation of the gearbox, sun and ring gears mesh with the planet gears. The vector  $\mathbf{f}_m(t, q)$  in Eq. (2.1) donates this meshing force which acts on two contacting components.  $F_{spn}$  is the force of the sun-planet gear meshing, while  $F_{rpn}$  denotes the force from the ring-planet gear meshing. There is no gear meshing for the carrier, therefore, the force entry for the carrier is 0 in this vector, and the vector  $\mathbf{f}_m(t, q)$  with  $9+3N$  dimensions can be written as

$$\mathbf{f}_m(t, q) = \left[ \underbrace{f_{mcx}, f_{mcy}, f_{mcu}}_{\text{Carrier}}, \underbrace{f_{mrx}, f_{mry}, f_{mru}}_{\text{Ring}}, \underbrace{f_{msx}, f_{msy}, f_{msu}}_{\text{Sun}}, \underbrace{f_{mpnx}, f_{mpny}, f_{mpnu}}_{\text{Planet } n \text{ for } n \text{ from 1 to } N} \right]^T, \tag{2.7}$$

where  $f_{mcx} = f_{mcy} = f_{mcu} = 0$ ,  $f_{mrx} = \sum_{n=1}^N F_{rpn} \cos \Psi_{rn}$ ,  $f_{mry} = \sum_{n=1}^N F_{rpn} \sin \Psi_{rn}$ ,  $f_{mru} = \sum_{n=1}^N F_{rpn}$ ,  $f_{msx} = \sum_{n=1}^N F_{spn} \cos \Psi_{sn}$ ,  $f_{msy} = \sum_{n=1}^N F_{spn} \sin \Psi_{sn}$ ,  $f_{msu} = \sum_{n=1}^N F_{spn}$ ,  $f_{mpnx} = -F_{spn} \cos \Psi_{sn} - F_{rpn} \cos \Psi_{rn}$ ,  $f_{mpny} = -F_{spn} \sin \Psi_{sn} - F_{rpn} \sin \Psi_{rn}$ , and  $f_{mpnu} = F_{spn} - F_{rpn}$ .

According to reference [32],  $\Psi_{sn}$  and  $\Psi_{rn}$  can be calculated by

$$\Psi_{sn} = \frac{\pi}{2} - \alpha + \Psi_n, \tag{2.8}$$

$$\Psi_{rn} = \frac{\pi}{2} + \alpha + \Psi_n, \tag{2.9}$$

where  $\alpha$  is the pressure angle of a gear pair. The pressure angle is the angle between the tooth face and the gear wheel tangent which is constant in planetary gearbox.

In Eq. (2.1),  $\mathbf{F}(t)$  is the vector for other forces (except bearing and meshing force mentioned above) acted in the carrier, the ring, the sun, and the planet gears in  $x, y,$  and  $u$  directions. The force includes internal force such as centrifugal force and external force such as input force, and the detail is shown in Eq. (2.11). The dimension of this force vector is  $9+3N$ .

$$\mathbf{F}(t) = \left\{ \underbrace{f_{cx}, f_{cy}, f_{cu}}_{\text{Carrier}}, \underbrace{f_{rx}, f_{ry}, f_{ru}}_{\text{Ring}}, \underbrace{f_{sx}, f_{sy}, f_{su}}_{\text{Sun}}, \underbrace{f_{pnx}, f_{pny}, f_{pnu}}_{\text{Planet } n \text{ for } n \text{ from } 1 \text{ to } N} \right\}, \quad (2.10)$$

In this thesis, the ring gear is fixed, while input force as constant is acted in the sun gear. The rotating speed of each component is also constant. Therefore, there is no acceleration in rotating direction. This means  $\ddot{u}_c = \ddot{u}_r = \ddot{u}_s = \ddot{u}_{pn} = 0$ . Furthermore, the  $\mathbf{M}, \mathbf{C}, \mathbf{K}, \mathbf{f}_m(t, q),$  and  $\mathbf{F}(t)$  are provided through [32], because the planetary gearbox is the same as [32]. The planetary gearbox has four planet gears and the ring gear is fixed. Then, all the components including the carrier, the sun, the planet, and the ring gears use the rotating coordinate system based on the carrier mentioned above. The real system will introduce in Chapter 3.

Many researchers have studied the dynamic model for a planetary gearbox [31, 36, 38]. Figure 2.2 shows a basic dynamic model [32]. As we mentioned earlier, [32] uses the rotating coordinate system for all components. The parameters defined earlier in this section are summarized in Table 2.1.

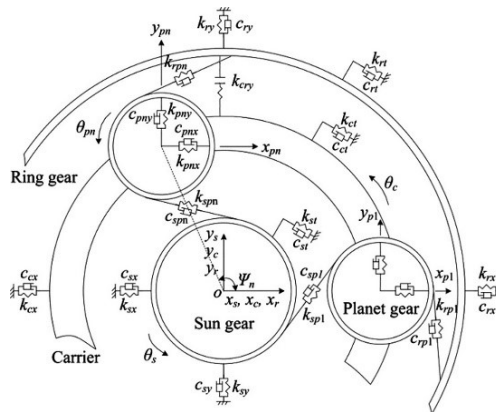


Figure 2.2 Dynamic model of the planetary gearbox [32].

Table 2.1 Parameters about dynamic model of the planetary gearbox [32].

Notation	Description
$c_{sx}, c_{sy}$	Damping coefficient of the sun gear bearing in the $x, y$ directions, and torsional direction ( $c_{sx} = c_{sy}$ )
$c_{rx}, c_{ry}$	Damping coefficient of the ring gear bearing in the $x, y$ directions, and the torsional direction ( $c_{rx} = c_{ry}$ )
$c_{cx}, c_{cy}$	Damping coefficient of the carrier bearing in the $x, y$ directions, and the torsional direction ( $c_{cx} = c_{cy}$ )
$c_{pnx}, c_{pny}$	Damping coefficient of the $n$ th planet in the $x, y$ directions ( $c_{pnx} = c_{pny}$ )
$c_{spn}, c_{rpn}$	Mesh damping coefficient of the $n$ th sun-planet, the ring-planet ( $c_{spn} \neq c_{rpn}$ )
$k_{sx}, k_{sy}$	Stiffness of the sun gear bearing in the $x, y$ directions, and the torsional direction ( $k_{sx} = k_{sy}$ )
$k_{rx}, k_{ry}$	Stiffness of the ring gear bearing in the $x, y$ directions, and the torsional direction ( $k_{rx} = k_{ry}$ )
$k_{cx}, k_{cy}$	Stiffness of the carrier bearing in the $x, y$ directions, and the torsional direction ( $k_{cx} = k_{cy}$ )
$k_{pnx}, k_{pny}$	Stiffness of the $n$ th planet bearing in the $x, y$ directions ( $k_{pnx} = k_{pny}$ )
$k_{spn}, k_{rpn}$	Mesh stiffness of the $n$ th sun-planet, the ring-planet ( $k_{spn} \neq k_{rpn}$ )
$x_r, y_r$	Displacement of the ring gear in the $x, y$ directions
$x_c, y_c$	Displacement of the carrier in the $x, y$ directions
$x_s, y_s$	Displacement of the sun gear in the $x, y$ directions
$x_{pn}, y_{pn}$	Displacement of the $n$ th planet in the $x, y$ directions
$\theta_s, \theta_c, \theta_{pn}$	Rotation angle of the sun gear, the carrier, and the $n$ th planet
$\Psi_n$	Circumferential angle of the $n$ th planet ( $\Psi_n = \text{constant}$ )

Dynamic model can simulate the vibration of gears through the motion equation. Compared with the spring-mass system mentioned in Chapter 1, the planetary gearbox dynamic model has three motion equations ( $x$ -direction,  $y$ -direction, and  $u$ -direction) for each component such as a

gear or the carrier. For example, the equations of motion in the  $x$ -direction, the  $y$ -direction, and the  $u$ -direction for the sun gear as presented in [32] are given below, respectively.

$$\begin{aligned}
m_s \ddot{x}_s + c_{sx} \dot{x}_s + k_{sx} x_s + \sum_n F_{spn} \cos \Psi_{sn} &= m_s x_s \Omega^2 + 2m_s \dot{y}_s \Omega + m_s y_s \dot{\Omega}, \\
m_s \ddot{y}_s + c_{sy} \dot{y}_s + k_{sy} y_s + \sum_n F_{spn} \sin \Psi_{sn} &= m_s y_s \Omega^2 - 2m_s \dot{x}_s \Omega - m_s x_s \dot{\Omega}, \\
(J_s / r_s) \ddot{\theta}_s + \sum_n F_{spn} &= T_i / r_s,
\end{aligned} \tag{2.11}$$

where  $m_s$  is the mass of the sun gear,  $F_{spn}$  represents the dynamic force of the  $n$ th sun-planet gear mesh,  $\Omega$  is the rotation speed of the carrier,  $J_s$  is the mass moment of inertia for the sun gear,  $T_i$  is the input torque of the sun gear,  $r_s$  is the radius of the sun gear, and  $\Psi_{sn}$  can be calculated through Eq. (2.8). Note that  $c_{sx} = c_{sy}$ ,  $k_{sx} = k_{sy}$  as it was pointed out earlier.

On the right side of Eq. (2.11),  $m_s x_s \Omega^2$  is the centrifugal force which appears to act on all rotating objects in Newtonian mechanics,  $2m_s \dot{y}_s \Omega$  is the Coriolis force which is a fictitious force acting on a mass with a rotating reference frame, and  $m_s y_s \dot{\Omega}$  is the Euler force which is the fictitious tangential force appearing in the objects with variation of angular velocity. In a rotational planetary gearbox, these forces are considered in [32, 39]. The planetary gearbox system in this thesis is similar to the system used in another study [32]. Furthermore, they both use rotating coordinate system. Therefore, this thesis considers the same forces in right side of motion equations [32].

For a healthy planetary gearbox, we mean that there is no damage in any component and the clearances in bearings are 0. For such a healthy system, Figure 2.3 shows the dynamic response of carrier in a model with rotating coordinate system [32].  $x_c$  and  $y_c$  denote the vibration signal of the carrier in  $x$  and  $y$ -directions with the rotating coordinate system in a healthy planetary gearbox system.

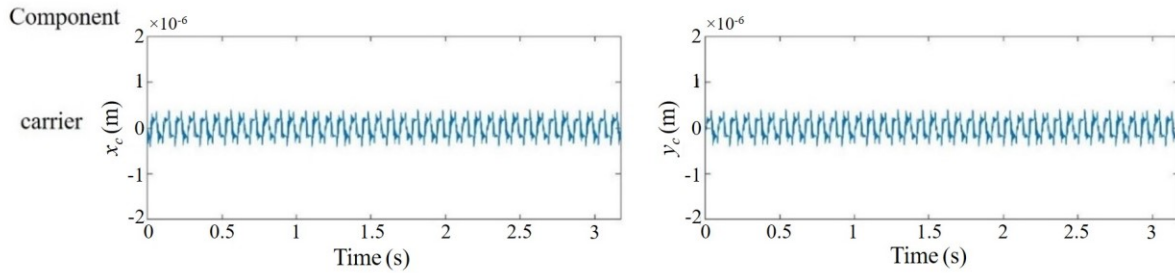


Figure 2.3 Dynamic response of the carrier for a healthy planetary gearbox with rotating coordinate system [32].

When a damage is introduced into a component of the gearbox, the vibration signal generated can be different. Damages could be sun gear tooth crack. When different operating factors are considered, the generated vibration system can also be different. For example, one such operating factor may be whether a bearing has clearance or not. Simulating different crack levels can help scientists to study the effect of crack for each component or the gearbox. Considering different environmental factors can improve the dynamic model close to the real system. These will be discussed in the next Section.

## 2.2. Reported Studies on Dynamic Modeling of Planetary Gearboxes considering Sun Gear tooth Crack and Bearing Clearances

In this section, we divide our review into two aspects: damage modeling and environment modeling. Damage modeling aims to address the health condition such as crack, pitting, and misalignment of the equipment. As mentioned in Chapter 1, the tooth crack is easily triggered by long-term high load operation. In this system, the sun gear as the input gear meshes with four planet gears and the load in sun gear could trigger the tooth crack. Therefore, this thesis focuses on sun gear tooth crack.

Environment modeling aims to consider the operating environment such as bearing clearances and lubricating conditions. As mentioned in Chapter 1, the bearings used in planetary gearbox has clearances. The bearing as an important component supports gears rotating in the gearbox. The clearance allows in-plane translation for connected components which means it affects the tooth wedging [26]. Therefore, this thesis focuses on the bearing clearance which significantly affect the vibration response for a planetary gearbox.

### 2.2.1. Damage Modeling of Gear Crack

The common understanding of the effects of damages in moving parts such as gears is the change in the meshing stiffness. If a crack or pitting occurs on a gear tooth, the meshing stiffness of the tooth will be compromised, when it goes into the meshing. The meshing stiffness is reflected in the  $F_{spn}$  and  $F_{rpn}$  symbols in Eq. (2.7) as introduced earlier. Thus, the dynamic equations introduced earlier can be used to study the effects of critical-component damages in the gearbox system.

Gear faults are caused by high service load, inappropriate operating conditions, and simple fatigue [40]. Gelman et al. [30] pointed about 60% of the gearbox faults is in the gear and the tooth damage including crack, pitting, and chipped are the main proportion. In a planetary gearbox, the sun gear contacts multiple planet gears which can increase the tooth damage on the sun gear [31]. Furthermore, the sun gear is an important transmission device which transmit the input torque into planetary gearbox, when the ring gear is fixed. Thus, a tooth crack on the sun gear can influence the effectiveness of a planetary gearbox. Liang et al. pointed out that a tooth crack can reduce the mesh stiffness [41]. Therefore, researchers evaluated this influence of a sun-gear tooth crack for a planetary gearbox through the mesh stiffness [28, 41, 42].

Mesh stiffness plays an important role in the dynamic modeling, because the final product of dynamic model is the vibration signal of the planetary gearbox; the primary excitation of this vibration is due to contact with the mesh stiffness variation [43]. When the gear meshes in a single stage planetary gearbox, there are two types of gear pairs including sun-planet and planet-ring.

Two approaches for evaluation of mesh stiffness are the finite element method (FEM) and the analytical method (AM) [40, 41, 44, 45]. First, the sun-planet, as well as the external-external gear mesh, is discussed in many researches with FEM [46-48] and AM [41, 49]. Second, the FEM [50] and AM [34, 51] are used to evaluate the mesh stiffness of planet-ring, as well as the external-internal gear.

FEM can be carried out using simulation software such as ANSYS which models the teeth around the contacting area. The teeth are divided into finite small parts called elements. The number and shape of elements affect the accuracy of mesh stiffness. FEM depends on how the elements in a model are generated.

In planetary gearbox, Kawalec et al. analysed the spur and helical gears by FEM [52]; Tsai et al. researched the plastic spur gears through FEM evaluation [53]; Jian et al. compared different topologies for coaxial magnetic gears using the 3D FEM [54], and Ramamurti et al. developed a FEM for the three-dimensional stress of spur and bevel gears [55]. Furthermore, the FEM is also used to evaluate the mesh stiffness of the gear with tooth crack. Chaair et al. researched the influence of spur gear tooth crack for gear-mesh stiffness [28]; Xue and Howard analysed the torsional vibration signal for the planetary gearbox fault detection, where the FEM was used to simulate the mesh stiffness for gear tooth damage [56], and Chen et al. considered the tooth root crack evaluated by FEM for the planetary gear set with flexible ring gear rim [57].

On the other hand, analytical method only analyses the composition of mesh stiffness and their equations. For example, the mesh stiffness includes Hertzian contact, bending, axial, and shear stiffness in analysis, while each stiffness has its own equation. Then, these compositions of mesh stiffness can calculate following equation to get the mesh stiffness of the gear. Therefore, AM depends on the number of compositions of mesh stiffness and their equations.

In planetary gearbox, Yang and Lin [58] analysed the dynamic of meshing gears through potential energy method for the gear pair without tooth damage. Different from the non-damage mesh stiffness, Tian et al. [49] studied the vibration signal of a gear set with three different gear tooth faults including chipped, cracked, and broken tooth. Furthermore, according to many researches, potential energy method is a mature method; for example, Yang and Lin [58] considered the Hertzian contact stiffness, bending stiffness, and axial compressive stiffness for the potential energy method which is the AM. Then, Tian et al. [49] proposed this method to calculate the shear stiffness. Furthermore, Liang et al. [34] considered the mesh stiffness of planetary gearbox with fixed ring gear. Thus, the mesh stiffness in potential energy method includes Hertzian contact, bending, axial, and shear stiffness.

As mentioned above, the advantage of FEM is that the result of FEM is close to actual gear-mesh with high accuracy model. However, the higher accurate deformations of involute transition curve mean more time on simulation. Furthermore, a variety of parameters such as tolerances, element choice, and mesh density make FEM complicated, because these data significantly affect the accuracy of FEM [34]. For example, if the mesh density is not reasonable, there is a discretization error in FEM which can cause the inaccurate response spectrum [59].

Different from FEM, investigators only need the equations of mesh stiffness in AM, rather than using finite element model. Except the complex modeling process, the AM saves time compared with FEM [42]. The accuracy of AM is based on the equations; therefore, if the equations are not suitable, the result accuracy of AM is lower than FEM. However, the AM is a useful and suitable method in dynamic modeling of planetary gearbox approved by many researches.

Ambarisha et al. [45] compared the analytical and finite element models for the planetary gearbox without tooth crack. The response from the FEM and AM have a strong agreement through a series of complex nonlinear behaviors for the planetary gear set [45]. Many researchers used AM to evaluate the mesh stiffness [32, 58, 60]. Furthermore, a fault diagnosis of a planetary gearbox usually evaluates many different crack levels through AM as reported in the literature. For example, Liang et al. and Liu et al. analysed the planetary gearbox with 10% (0.78 mm) and 50% (0.39 mm) sun-gear tooth crack [32, 61]. Wu et al. analysed a gear tooth crack from 0% to 81% with an increment of 1% [62]. Furthermore, different crack levels can be easily simulated by Eq. (2.12) to (2.17).

In this thesis, we plan to consider the range of crack levels going from 0 to 50% with an increment of 0.5%. Although FEM is a powerful method for gear mesh stiffness. It requires much time to simulate the mesh stiffness of gear with a tooth crack from 0 to 50%. Compared with FEM, AM is a simple and effective method to evaluate the gear mesh stiffness [41]. Thus, analytical method (AM) is used to evaluate the gear mesh stiffness for a planetary gearbox in this thesis.

We are providing fundamental equations of the AM approach when the gear tooth crack is considered. The potential energy method used in this thesis is based on the model in other researches [34, 41]. The Hertzian contact stiffness  $k_h$ , bending stiffness  $k_b$ , shear stiffness  $k_s$ , axial compressive stiffness  $k_a$ , a sun-gear tooth crack, and the fixed ring gear are considered in this thesis. There are two types of gear pair including external-external (sun-planet) and external-internal (planet-ring). For these two different types, the  $k_h$  from the result derived by Yang and Sun [63] is

$$k_h = \frac{\pi EL}{4(1-\nu^2)}, \quad (2.12)$$

where  $E$ ,  $L$  and  $\nu$  denote Young's modulus, tooth width, and Poisson's ratio, respectively. Furthermore, there are two different mesh type. First, single-tooth-pair mesh stiffness [41] is calculated by

$$k_t = \frac{1}{\frac{1}{k_h} + \frac{1}{k_{b1}} + \frac{1}{k_{s1}} + \frac{1}{k_{a1}} + \frac{1}{k_{b2}} + \frac{1}{k_{s2}} + \frac{1}{k_{a2}}}, \quad (2.13)$$

where the subscript 1 and 2 denote the sun and the planet gear, respectively. Second, double-tooth-pair mesh stiffness [41] is calculated by

$$k_t = k_{t1} + k_{t2} = \sum_{i=1}^2 \frac{1}{\frac{1}{k_{h,i}} + \frac{1}{k_{b1,i}} + \frac{1}{k_{s1,i}} + \frac{1}{k_{a1,i}} + \frac{1}{k_{b2,i}} + \frac{1}{k_{s2,i}} + \frac{1}{k_{a2,i}}}, \quad (2.14)$$

where  $i = 1$  or  $2$  for the first or the second pair of meshing teeth.

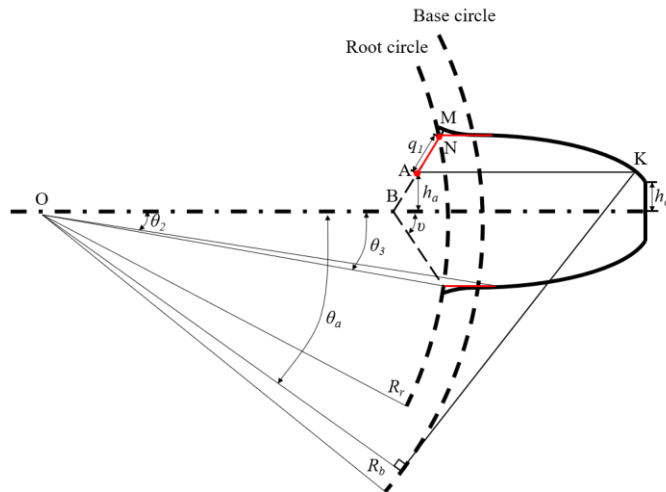


Figure 2.4 Cracked tooth model [41].

Figure 2.4 is based on the cracked tooth model developed by Liang et al. [41]. The  $q_1$  is the crack length from the point  $N$  to point  $A$ . The line segment  $MN$  is interpreted as the initial notch which is not considered as crack length [41]. In this figure, we can see that the crack is modeled as a straight line growing from the root of the gear tooth following an angle denoted by symbol  $\nu$  growing deeper into the gear body. In Figure 2.4,  $h_a$  denotes the distance form the crack end point  $A$  to the tooth central line,  $h_o$  is the half roof chordal tooth thickness,  $\theta_a$  is the angle corresponding to the force action point  $K$ , and  $\theta_l$  is calculated by

$$\theta_1 = \theta - \frac{\pi}{2Z_1} - \tan \alpha + \alpha$$

$$+ \tan \left[ \arccos \frac{Z_1 \cos \alpha}{\sqrt{(Z_2 - 2)^2 + (Z_2 - Z_1)^2 - 2(Z_2 - 2)(Z_2 - Z_1) \cos(\alpha - \arccos \frac{N_2 \cos \alpha}{N_2 - 2})}} \right], \quad (2.15)$$

where  $\theta$  is the rotational angel of the gear,  $\alpha$  denotes the pressure angle,  $Z_1$  and  $Z_2$  represent the number of teeth for the input and output gears when two gears contact each other, respectively.

When  $\theta_l > \theta_a$ , the equation of bending and shear stiffness of the cracked is given as follow [41]

$$k_b = \int_{\theta_3}^{\theta_r} \frac{12 \sin \theta \left[ \frac{Z \cos \theta_0}{Z - 2.5} - (\cos \theta + \cos \theta_3 - \cos \theta_r - \frac{q_1}{R_r} \cos \nu) \cos \theta_1 \right]^2}{EL(\sin \theta_3 + \sin \theta - \frac{q_1}{R_r} \sin \nu)^3} d\theta$$

$$+ \frac{4 \left[ 1 - \frac{(Z - 2.5) \cos \theta_1 \cos \theta_3}{Z \cos \theta_0} \right]^3 - 4(1 - \cos \theta_1 \cos \theta_2)^3}{EL \cos \theta_1 (2 \sin \theta_2 - \frac{q_1}{R_b} \sin \nu)^3}, \quad (2.16)$$

$$+ \int_{-\theta_a}^{\theta_2} \frac{12 \{ 1 + \cos \theta_1 [(\theta_2 - \theta) \sin \theta - \cos \theta] \}^2 (\theta_2 - \theta) \cos \theta}{EL \left[ \sin \theta_2 - \frac{q_1}{R_b} \sin \nu + \sin \theta + (\theta_2 - \theta) \cos \theta \right]^3} d\theta$$

$$+ \int_{-\theta_1}^{-\theta_a} \frac{3 \{ 1 + \cos \theta_1 [(\theta_2 - \theta) \sin \theta - \cos \theta] \}^2 (\theta_2 - \theta) \cos \theta}{2EL \left[ \sin \theta + (\theta_2 - \theta) \cos \theta \right]^3} d\theta$$

$$\begin{aligned}
k_s = & \int_{\theta_3}^{\theta_r} \frac{2.4(1+\nu) \cos^2 \theta_1 \sin \theta}{EL(\sin \theta_3 + \sin \theta - \frac{q_1}{R_r} \sin \nu)^3} d\theta \\
& + \frac{2.4(1+\nu) \cos^2 \theta_1 (\cos \theta_2 - \frac{Z-2.5}{Z \cos \theta_0} \cos \theta_3)}{EL(2 \sin \theta_2 - \frac{q_1}{R_b} \sin \nu)^3} , \\
& + \int_{-\theta_a}^{\theta_2} \frac{2.4(1+\nu)(\theta_2 - \theta) \cos \theta \cos^2 \theta_1}{EL[\sin \theta_2 - \frac{q_1}{R_b} \sin \nu + \sin \theta + (\theta_2 - \theta) \cos \theta]} d\theta \\
& + \int_{-\theta_1}^{-\theta_a} \frac{1.2(1+\nu)(\theta_2 - \theta) \cos \theta \cos^2 \theta_1}{EL[\sin \theta + (\theta_2 - \theta) \cos \theta]} d\theta
\end{aligned} \tag{2.17}$$

where  $\theta_2$ ,  $\theta_3$ , and  $\nu$  denote the different angle shown in the Figure 2.4,  $q_1$  is the length of crack on the sun gear,  $\nu$  is the Poisson's ratio for the gear,  $Z$  is the number of planet gears in a planetary gearbox,  $R_r$  and  $R_b$  are the root circle and base circle.

When the  $\theta_1 \leq \theta_a$ , the equation of bending and shear stiffness of the cracked is given as follow [41]

$$\begin{aligned}
k_b = & \int_{\theta_3}^{\theta_r} \frac{12 \sin \theta \left[ \frac{Z \cos \theta_0}{Z-2.5} - (\cos \theta + \cos \theta_3 - \cos \theta_r - \frac{q_1}{R_r} \cos \nu) \cos \theta_1 \right]^2}{EL(\sin \theta_3 + \sin \theta - \frac{q_1}{R_r} \sin \nu)^3} d\theta \\
& + \frac{4 \left[ 1 - \frac{(Z-2.5) \cos \theta_1 \cos \theta_3}{Z \cos \theta_0} \right]^3 - 4(1 - \cos \theta_1 \cos \theta_2)^3}{EL \cos \theta_1 (2 \sin \theta_2 - \frac{q_1}{R_b} \sin \nu)^3} , \\
& + \int_{-\theta_1}^{\theta_2} \frac{12 \{ 1 + \cos \theta_1 [(\theta_2 - \theta) \sin \theta - \cos \theta] \}^2 (\theta_2 - \theta) \cos \theta}{EL[\sin \theta_2 - \frac{q_1}{R_b} \sin \nu + \sin \theta + (\theta_2 - \theta) \cos \theta]^3} d\theta
\end{aligned} \tag{2.18}$$

$$\begin{aligned}
k_s = & \int_{\theta_3}^{\theta_r} \frac{2.4(1+\nu) \cos^2 \theta_1 \sin \theta}{EL(\sin \theta_3 + \sin \theta - \frac{q_1}{R_r} \sin \nu)^3} d\theta \\
& + \frac{2.4(1+\nu) \cos^2 \theta_1 (\cos \theta_2 - \frac{Z-2.5}{Z \cos \theta_0} \cos \theta_3)}{EL(2 \sin \theta_2 - \frac{q_1}{R_b} \sin \nu)^3} \\
& + \int_{-\theta_1}^{\theta_2} \frac{2.4(1+\nu)(\theta_2 - \theta) \cos \theta \cos^2 \theta_1}{EL[\sin \theta_2 - \frac{q_1}{R_b} \sin \nu + \sin \theta + (\theta_2 - \theta) \cos \theta]} d\theta
\end{aligned} \tag{2.19}$$

When the ring gear is fixed, the gear mesh frequency  $\omega_m$  (Hz) from the reference [64] is

$$\omega_m = Z_s Z_r \Omega_s / (Z_s + Z_r), \tag{2.20}$$

where  $\Omega_s$  (rad/s) is the rotating speed of the sun gear.  $Z$  is the number of teeth, while the subscript  $s$  and  $r$  denote the sun and the ring gears.

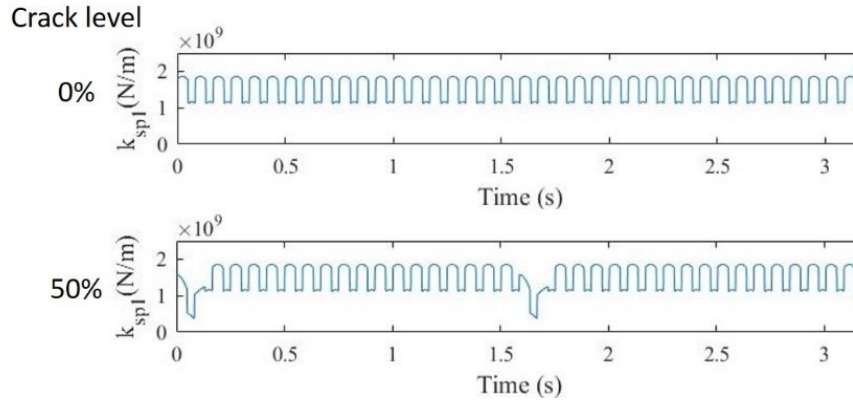


Figure 2.5 Mesh stiffness of sun-planet 1 for healthy (0%) and 50% tooth crack gear.

The motion equations from Eqs. (2.1) to (2.10) can be used for healthy planetary gearboxes and/or tooth-crack planetary gearboxes. As shown in Chapter 1, the tooth crack can reduce the strength of the tooth which affects the mesh stiffness. Various sun-gear crack levels mean different mesh stiffness. For example, Figure 2.5 shows the mesh stiffness for a healthy gear and a gear with 50% tooth crack [41]. The  $k_{sp1}$  is the mesh stiffness for sun-planet 1. It is obvious to see that the tooth crack decreases the mesh stiffness. The dynamic model given in Figure 2.2 and Eq. (2.11)

can simulate the dynamic responses under different tooth crack levels in the sun gear for a planetary gearbox through different mesh stiffness values.

Similar to the sun-planet mesh stiffness, the equations for ring-planet mesh stiffness can be found in [34]. In conclusion, a tooth crack in the sun gear can affect the effectiveness of a planetary gearbox or cause economic losses. Using Eq. (2.12) to (2.19) from prior researches [34, 41, 64], the mesh stiffness of a planetary gear set can be evaluated in this thesis.

### **2.2.2. The operating environment of a planetary gearbox**

For a planetary gearbox, the operating environment could be complex. For example, there is a lubrication system that is used to reduce the friction in the system and make it run smoothly. The bearing clearance may be present in the system after installation. All these environments affect the vibration signals. It is hard to consider all operating environments for a dynamic model of planetary gearbox. Considering a significant variable and treating other factors constant, is a useful method to analyse the effects of one special factor. In this thesis, the special factor is the bearing clearance; therefore, other environmental factors are kept un-changed in the planetary gearbox. The input torque is constant, and the lubrication system is assumed to be healthy. In other words, this thesis focuses only on the bearing forces for motion equations in a planetary gearbox with the potential of having sun gear tooth crack.

In dynamic modeling, the  $\mathbf{C}\dot{\mathbf{q}}$  and  $\mathbf{K}\mathbf{q}$  in Eq. (2.1) are influenced by bearing factors [32].  $\mathbf{C}$  is the matrix of bearing damping and  $\mathbf{K}$  is the matrix of bearing stiffness. Here,  $\dot{\mathbf{q}}$  means the speed of displacement for carrier, ring, sun, and planet gears, while  $\mathbf{q}$  denotes the displacement of carrier, ring, sun, and planet gears mentioned in Eq. (2.2). The bearing clearance condition changes the expression of  $\mathbf{C}\dot{\mathbf{q}}$  and  $\mathbf{K}\mathbf{q}$  and motion equations such as Eq. (2.11) given in Chapter 4. When the ring gear is fixed, there are three types of bearings in the planetary gear set: carrier bearing, sun-gear, and planet-gear bearing. This thesis focuses on the spherical roller bearing. Many documents from the manufacturer show that there is clearance in this roller bearing [30, 65].

Bearing clearance has been considered in much research. First, Kahraman and Singh [66] researched the nonlinear dynamic for the geared rotor bearing system. Kahraman [64] generated a nonlinear dynamic model to analyse the load for a planetary gearbox. Then, Guo and Parker [26] also analysed the nonlinear dynamic modeling for a spur gear involving tooth wedging. Guo and

Parker [36] observed the effect of bearing clearance in the planetary gearbox for a helicopter. Guo et al. [27] investigated the effect of bearing clearance in the planetary gear set for a wind turbine.

Although much research are about the effect of the bearing clearance in the dynamic model for a planetary gear set, crack tooth analysis of a planetary gearbox considering the bearing clearance is limited. These references [26, 36, 67] were about the planetary gearbox with perfect gears.

The information about clearance of bearings in the planetary gear set to be studied in this thesis is found through the manufacturers [65, 68]. When the bearing clearance is considered, the linear bearing model will change to the non-linear model [26]. In the non-linear model, there are inner and outer races [26]. The inner race contacts the gear shaft and the outer race contacts the shell and rollers. These rollers are simplified to the spring system shown in Figure 2.6. If the displacement of the inner race is bigger than the bearing clearance, these springs will be compressed and generate force to the inner race. Otherwise, the springs will not be compressed and there is no force from the bearing.

Figure 2.7 illustrates the coordinate system for carrier and planet gears used in [26]. As mentioned above, the carrier uses the fixed coordinate system and planet gears use the rotating coordinate system in [26]. The sun gear uses  $x$  and  $y$ , while the planet gear uses  $\xi$  and  $\eta$  because of the different coordinate system. Although the motion equations are focused on [32] with the rotating coordinate system for all components, there are no equations for bearing clearance. Therefore, we will introduce the equations for bearing clearance in [26] with rotating and fixed coordinate system in this Chapter. Then, the equations of bearing clearance for only the rotating coordinate system, based on coordinate system transformation, will be shown in Chapter 3.

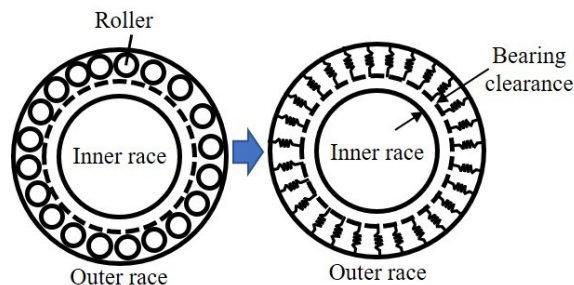


Figure 2.6 Non-linear model for the bearing.

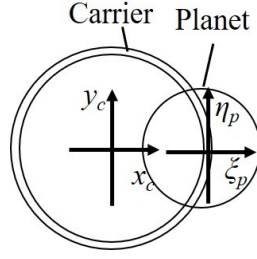


Figure 2.7 Coordinate system for carrier and planet gear [26].

The relative displacement  $\delta_{cp}$  between the carrier and the planet [26] is followed

$$\delta_{cp} = [(x_c \cos \alpha + y_c \sin \alpha - \xi_p)^2 + (-x_c \sin \alpha + y_c \cos \alpha + \mu_c - \eta_p)^2]^{1/2}, \quad (2.21)$$

where  $x_c$  and  $y_c$  denote the displacement of carrier in  $x$  and  $y$  directions, while the  $\xi_p$  and  $\eta_p$  are the displacement of planet gear in  $\xi$  and  $\eta$  directions, and  $\alpha$  is the pressure angle of the planet gear. Then, the angle contact  $\mathcal{G}_{cp}$  [26] is followed

$$\mathcal{G}_{cp} = \tan^{-1} \left( \frac{-x_c \sin \alpha + y_c \cos \alpha + \mu_c - \eta_p}{x_c \cos \alpha + y_c \sin \alpha - \xi_p} \right), \quad (2.22)$$

The forces from the bearings in the research [26] are followed

$$f_{cp_x} = \mu_{cp} k_p (\delta_{cp} - \Delta_{cp}) \cos(\mathcal{G}_{cp} + \alpha), \quad (2.23)$$

$$f_{cp_y} = \mu_{cp} k_p (\delta_{cp} - \Delta_{cp}) \sin(\mathcal{G}_{cp} + \alpha), \quad (2.24)$$

$$f_{cp_\xi} = -\mu_{cp} k_p (\delta_{cp} - \Delta_{cp}) \cos \mathcal{G}_{cp}, \quad (2.25)$$

$$f_{cp_\eta} = -\mu_{cp} k_p (\delta_{cp} - \Delta_{cp}) \sin \mathcal{G}_{cp}, \quad (2.26)$$

where  $f_{cp_x}$  and  $f_{cp_y}$  are the bearing force based on the carrier in the  $x$  and  $y$  directions. The  $f_{cp_\xi}$  and  $f_{cp_\eta}$  denote the bearing force based on the planet gear in the  $\xi$  and  $\eta$  directions. The  $\mu_{cp}$  [26] is given below:

$$\mu_{cp} = \begin{cases} 1, & \text{if } \delta_{cp} > \Delta_{cp} \\ 0, & \text{if } \delta_{cp} < \Delta_{cp} \end{cases}, \quad (2.27)$$

Eq. (2.21) to (2.27) show that there is no force from bearing when the relative displacement is smaller than the bearing clearance value. Figure 2.8 shows the force of planet bearing changing with the value of the clearance. The equations for the carrier and the sun gear bearing with clearance are similar to these equations for planets. Except the carrier, sun and planet gear bearing, the bearing of carrier-ring in the dynamic model was also considered [26, 69]. However, there is no carrier-ring bearing in the planetary gearbox system to be focused on in this thesis because there is no bearing contacting carrier and ring gear. In this thesis, carrier, sun, ring, and planet gears use rotating coordinate system based on carrier. Therefore, the bearing clearance equations presented in Chapter 3 are different from Eqs. (2.21) to (2.26) given above.

In conclusion, bearing is an important structure in a planetary gearbox. This thesis considers a constant bearing clearance and details are discussed in Chapter 3. When a ring gear is fixed, there are carrier, sun-gear, and planet-gear bearings, while there is no carrier-ring bearing in our system.

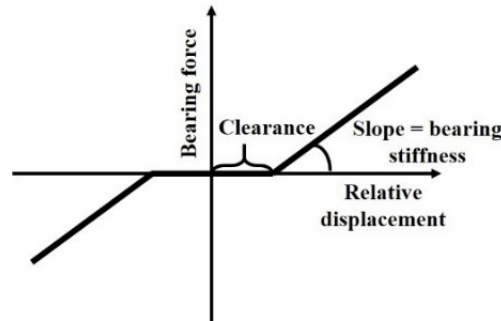


Figure 2.8 The relationship between bearing force and relative displacement.

### 2.3. Summary

As described above, the AM can save considerable time compared with the FEM, especially for the fault diagnosis which needs evaluating many crack levels. The potential energy method, one of the AM used in dynamic model, is used to simulate the external-external and external-internal gear mesh [34, 41]. Liang et al. [32] discussed the vibration signal of a planetary gearbox with different sun-gear tooth crack. However, the bearing clearance is ignored in this reference. In addition, the clearance is mostly discussed for a healthy planetary gear set [26]. In conclusion, this

thesis focuses on the effects of bearing clearance in the planetary gearbox with the sun-gear crack from 0% to 50%; it is summarized as follows:

- (1) Simulate the mesh stiffness of 0%, 0.05%, 0.1% ... 50% sun-gear crack for a planetary gearbox based on the references [34, 41].
- (2) In the dynamic model with fixed ring gear, there are three types of bearing in the planetary gear set. First is the sun gear bearing, the second is the planet bearings and the third is the bearing for the carrier. There is no ring gear bearing and carrier-ring bearing.
- (3) Consider the effects of carrier, sun-gear and planet-gear bearings in the dynamic response, respectively. Then, two of the three kinds bearing clearance are considered. Finally, all bearing clearance are considered in the dynamic modeling.

## **Chapter 3**

### **Structure of the Planetary Gearbox and its Dynamic Model Considering Sun**

#### **Gear Crack and Bearing Clearance**

As introduced in Chapter 2, the dynamic responses of the planetary gearbox with a tooth crack in sun gear could be obtained through simulating the corresponding mesh stiffness. Furthermore, Chapter 2 has described that the fixed and rotating coordinate systems are commonly employed in dynamic modelling. Specifically, this thesis uses the rotating coordinate system in carrier, sun, planet, and ring gears for dynamic model, and this coordinate system is based on the carrier. That means, if the carrier is as stationary, the other components including the sun, the planet, and the ring gears will have the relative motion with the carrier.

In this chapter, we will, first, introduce the experimental platform namely the planetary gearbox system that is to be simulated in this study. In addition, some assumptions on modeling of this planetary gearbox will be described. Modeling of the sun gear crack will also be introduced in Section 3.2. The models for bearing clearance will be introduced in Section 3.3. Finally, the details of the dynamic model and corresponding motion equations of the planetary gearbox system will be presented in Section 3.4.

#### **3.1. Introduction of the Planetary Gearbox System**

The planetary gearbox system in this thesis is the same as the system in [32, 35]. According to these researches, the Reliability Research Lab in the Department of Mechanical Engineering at University of Alberta, Edmonton, Canada has a planetary gearbox test rig as shown in Figure 3.1. This experimental platform includes one variable-frequency drive (VFD), one lubrication system, one drive motor, one bevel gearbox, two planetary gear sets, two speed-up gearboxes, and one load motor. It should be noted that the second stage of the planetary gearbox will be employed as research target in this work, as shown in Figure 3.1. The detailed parameters of the bevel and planetary gearboxes including number of teeth and their reduction ratios are shown in Table 3.1. There are three planet gears in the first stage planetary gear set, and the second stage focused on this thesis has four planet gears.

In the second stage planetary gearbox, the input gear is sun gear, while the carrier is output. In addition, the ring gear is fixed, the moveable parts are the carrier, the sun, and the planet gears. The frequency of driving motor is fixed at 1200 rpm. According to the values of gearboxes' parameters in Table 3.1, the frequency ( $f_s$ ) of the sun gear in the second stage planetary gearbox can be calculated through the following formulation

$$f_s = \frac{f_d}{i_b i_{stage1}}, \quad (3.1)$$

where  $f_d$  denotes the frequency of the driving motor,  $i_b$  and  $i_{stage1}$  are the reduction ratio of bevel gearbox and the reduction ratio of the first stage planetary gear set, respectively. Thus, the rotating frequency of the sun gear of the second stage planetary gearbox is 0.778 Hz based on Eq. (3.1). The mesh frequency  $f_m$  in stage two is 11.970 Hz which is calculated by

$$f_m = \frac{f_s}{\frac{1}{Z_s} - \frac{1}{Z_p}}, \quad (3.2)$$

where  $f_s$  is the sun gear rotating frequency and coefficients  $Z_s$  and  $Z_p$  denote the numbers of teeth of the sun gear and the planet gear, respectively.

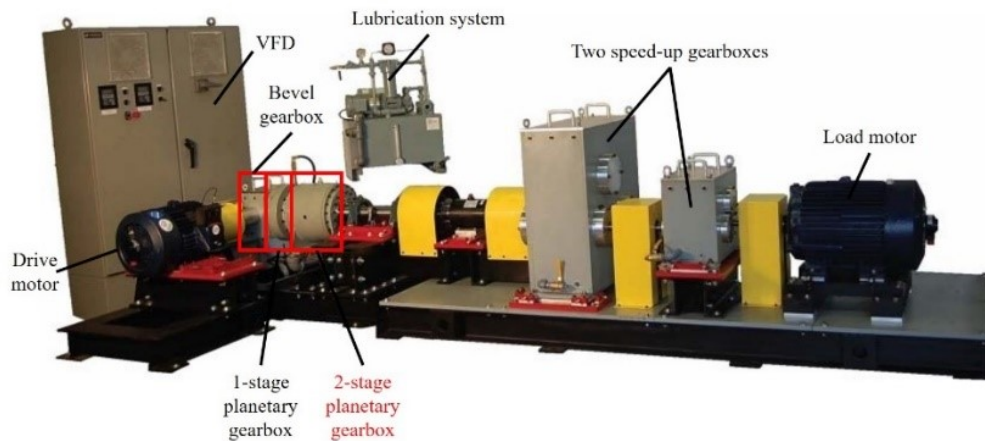


Figure 3.1 Planetary gearbox test rig in RRL, University of Alberta [35].

Table 3.1 Number of teeth and the reduction ratio of each gearbox in the test rig.

	Bevel gearbox		1 <sup>st</sup> stage planetary gearbox (three planet gears)			2 <sup>nd</sup> stage planetary gearbox (four planet gears)		
	Input gear	Output gear	Sun gear	Planet gear	Ring gear	Sun gear	Planet gear	Ring gear
<b>No. of teeth</b>	18	72	28	62	152	19	31	81
<b>Reduction ratio</b>	4.000		6.429			5.263		

Figure 3.2 shows the bevel gearbox and the structure of the two stages (e.g., stage one and stage two) of the planetary gearboxes. The bevel gearbox is connected to the first stage planetary gearbox, where the shaft of the sun gear is the output of the bevel gearbox, which is also taken to be the input for the first stage planetary gearbox. The carrier is the output of the first stage planetary gearbox which is connected to the sun gear of the second stage planetary gearbox.

Figure 3.3 illustrates the specific components of the planetary gearbox in stages one and two. In stage one, there are three identical planet gears and their corresponding bearings, one carrier and its corresponding bearing, and one ring gear without bearing. In stage two, there are four identical planet gears and their corresponding bearings, one carrier and its corresponding bearing, and one ring gear without bearing. There are two other supporting bearings for the carrier output shaft of the second stage planetary gearbox at the right side of stage two, as shown in Figures 3.2 and 3.3.

In stage two planetary gearboxes, there are three different bearing types including carrier bearing (stage one), carrier bearing (stage two), and four planet gear bearings. Figure 3.4 shows the location and the structures of these mentioned bearings for the second stage planetary gearbox. Table 3.2 lists the parameters of two carrier bearings and the planet gear bearing for the two-stage planetary gearboxes. The parameters ID and OD are the bearing inner and outer race diameters, respectively.

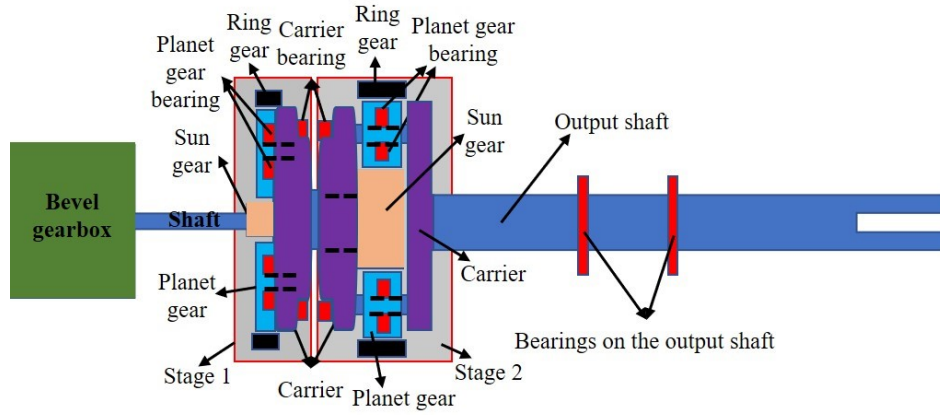


Figure 3.2 The structure of real planetary gearbox system.

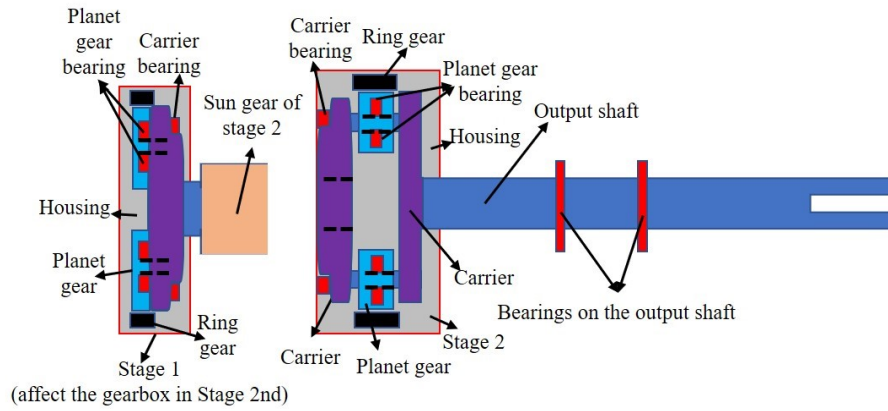


Figure 3.3 The installation diagram of the stages one and two planetary gearboxes.

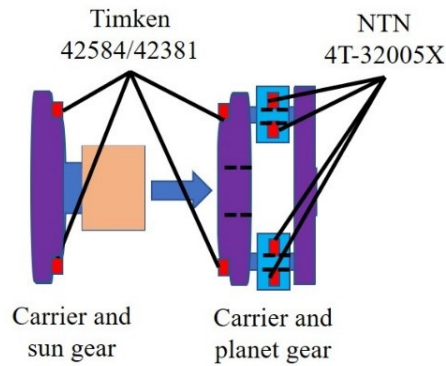


Figure 3.4 Location and structure of bearings.

Table 3.2 Parameters of two carrier bearings and planet gear bearings for the two-stage planetary gearboxes.

Location	Description	ID (mm)	OD (mm)	Width (mm)	No. of rollers
Carrier bearing (stage one)	Timken 42584/42381	96.838	148.4	28.58	26
Carrier bearing (stage two)	Timken 42584/42381	96.838	148.4	28.58	26
Planet gear bearing	NTN 4T-32005X	25	47	15	19

The Timken 42584/42381 and NTN 4T-32005X bearings shown in Table 3.2 and Figure 3.4 are both roller bearing with tapered bore, which means the tapered roller bearing is used for the carrier (stage one), the carrier (stage two), and the planet gears. Furthermore, Figure 3.5 shows the geometrical structure of the roller bearing with tapered bore. In Table 3.2, Timken 42584/42381 means the type series of cup is 42584 and the cone type series is 42584. These data are obtained from the online available documents of Timken and NTN companies [70, 71].

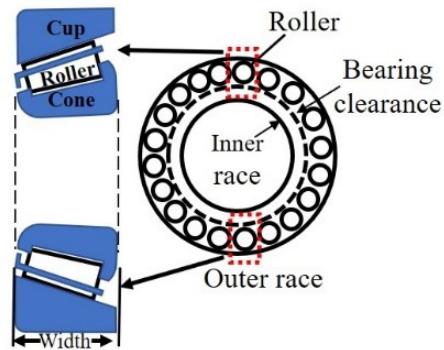


Figure 3.5 The structure of the roller bearing with the tapered bore.

As to the clearances of these bearings, these C codes including C1, C2, C0/CN, C3, C4, and C5 are used to describe the bearing clearance. This nomenclature is in accordance with the standard of ISO 5753: C1 is lower than C2, C2 is lower than C0/CN, C0/CN is the standard clearance for

applications under normal operating conditions, C3 is higher than C0/CN, C4 is higher than C3, and C5 is higher than C4. Although, there are 6 C-codes for bearing clearance, the bearings in this thesis only have 5 C-code without the C1, based on the documents of bearing companies [70, 71]. Furthermore, C0/CN (normal) and C3 are used in a variety of applications such as gearboxes [70]. Therefore, the bearing clearance under normal operating conditions (C0/CN) is considered in this thesis, and the minimum value of C0/CN is considered. If this extreme clearance affects the vibration signal with sun-gear tooth crack, other higher clearance will have the same influence in vibration response.

The carrier bearing in stage one is produced by Timken [70]. The minimum normal clearance of the carrier bearing in stage one is 0.080 mm, as shown in Table 3.3. The type of the carrier bearing in stage one is the same as the carrier bearing used in stage two. Hence, the minimum normal clearance of the carrier bearing in stage two is also 0.080 mm, as shown in Table 3.3.

The clearance of the planet bearing is shown in Table 3.4, which is different from the bearings of carrier. This bearing is produced by NTN and the minimum normal clearance is 0.035 mm [71].

As mentioned above, this thesis focuses only on the planetary gearbox in stage two. The nested structure of the two planetary gearboxes is complex, because the sun gear in stage two is naturally fixed with the carrier in stage one, and the vibration generated from the carrier in stage one can affect the gearbox in stage two during operations. Therefore, we assumed that the sun gear in stage two is rigidly connected to carrier in stage one. Then, this structure seems to be a single rigid body (SRB) and the carrier bearing in stage one is also the bearing that is used for supporting the sun gear of stage two. Furthermore, the single structure, including the carrier of stage one and sun gear shaft of stage two, is receiving free rotation input from stage one. We have ignored the vibration caused by gear meshing in stage one and its impact on our targeted stage two planetary gearbox.

We assumed that the bearing clearance is its corresponding minimum normal clearance (the minimum value in C0/CN), and this clearance is not changing during operation. According to Chapter 2, if the vibration of a gear is lower than its corresponding bearing clearance, forces from any direction will not be produced from the bearing. The limitation is because the real bearing clearance could be different from the minimum normal clearance, and usually it is difficult to be measured in the gearbox in practice.

Table 3.3 Clearance for carrier bearing based on Timken document [70].

Nominal bore diameter (mm)		C2		Normal (C0/CN)		C3		C4		C5	
Over (mm)	Incl. (mm)	Min. (mm)	Max. (mm)	Min. (mm)	Max. (mm)	Min. (mm)	Max. (mm)	Min. (mm)	Max. (mm)	Min. (mm)	Max. (mm)
80	100	0.055	0.080	0.080	0.110	0.110	0.140	0.140	0.180	0.180	0.230

Table 3.4 Clearance for planet gear bearing based on NTN document [71].

Nominal bore diameter (mm)		C2		Normal (C0/CN)		C3		C4		C5	
Over (mm)	Incl. (mm)	Min. (mm)	Max. (mm)	Min. (mm)	Max. (mm)	Min. (mm)	Max. (mm)	Min. (mm)	Max. (mm)	Min. (mm)	Max. (mm)
24	30	0.020	0.045	0.035	0.060	0.045	0.070	0.055	0.080	-	-

### 3.2. Gear Crack Modeling

Sun gear crack is a common tooth fault in the planetary gearbox described in Chapter 1, and this fault could make the gear set failures if no early detection is conducted. If a planetary gearbox is damaged by tooth crack, it causes economic loss or catastrophic accidents. Therefore, this thesis focuses on the sun-gear tooth crack, and the crack level is from 0% to 50% with an increment of 0.5%. The 0% level means there is no tooth crack, the 50% is the crack length with 3.90 mm, and the 0.5% is equal to 0.039 mm crack length. In other words, there are 101 cases in this thesis from 0% to 50% crack level.

In this thesis the root circle of sun gear is lower than its base circle, and thus the tooth crack modeling (Figure 3.6) is same as the model mentioned in Chapter 2 [41]. In this figure, the  $q_1$  is the crack length, and the crack initiation point is point  $N$  in the root circle. Then, the crack is modeled with a straight-line growth from the point  $N$  to the point  $A$  as shown in Figure 3.6. The

extreme crack length is that, the tooth crack propagates the growth line from initiation point  $N$  to the end point  $B$  which is 50% crack level. Furthermore, the line segment  $MN$  is interpreted as the initial notch which is not considered as crack length [41]. Figure 3.7 shows the length and width propagation [72]. In this figure,  $w$  denotes the width and  $q_l$  is the crack length; when the length  $q_l$  increases, the width  $w$  always remains the same length  $A-A$  during the growth of the crack level. In reality, whenever there is a crack, there is also a crack thickness value in addition to crack length and crack width as described above. Since this thesis focuses on dynamic simulation, we have assumed that the crack width is zero. This model is also used in another investigation [32].

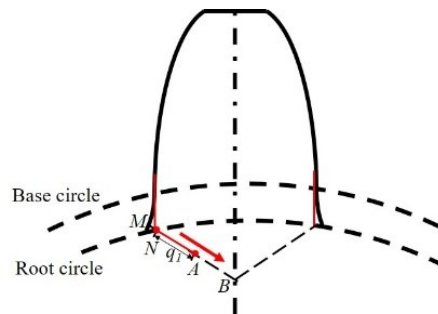


Figure 3.6 The sun-gear tooth crack modeling [41].

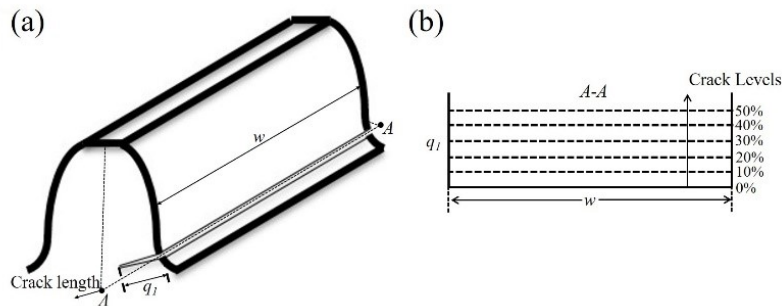


Figure 3.7 Length and width propagation (a) model, (b) the related scenario [72].

Wu et al. [62] researched the effect of tooth crack; it shows that the influence caused by the crack is observable, when the crack level grows. Then, Pandya and Parey [47] pointed the vibration level changes drastically for a advanced crack (more than 40%), and the accuracy of the mesh stiffness generated by potential energy model decreases through the crack level growth. Therefore, this thesis focuses on the effect of bearing clearance for a planetary gearbox, with low sun-gear tooth crack level from 0% to 50%. Furthermore, 6 different crack levels are used to analyse the effect of sun-gear tooth crack for a planetary gearbox, and these levels include healthy

level (0%), low-crack levels (10%, 20%, 30%, and 40%), and half-tooth level (50%), in Chapter 4. If the effect of the bearing clearance is found in low-crack level, the impulse caused by crack will be discovered in high-crack level. The correspondence between crack levels and length is shown in Table 3.5.

Table 3.5 Crack levels and length.

Crack Levels	0%	10%	20%	30%	40%	50%
Crack Length (mm)	0	0.78	1.56	2.34	3.12	3.90

Due to the comparison between finite element method (FEM) and analytical method (AM) in Chapter 2, the time-saving AM is used to model the sun-gear tooth crack in this thesis. Furthermore, the real planetary gearbox system and tooth crack model considered in this thesis are the same as the system in the investigation of Liang et al. [32], discussed in Chapter 2. According to the crack model with Eqs. (2.12) to (2.19), this thesis simulates the mesh stiffness for ring-planet and sun-planet gear pairs, the results are discussed in Chapter 4.

### 3.3. Bearing Clearance Modeling

The dynamic model based on the lab planetary gearbox considering clearances is shown in Figure 3.8. The carrier, ring, sun, and planet are denoted by subscripts  $c$ ,  $r$ ,  $s$ , and  $p$ , respectively. Each gear has two planes and one rotational degree of freedom, denoted by  $x$ ,  $y$ , and  $\theta$ , respectively, where  $x$  is the radial displacement,  $y$  is the tangential displacement, and  $\theta$  is the rotational displacement. A planetary gearbox has one carrier, one sun gear, one ring gear, and  $N$  planet gears. Thus, a single planetary gearbox has  $3(N+3)$  degrees of freedom, where  $N = 4$  is the number of planet gears for the second stage planetary gearbox focused in this thesis. Then, the coordinate systems for carrier, sun, planet, and ring gears are rotating coordinate system which is fixed on the carrier [32]. This means all the components in a planetary gearbox use the same coordinate system, and this system rotates with the carrier. In other words, if the carrier seems be stationary, there will be a relative motion between the carrier and other components (the sun, the planet, and the ring gears). Table 3.6 shows parameters of the modeled planetary gearbox that are used in this study.

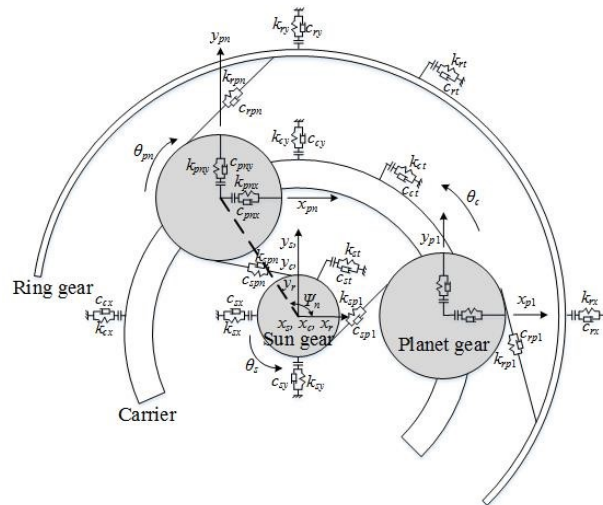


Figure 3.8 Lumped parameter model of the planetary gear set.

Table 3.6 Parameters setting of the modeled planetary gearbox.

Parameters	Sun gear	Planet gear	Ring gear
Number of teeth	19	31	81
Module (mm)	3.2	3.2	3.2
Pressure angle (°)	20	20	20
Mass (kg)	0.700	1.822	5.982
Face width (m)	0.0381	0.0381	0.0381
Young's modulus (Pa)	$2.068 \times 10^{11}$	$2.068 \times 10^{11}$	$2.068 \times 10^{11}$
Poisson's ratio	0.3	0.3	0.3
Base circle radius (mm)	28.3	46.2	120.8
Bearing stiffness (N·m)	$k_{sx}=k_{sy}=k_{rx}=k_{ry}=k_{cx}=k_{cy}=k_{pnx}=k_{pny}=1.0 \times 10^8$		
Bearing damping (Ns/m)	$c_{sx}=c_{sy}=c_{rx}=c_{ry}=c_{cx}=c_{cy}=c_{pnx}=c_{pny}=1.5 \times 10^3$		
Bearing clearance (mm)	$\Delta_c = \Delta_s = 0.080, \Delta_p = 0.035$		

The equations of bearing force ( $F_{cpnx}$  and  $F_{cpny}$ ) between the carrier and the  $n$ -th planet are different [32] due to the planet gear bearing clearance. These forces considering bearing clearance in this thesis are modified [26, 32]. The  $\mu$  and  $(\delta - \Delta)$  are used to calculate the effect of bearing clearance [26]. This thesis uses these variables ( $\mu$ ,  $\delta$ , and  $\Delta$ ) to improve the bearing force equations [32], then, the modified equations are shown as

$$F_{cpnx} = \mu_{cpn} k_{pnx} (\delta_{cpn} - \Delta_p) \cos(\mathcal{G}_{cpn}) + \mu_{cpn} c_{pnx} (\dot{x}_{pn} - \dot{x}_c), \quad (3.3)$$

$$F_{cpny} = \mu_{cpn} k_{pny} (\delta_{cpn} - \Delta_p) \sin(\mathcal{G}_{cpn}) + \mu_{cpn} c_{pny} (\dot{y}_{pn} - \dot{y}_c), \quad (3.4)$$

where  $k_{pnx}$  and  $k_{pny}$  denote the mesh stiffness of the planet gear bearing in directions  $x$  and  $y$ ,  $c_{pnx}$  and  $c_{pny}$  are the damping for the planet gear bearing in directions  $x$  and  $y$ ,  $\Delta_p$  is the clearance of planet bearing and  $\delta_{cpn}$  is the relative displacement between the planet and the carrier. Based on the same coordinate system used in carrier and planet gears, their displacement can be calculated directly in the same axis, such as  $x_{pn} - x_c$  in the  $x$ -direction which is different from Eq. (2.21) in Chapter 2. Therefore, the equation of relative displacement  $\delta_{cpn}$  is

$$\delta_{cpn} = \sqrt{(x_{pn} - x_c)^2 + (y_{pn} - y_c)^2}, \quad (3.5)$$

where  $\mathcal{G}_{cpn}$  is the contact angle between the  $n$ -th planet and the carrier, that is

$$\mathcal{G}_{cpn} = \begin{cases} \tan^{-1}\left(\frac{y_{pn} - y_c}{x_{pn} - x_c}\right) & \text{if } x_{pn} > x_c \\ \frac{\pi}{2} & \text{if } x_{pn} = x_c, y_{pn} > y_c \\ -\frac{\pi}{2} & \text{if } x_{pn} = x_c, y_{pn} < y_c \\ \pi + \tan^{-1}\left(\frac{y_{pn} - y_c}{x_{pn} - x_c}\right) & \text{if } x_{pn} < x_c \end{cases}, \quad (3.6)$$

where  $x_c$  and  $y_c$  denote the displacement of carrier in directions  $x$  and  $y$ , respectively.  $x_{pn}$  and  $y_{pn}$  are the displacement for the  $n$ -th planet gear in directions  $x$  and  $y$ , respectively. The value of  $\mu_{cpn}$  is determined by the coefficient  $\mathcal{G}_{cpn}$  [26],

$$\mu_{cpn} = \begin{cases} 1, & \text{if } \delta_{cpn} > \Delta_p \\ 0, & \text{if } \delta_{cpn} < \Delta_p \end{cases}, \quad (3.7)$$

From Eq. (3.7), it is noted that no force is produced from the planet bearing when the relative displacement  $\delta_{cpn}$  is lower than the clearance  $\Delta_p$ . Similar to the modified between Eqs. (3.3) and (3.7), the motion equations of dynamic modeling are modified equations from the investigation of Liang et al. [32].

### 3.4. Motion Equations in Dynamic Model

For the sun gear, the corresponding motion equations are modified [26, 32], similar to the Eqs. (3.3) and (3.4), and the improved motion equations are

$$\begin{aligned} m_s \ddot{x}_s + \mu_s c_{sx} \dot{x}_s + \mu_s k_{sx} (\delta_s - \Delta_s) \cos(\vartheta_s) + \sum_n F_{spn} \cos \Psi_{sn} = \\ m_s x_s \Omega^2 + 2m_s \dot{y}_s \Omega + m_s y_s \dot{\Omega} \end{aligned}, \quad (3.8)$$

$$\begin{aligned} m_s \ddot{y}_s + \mu_s c_{sy} \dot{y}_s + \mu_s k_{sy} (\delta_s - \Delta_s) \sin(\vartheta_s) + \sum_n F_{spn} \sin \Psi_{sn} = \\ m_s y_s \Omega^2 - 2m_s \dot{x}_s \Omega - m_s x_s \dot{\Omega} \end{aligned}, \quad (3.9)$$

$$(J_s / r_s) \ddot{\theta}_s + \sum_n F_{spn} = T_i / r_s, \quad (3.10)$$

where  $J$  is the mass moment of inertia,  $T_i$  is the input torque of the sun gear,  $r_s$  is the radius of the sun gear,  $\Delta_s$  is the clearance for the sun gear bearing,  $\theta_s$  is the rotational displacement for sun gear,  $x_s$  and  $y_s$  are the displacement for the sun gear in directions  $x$  and  $y$ , respectively. The coefficients  $\delta_s$ ,  $\vartheta_s$  and  $\mu_s$  are given as

$$\delta_s = \sqrt{x_s^2 + y_s^2}, \quad (3.11)$$

$$\vartheta_s = \begin{cases} \tan^{-1}\left(\frac{y_s}{x_s}\right) & \text{if } x_s > 0 \\ \frac{\pi}{2} & \text{if } x_s = 0, y_s > 0 \\ -\frac{\pi}{2} & \text{if } x_s = 0, y_s < 0 \\ \pi + \tan^{-1}\left(\frac{y_s}{x_s}\right) & \text{if } x_s < 0 \end{cases}, \quad (3.12)$$

$$\mu_s = \begin{cases} 1, & \text{if } \delta_s > \Delta_s \\ 0, & \text{if } \delta_s < \Delta_s \end{cases}, \quad (3.13)$$

The dynamic force generated from the sun-planet gear mesh  $F_{spn}$  (the subscript  $spn$  denotes the sun-planet gear interaction) is [32]

$$F_{spn} = k_{spn} \delta_{spn} + c_{spn} \dot{\delta}_{spn}, \quad (3.14)$$

$$\delta_{spn} = (x_s - x_{pn}) \cos \Psi_{sn} + (y_s - y_{pn}) \sin \Psi_{sn} + r_s \theta_s + r_{pn} \theta_{pn} - r_c \theta_c \cos \alpha, \quad (3.15)$$

$$\Psi_{sn} = \frac{\pi}{2} - \alpha + \Psi_n, \quad (3.16)$$

$$\Psi_n = \frac{2(n-1)\pi}{N}, \quad (3.17)$$

where  $m$  is the mass of a gear,  $\Psi_n$  is the circumferential angle of the  $n$ -th planet,  $k$  is the stiffness coefficient,  $c$  is the damping coefficient,  $\delta_{spn}$  is the relative displacement between the sun gear and  $n$ -th planet gear,  $x$  and  $y$  are the displacement in directions  $x$  and  $y$ ,  $\alpha$  is the pressure angle of a gear pair,  $r_s$  is the radius of sun gear and  $\theta$  is the angle of rotation.

For the ring gear, the corresponding motion equations are modified based on [26, 32], similar to the sun gear, the motion equations of ring gear are

$$\begin{aligned}
m_r \ddot{x}_r + c_{rx} \dot{x}_r + k_{rx} x_r + \sum_n F_{rpn} \cos \Psi_m = \\
m_r x_r \Omega^2 + 2m_r \dot{y}_r \Omega + m_r y_r \dot{\Omega}
\end{aligned} \tag{3.18}$$

$$\begin{aligned}
m_r \ddot{y}_r + c_{ry} \dot{y}_r + k_{ry} y_r + \sum_n F_{rpn} \sin \Psi_m = \\
m_r y_r \Omega^2 + 2m_r \dot{x}_r \Omega + m_r x_r \dot{\Omega}
\end{aligned} \tag{3.19}$$

$$(J_r / r_r) \ddot{\theta}_r + (c_{rt} / r_r) \dot{\theta}_r + (k_{rt} / r_r) \theta_r + \sum_n F_{rpn} = 0, \tag{3.20}$$

where  $r_r$  is the radius of the ring gear,  $\theta_r$  is the rotational displacement for the ring gear,  $x_r$  and  $y_r$  are the displacement for the ring gear in directions  $x$  and  $y$ , respectively.

The dynamic force generated from the ring-planet gear mesh  $F_{rpn}$  (the subscript  $rpn$  denotes the ring-planet gear interaction) is [32]

$$F_{rpn} = k_{rpn} \delta_{rpn} + c_{rpn} \dot{\delta}_{rpn}, \tag{3.21}$$

$$\begin{aligned}
\delta_{rpn} = (x_r - x_{pn}) \cos \Psi_m + (y_r - y_{pn}) \sin \Psi_m \\
+ r_r \theta_r - r_{pn} \theta_{pn} - r_c \theta_c \cos \alpha
\end{aligned} \tag{3.22}$$

$$\Psi_m = \frac{\pi}{2} + \alpha + \Psi_n \tag{3.23}$$

For the carrier, the motion equations are similar to Eqs. (3.8), (3.9), and (3.10), which have improved the corresponding equations in [26, 32].

$$\begin{aligned}
m_c \ddot{x}_c + \mu_s c_{cx} \dot{x}_c + \mu_s k_{cx} (\delta_c - \Delta_c) \cos(\vartheta_c) - \sum_n F_{cpnx} = \\
m_c x_c \Omega^2 + 2m_c \dot{y}_c \Omega + m_c y_c \dot{\Omega}
\end{aligned} \tag{3.24}$$

$$\begin{aligned}
m_c \ddot{y}_c + \mu_s c_{cy} \dot{y}_c + \mu_s k_{cy} (\delta_c - \Delta_c) \sin(\vartheta_c) - \sum_n F_{cpny} = \\
m_c y_c \Omega^2 - 2m_c \dot{x}_c \Omega - m_c x_c \dot{\Omega}
\end{aligned} \tag{3.25}$$

$$\begin{aligned} (J_c / r_c) \ddot{\theta}_c + \sum_n F_{cpnx} \sin \Psi_n - \\ \sum_n F_{cpny} \cos \Psi_n = T_o / r_c \end{aligned} \quad (3.26)$$

where  $r_c$  is the radius of the carrier,  $\Delta_c$  is the clearance for carrier bearing,  $T_o$  is the output torque of the carrier,  $\theta_c$  is the rotational displacement for the carrier,  $x_c$  and  $y_c$  are the displacement for the carrier in directions  $x$  and  $y$ , respectively. The coefficients  $\delta_c$ ,  $\mathcal{G}_c$  and  $\mu_c$  are given as

$$\delta_c = \sqrt{x_c^2 + y_c^2}, \quad (3.27)$$

$$\mathcal{G}_c = \begin{cases} \tan^{-1}\left(\frac{y_c}{x_c}\right) & \text{if } x_c > 0 \\ \frac{\pi}{2} & \text{if } x_c = 0, y_c > 0 \\ -\frac{\pi}{2} & \text{if } x_c = 0, y_c < 0 \\ \pi + \tan^{-1}\left(\frac{y_c}{x_c}\right) & \text{if } x_c < 0 \end{cases}, \quad (3.28)$$

$$\mu_c = \begin{cases} 1, & \text{if } \delta_c > \Delta_c \\ 0, & \text{if } \delta_c < \Delta_c \end{cases}, \quad (3.29)$$

For the planet gear, similar to the sun gear, the modified motion equations are based on [26, 32]

$$\begin{aligned} m_{pn} \ddot{x}_{pn} + F_{cpnx} - F_{spn} \cos \Psi_{sn} - F_{rpn} \cos \Psi_{rn} = \\ m_{pn} x_{pn} \Omega^2 + 2m_{pn} \dot{y}_{pn} \Omega + m_{pn} y_{pn} \dot{\Omega} \\ + m_{pn} r_c \Omega^2 \cos \Psi_n \end{aligned} \quad (3.30)$$

$$\begin{aligned} m_{pn} \ddot{y}_{pn} + F_{cpny} - F_{spn} \sin \Psi_{sn} - F_{rpn} \sin \Psi_{rn} = \\ m_{pn} y_{pn} \Omega^2 - 2m_{pn} \dot{x}_{pn} \Omega - m_{pn} x_{pn} \dot{\Omega} \\ + m_{pn} r_c \Omega^2 \sin \Psi_n \end{aligned} \quad (3.31)$$

$$(J_{pn} / r_{pn}) \ddot{\theta}_{pn} + F_{spn} - F_{rpn} = 0, \quad (3.32)$$

where  $\theta_{pn}$  is the rotational displacement for  $n$ th planet gear,  $x_{pn}$  and  $y_{pn}$  are the displacement for the  $n$ -th planet gear in directions  $x$  and  $y$ , respectively.

In these equations-of-motion, the subscripts  $c$ ,  $r$ ,  $s$ , and  $pn$  are denoted for the carrier, ring, sun, and  $n$ -th planet gears, respectively. Furthermore, the rotational speed is a constant and ring gear is fixed. Thus, the angular acceleration of the carrier, planet, sun, and ring is 0.

We can obtain the vibration response of the carrier, sun, planet, and ring gear in the rotating coordinate system through the Eqs. (3.8) to (3.32). The coordinate transformed equation [73] is

$$\begin{bmatrix} x_g \\ y_g \end{bmatrix} = \begin{bmatrix} \cos(t\Omega_c) & -\sin(t\Omega_c) \\ \sin(t\Omega_c) & \cos(t\Omega_c) \end{bmatrix} \begin{bmatrix} x \\ y \end{bmatrix}, \quad (3.33)$$

where  $\Omega_c$  is the rotating speed of the carrier,  $t$  is the time,  $x$  and  $y$  denote the rotating coordinate system,  $x_g$  and  $y_g$  denote the fixed rotating coordinate system. The transmission path is not considered in this thesis. Thus, we have assumed that there is no attenuation for vibration signal in the planetary gearbox. Through the following equations, the vibration signal of planetary gearbox in terms of both directions are as follows:

$$x_{signal} = x_{sg} + \sum_{n=1}^4 x_{png} + x_{cg} + x_{rg}, \quad (3.34)$$

$$y_{signal} = y_{sg} + \sum_{n=1}^4 y_{png} + y_{cg} + y_{rg}, \quad (3.35)$$

where  $x_{signal}$  and  $y_{signal}$  denote the vibration signal for a whole planetary gearbox in  $x_g$  and  $y_g$  direction, the subscript  $pn$  denotes the  $n$ th planet, respectively.

### 3.5. Summary

This chapter has discussed the structure of the planetary gearbox to be modeled, the dynamic forces generated by the sun-planet gear meshes and by the ring-planet gear meshes, and the motion equations of the sun gear, the ring gear, the carrier, and all planet gears. Three types of bearings including carrier bearing, sun-gear bearing, and planet-gear bearing are considered. We will describe the dynamic effect of bearing clearance through different combinations in the next chapter. These combinations are clearances of the sun-gear, planet-gear, or carrier bearings,

bearing clearance of the sun gear and planet gear, bearing clearance of the sun gear and carrier, bearing clearance of the planet gear and carrier, and bearing clearance of the carrier, sun gear, and planet gear. With these models introduced in this chapter, the effects of bearing clearances on the vibration responses will be covered in Chapter 4.

## Chapter 4

### Effect of the Bearing Clearance for the Dynamic Response

In Chapter 3, we have discussed the structure of the planetary gearbox, including stage one and stage two, which is physically located in the Reliability Research Lab at the University of Alberta. Focusing on stage two only of this physical planetary gearbox, we have also described in Chapter 3 its dynamic model that considers the sun gear crack and the bearing clearance effects. In this chapter, our main objective is to run the models reported in Chapter 3 and investigate the dynamic responses of the stage two planetary gear set using Matlab codes considering various scenarios of bearing clearances. The organization of this chapter is as follows:

In Section 4.1, we will run the Matlab code provided by Dr. Xihui Liang (see Preface) to generate the meshing stiffness profile for each pair of meshing gears under various length values of a single crack on the sun gear. These meshing profiles will be used in later sections of this chapter.

In Section 4.2, we will run the Matlab code provided by Dr. Xihui Liang (see Preface) to generate the dynamic responses of the stage two planetary gear set when all bearing clearances are assumed to be zero. These responses are generated under various length values of the sun gear crack. These responses will be the baseline for demonstration of the effects of bearing clearances in later sections wherein some or all of the bearing clearances are considered to be non-zero. This case is referred to as Case 1.

In Section 4.3, we will consider the scenario when only one type of bearings has non-zero clearance values. There are three types of bearings in the modeled stage two planetary gear set, namely the planet gear bearings (there are four of these as there are four units of the planet gears in the modeled gear set), the sun gear bearing, and the carrier bearing. The effects of clearances of each of these three types of bearings will be studied one by one in a subsection of this Section 4.3 and these three cases are referred to as Case 2, Case 3, and Case 4, respectively. These effects will be demonstrated for various length values of the sun gear crack. In this section, we use the improved differential equations presented in Chapter 3 as the effects of bearing clearances are

considered in these equations. Matlab code improved by me incorporating clearance effects is run to generate the dynamic responses under each of these cases.

In Section 4.4, we consider the scenarios wherein two of the three types of bearings have non-zero clearance values. Case 5 represents the scenario wherein only the sun gear bearing and all four planet gear bearings have non-zero clearance values. Case 6 is when only all planet gear bearings and the carrier bearing have non-zero clearance values. Case 7 is when only the sun gear bearing and the carrier bearing have non-zero clearance values. Under each of the three cases, the dynamic responses of the stage two planetary gear set are generated for various sun gear crack length values through the improved differential equations presented in Chapter 3.

In Section 4.5, we consider the scenario when all three types of bearings, namely the sun gear bearing, the four planet bearings, and the carrier bearing, have non-zero clearance values. Again, various length values of the sun gear crack are considered. Through the improved motion equations presented in Chapter 3, the dynamic responses generated in this section (Case 8) are compared with the baseline responses generated when no clearances are considered at all (Case 1).

The final summary and conclusion for this whole chapter is provided in Section 4.6.

#### **4.1. Mesh Stiffness with Sun Gear Tooth Crack**

As mentioned before, in this thesis, we model only the second stage of the planetary gearbox that is physically located in the Reliability Research Lab at the University of Alberta and is described in Chapter 3 of this thesis. This second stage planetary gear set has four planet gears, including planet gears 1, 2, 3, and 4, as illustrated in Figure 4.1. The sun gear is the input, while the carrier is the output. Then, the rotational direction of the ring gear, the sun gear, and the carrier are counterclockwise, while the planet gears use a clockwise rotation. According to the descriptions in Chapter 3, the running speed of the motor was fixed with 1200 rpm (i.e., 20 Hz), the input rotating speed of the sun gear in Stage 2 is 0.778 Hz, the duration of the sun wheel with one cycle is 1.286 s, and the meshing frequency  $f_m$  of the sun-planet gear is 11.970 Hz based on Eq. (3.2) in Chapter 3. Using the Matlab code provided by Dr. Xihui Liang (see Preface), in this section, we will run the code and generate the meshing stiffness profile for each pair of meshing gears under various values of the sun gear crack length.

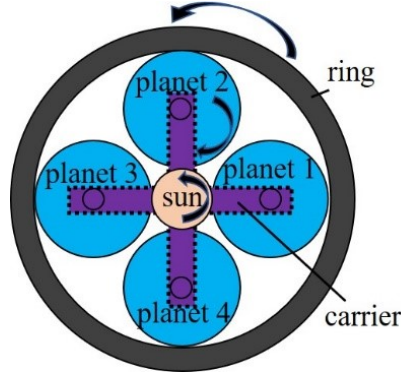


Figure 4.1 Planetary gearbox with four planet gears.

First, we calculate the meshing stiffness of the ring-planet gear pair based only upon the parameters setting [34]. In this case, the crack length values of the sun gear do not affect the ring-planet meshing stiffness profile, as the sun gear is not involved in this pair of meshing gears. Figure 4.2 shows the ring-planet meshing stiffness of the planet gear within two running cycles, it can be seen that the running time-interval of the ring-planet mesh stiffness is 3.174 s, which is 2.5 times that of the rotation cycle of the sun gear. The statuses of the planet gear and the ring gear are healthy without any tooth faults. Figure 4.2(a) is the mesh stiffness of ring-planet 1, Figure 4.2(b) is the mesh stiffness of ring-planet 2, Figure 4.2(c) is the mesh stiffness of ring-planet 3, and Figure 4.2(d) is the mesh stiffness of ring-planet 4. The  $k_{rpn}$  in the  $y$  axis denotes the  $n$ th ring-planet gear mesh stiffness, and  $n$  is a number from 1 to 4. These mesh stiffness plots are generated with the equations in the literature of Liang et al. [34], which are similar to Eqs. (2.12–2.19) in Chapter 2.

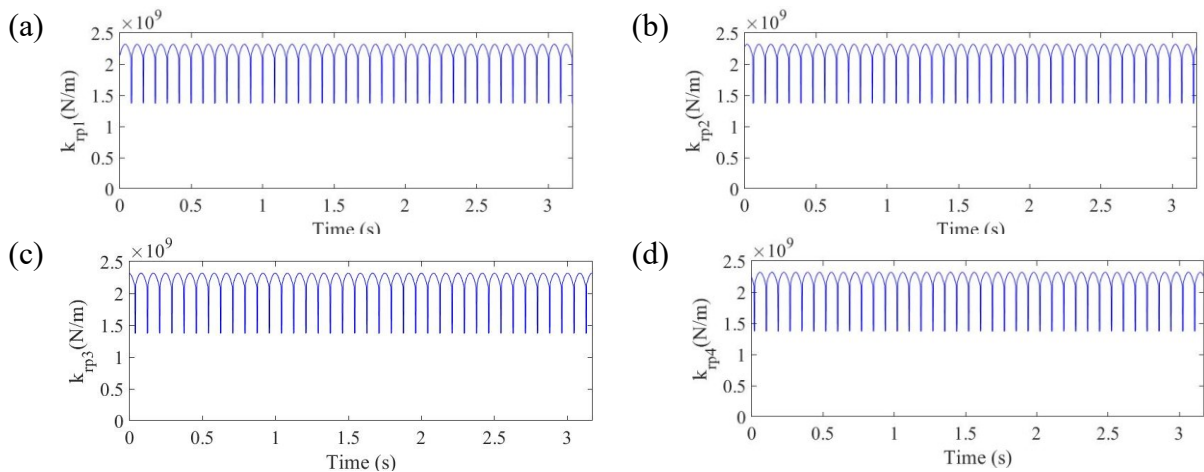


Figure 4.2 Meshing stiffness of (a) ring-planet 1, (b) ring-planet 2, (c) ring-planet 3, and (d) ring-planet 4 [34].

We next consider the meshing between the sun gear and the planet gears when the sun gear has a crack with various possible length values. Generally, the meshing stiffness of a pair of gears will be reduced if a gear fault, such as crack or weakness, exists in the gear-pair, and the durability of the planetary gearbox will also be reduced accordingly [31]. In the following, we present a few figures which demonstrate the reduction in meshing stiffness when a cracked tooth is involved in meshing. Figures 4.3, 4.4, 4.5, and 4.6 illustrate the meshing stiffness of the sun-planet pair with different levels (e.g., 0%, 10%, 20%, 30%, 40%, and 50%) of the tooth crack located in the sun-gear. These meshing stiffness plots with the sun-gear crack are generated with Eqs. (2.12–2.19), which are given in Chapter 2. We can observe the effect of a tooth crack encountered in a sun gear. From the resulting 50% meshing stiffness shown in Figure 4.3, it can be observed that the meshing stiffness produced by the gear crack is sharply reduced compared to the meshing stiffness of a healthy gear. Specifically, the minimum value of the meshing stiffness in a 0% crack level is  $1.1 \times 10^9$ , shown in Figure 4.3(a); the minimum value of the meshing stiffness in a 10% crack level is  $9.5 \times 10^8$ , shown in Figure 4.3(b); the minimum value of the meshing stiffness in a 20% crack level is  $8 \times 10^8$ , shown in Figure 4.3(c); the minimum value of the meshing stiffness in a 30% crack level is  $6.6 \times 10^8$ , shown in Figure 4.3(d); the minimum value of the meshing stiffness in a 40% crack level is  $5.1 \times 10^8$ , shown in Figure 4.3(e); and the minimum value of the meshing stiffness in a 50% crack level is  $3.7 \times 10^8$ , shown in Figure 4.3(f). The crack level represents the tooth fault degree in the sun gear of the planetary gearbox. As shown in Figure 4.3(f), the sudden drops of meshing stiffness in sun-planet 1 are detected when the operating time is from 0 s to 0.13 s and 1.59 s to 1.72 s. As shown in Figure 4.4(f), the sudden drops of meshing stiffness in sun-planet 2 are visible when the operating time is from 0.41 s to 0.54 s and 1.99 s to 2.12 s. Similarly, the sudden drops of meshing stiffness in sun-planet 3 in Figure 4.5(f) and sun-planet 4 in Figure 4.6(f) are visible when the operating time is from 0.8 s to 0.93 s and 2.39 s to 2.52 s, and 1.20 s to 1.33 s and 2.79 s to 2.92 s, respectively.

Furthermore, according to the mesh stiffness accompanied by the tooth crack in the sun-gear, the dynamic response can be calculated through the motion equations of the planetary gearbox, as discussed in Chapter 3. Consequently, the dynamic response effect that is generated by the main components of the planetary gearbox will be discussed in the next section.

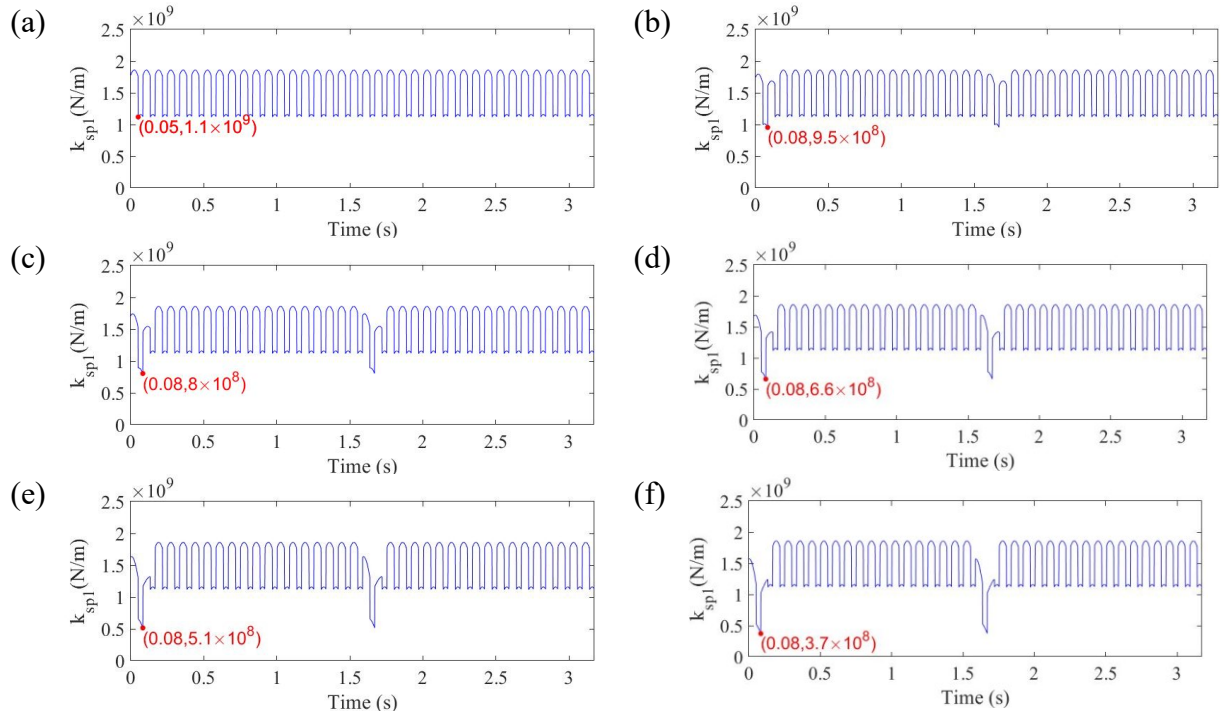


Figure 4.3 Meshing stiffness of sun-planet 1 with (a) 0%, (b) 10%, (c) 20%, (d) 30%, (e) 40%, and (f) 50% sun-gear tooth crack.

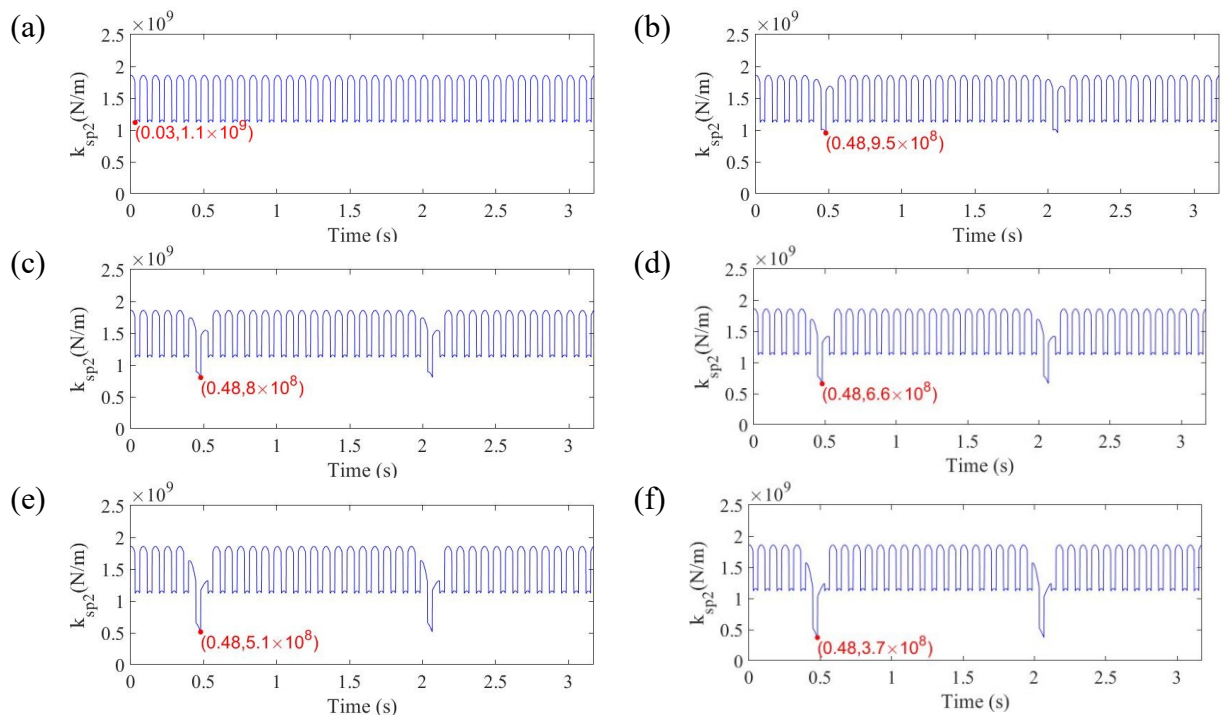


Figure 4.4 Meshing stiffness of sun-planet 2 with (a) 0%, (b) 10%, (c) 20%, (d) 30%, (e) 40%, and (f) 50% sun-gear tooth crack.

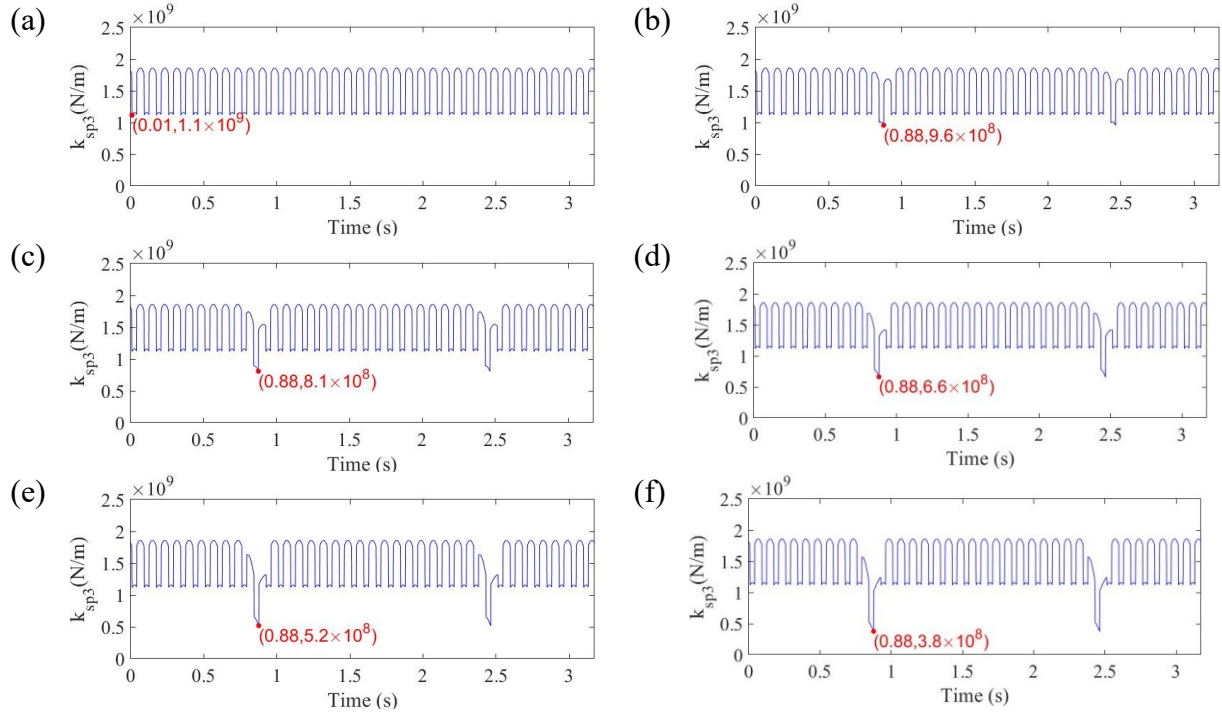


Figure 4.5 Meshing stiffness of sun-planet 3 with (a) 0%, (b) 10%, (c) 20%, (d) 30%, (e) 40%, and (f) 50% sun-gear tooth crack.

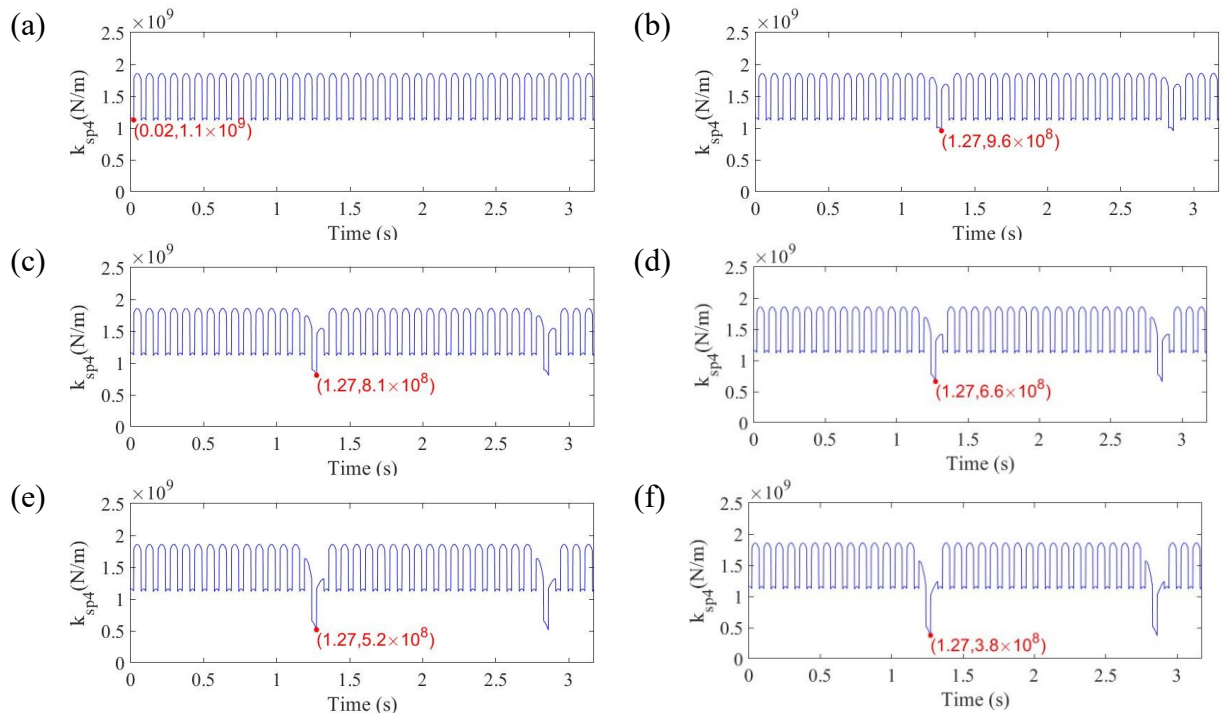


Figure 4.6 Meshing stiffness of sun-planet 4 with (a) 0%, (b) 10%, (c) 20%, (d) 30%, (e) 40%, and (f) 50% sun-gear tooth crack.

## 4.2. Case 1: Dynamic Modeling without Bearing Clearance

In this subsection, we assume that all bearings have zero clearance values. This means that the dynamic response effect without bearing clearance (e.g., carrier bearing clearance, sun-gear bearing clearance, and planet-gear bearing clearance are all assumed to be 0) will be discussed in detail. The Matlab code provided by Dr. Xihui Liang is run to generate the dynamic responses in this section.

The vibration signal of the planetary gearbox can be calculated through Eqs. (3.3–3.32) in Chapter 3. Then, the ODE15S function in MATLAB is used to solve the differential equations for the sun gear from Eqs. (3.8–3.10), for the ring gear from Eqs. (3.18–3.20), for the carrier from Eqs. (3.24–3.26), and for the planet gears from Eqs. (3.30–3.32). According to the coordinating motion equations, Figure 4.7 illustrates the displacement of the sun gear (a, b), the ring gear (c, d), the carrier (e, f), and the total planet gear (g, h) when the tooth crack level is 50%, and in which the  $x_{sg}$ ,  $x_{rg}$ ,  $x_{cg}$ ,  $x_{pg}$ ,  $y_{sg}$ ,  $y_{rg}$ ,  $y_{cg}$ , and  $y_{pg}$  are the displacements of the carrier, the sun-gear, the ring, and the planet-gear in the  $x_g$  and  $y_g$  directions, respectively. Then, the red dashed line shows the highest displacement value in the  $x_g$  direction, which is similar to the value in the  $y_g$  direction. Furthermore, the displacements  $x_{pg}$  and  $y_{pg}$  are calculated by

$$\begin{cases} x_{pg} = \sum_{n=1}^4 x_{png} \\ y_{pg} = \sum_{n=1}^4 y_{png} \end{cases}, \quad (4.1)$$

where  $x_{pg}$  and  $y_{pg}$  denote the displacement of the total planet gear in the  $x_g$  and  $y_g$  directions based on the fixed coordinate system discussed in Chapter 3, and  $x_{png}$  and  $y_{png}$  denote the displacement of the  $n$ th planet gear in the  $x_g$  and  $y_g$  directions based on the fixed coordinate system shown in Figure 4.8, which can be calculated through the coordinate transform equation, (Eq. 3.33).

Compared with Figure 4.7 (g, h) and the other figures (a, b, c, d, e, f), we observe the vibration displacement in the planet gear is much higher than that produced via other components without any bearing clearance. Then, Figure 4.8 illustrates the vibration displacement of each planet gear. From this figure, several interesting phenomena are found: (1) the displacement of planet gear 1 and 3 are opposite because the difference angle between planet gear 1 and 3 is  $180^\circ$ ; (2) similar to

planet gear 1 and 3, the displacements of planet gear 2 and 4 are also opposite, with a difference angle of  $180^\circ$ .

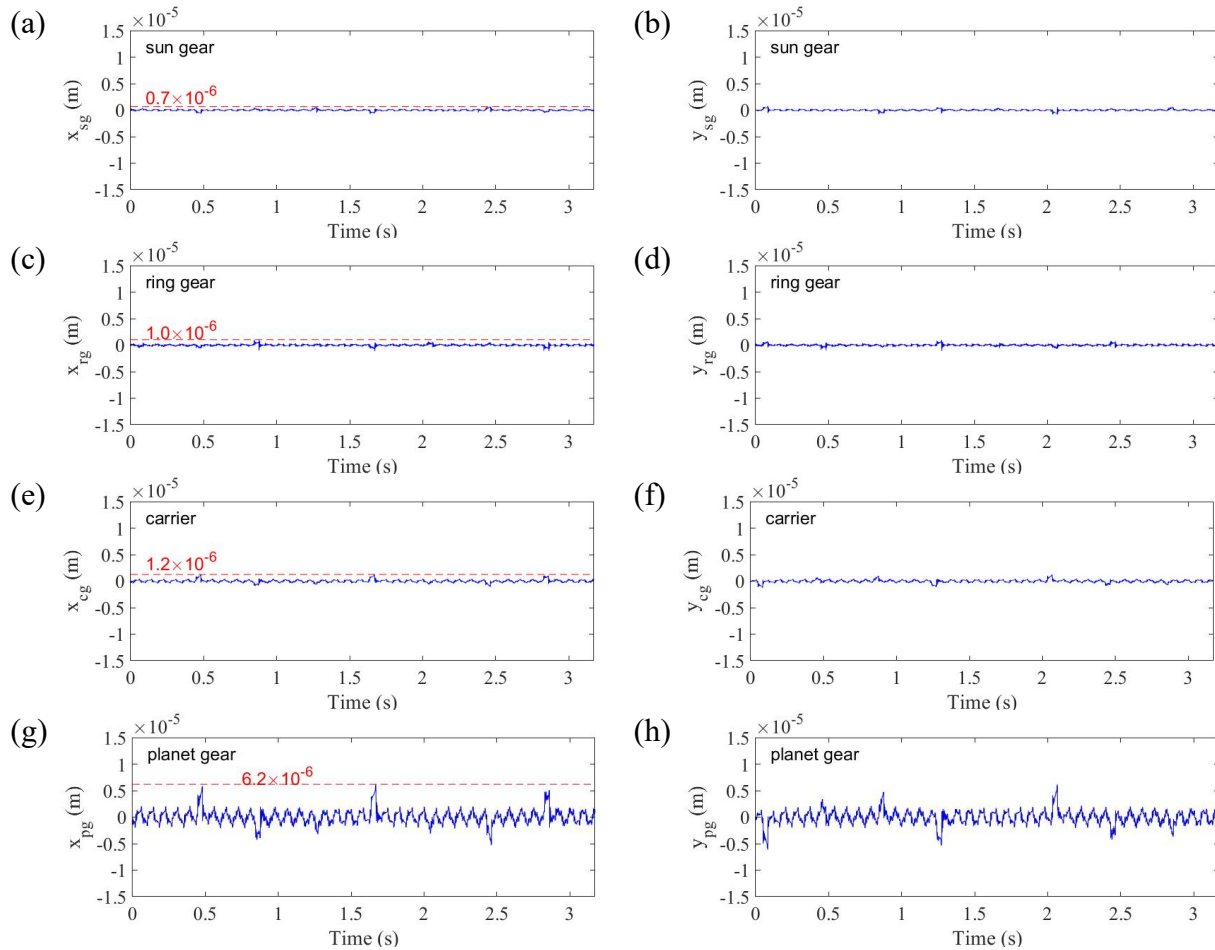


Figure 4.7 Vibration displacement signal of each component with a 50% sun-gear crack without clearance.

Finally, according to Eqs. (3.34) and (3.35), the vibration response of the planetary gear set is simulated and shown in Figure 4.9, which means adding the vibration displacement of each component shown in Figures 4.7(a, c, e, and g) to get Figure 4.9(k), and adding the vibration displacement of each component shown in Figures 4.7(b, d, f, and h) to get Figure 4.9(l). Then, the red dashed line in Figure 4.9(k) shows the highest displacement value of  $x_{signal}$  with a 50% crack level. From Figure 4.9, several interesting phenomena are found: (1) the impulse fault signals caused by a tooth crack are easily identified with the increase of a fault crack; (2) the fault impulse intervals are obvious in  $x_{signal}$ , while the impulses between 1.5 s and 2 s in  $y_{signal}$  are not detected, shown in Figure 4.9(l).

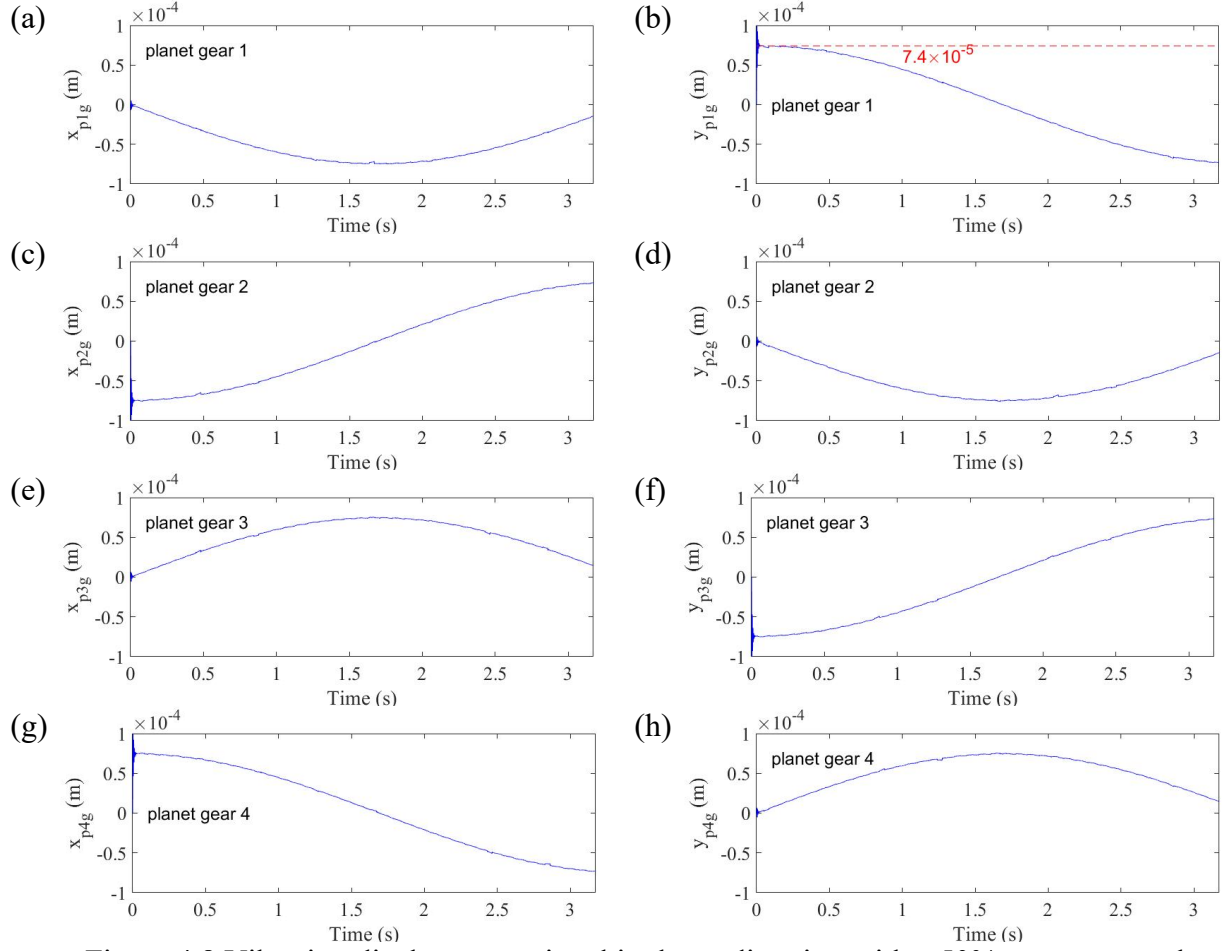


Figure 4.8 Vibration displacement signal in the  $x_g$  direction with a 50% sun-gear crack without clearance.

From 0 s to 3 s in Figure 4.9(k) and (l), eight time points are identified by a sun-gear crack: 0.07 s, 0.47 s, 0.84 s, 1.24 s, 1.64 s, 2.04 s, 2.44 s, and 2.84 s. Figure 4.10 shows the location of a tooth crack at eight different time points, wherein subfigure (a) shows when the tooth crack contacts with planet 1, subfigure (b) with planet 2, subfigure (c) with planet 3, subfigure (d) with planet 4, and subfigures (e)-(h) show when the tooth crack contacts with planets 1-4 again, respectively. Furthermore,  $\alpha$  is the rotation angle of the carrier, which is the angle between the  $x_g$  axis and the planet 1 gear shown in Figure 4.10(c), can be calculated by

$$\alpha = 180v_c t / \pi, \quad (4.2)$$

where  $v_c$  is the rotation speed of the carrier (rad/s), and  $t$  is the rotational time with unit s.

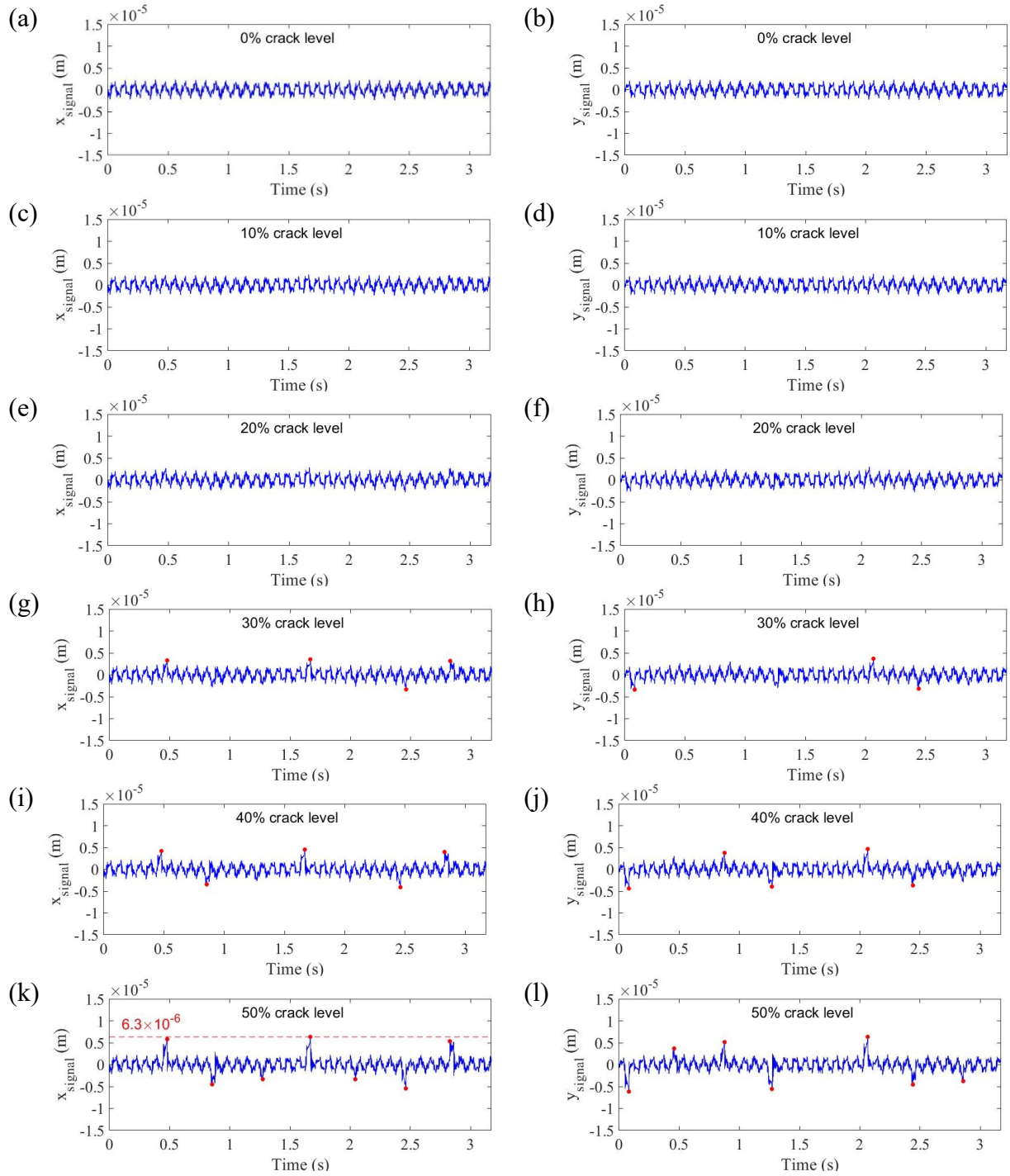


Figure 4.9 Vibration signal of the planetary gearbox in the  $x_g$  direction with (a) 0%, (c) 10%, (e) 20%, (g) 30%, (i) 40%, and (k) 50% sun-gear tooth cracks; in the  $y_g$  direction with (b) 0%, (d) 10%, (f) 20%, (h) 30%, (j) 40%, and (l) 50% sun-gear tooth cracks.

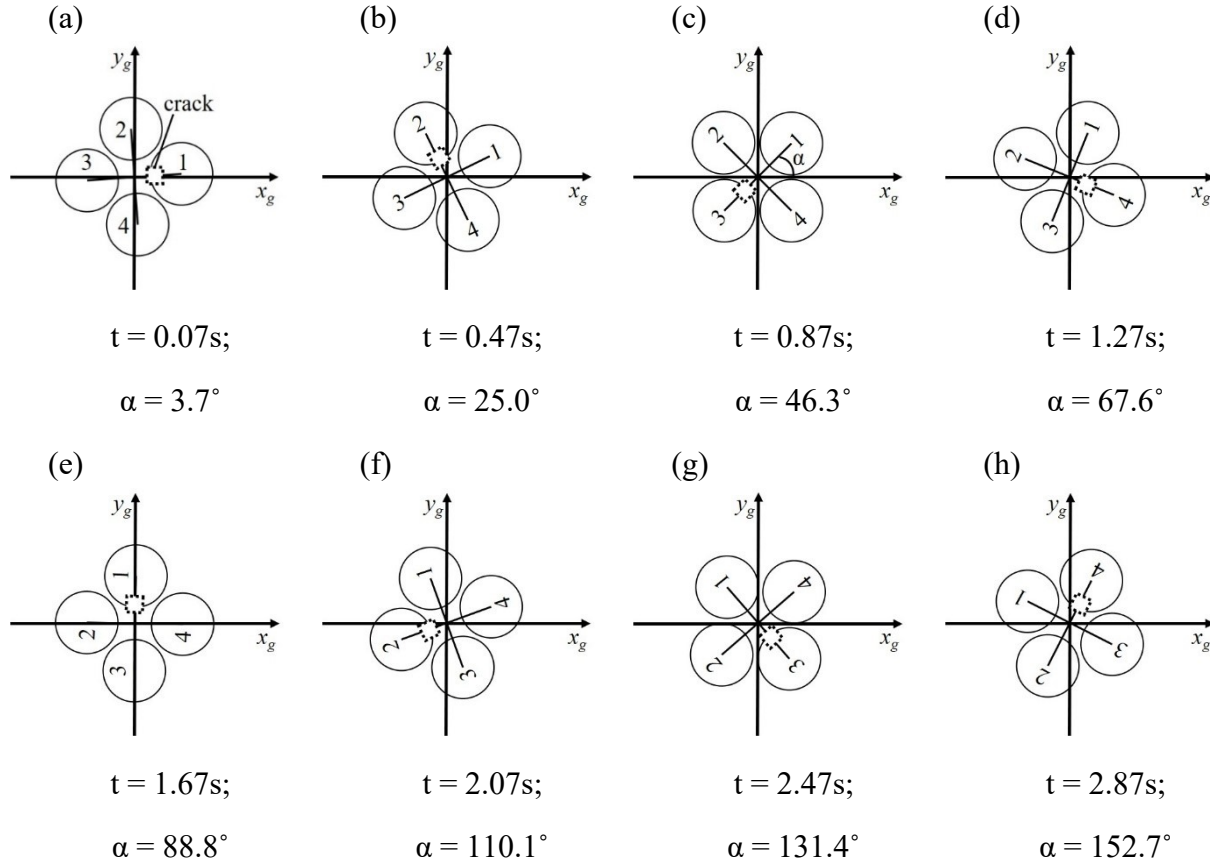


Figure 4.10 Different locations of tooth crack at (a) 0.07 s, (b) 0.47 s, (c) 0.84 s, (d) 1.24 s, (e) 1.64 s, (f) 2.04 s, (g) 2.44 s, and (h) 2.84 s.

All the vibration displacements caused by gear cracks can be decomposed into the  $x_g$  component and the  $y_g$  component. Figure 4.11 shows the decomposed  $x_g$  component and  $y_g$  component based on Figure 4.10 (b), where the red line in Figure 4.11 is the vibration direction of the planet gear, and the dash lines are the  $x_g$  component and  $y_g$  component. According to Figures 4.10 and 4.11, we have the following conclusions:

- (1) According to Figure 4.10 (a) and Figure 4.11, in this case, the carrier angle is  $3.7^\circ$  at the operating time 0.07 s, which means the meshing force is decomposed based on the  $y_g$  component rather than the  $x_g$  component because the meshing force is almost parallel to the  $y_g$  direction.
- (2) According to Figure 4.10 (b) and Figure 4.11, in this case, the carrier angle is  $25.5^\circ$  at the operating time 0.48 s. From Figure 4.11, the value of the  $x_g$  component is larger than the

value in the  $y_g$  component, which means the amplitude of the vibration signal in the  $x_g$  axis is bigger than that in the  $y_g$  axis.

- (3) According to Figure 4.10 (c) and Figure 4.11, in this case, the  $y_g$  component and the  $x_g$  component for mesh stiffness are roughly the same because the carrier angle is  $46.3^\circ$  at the operating time 0.87 s, which means the effect of the sun-gear crack is roughly the same in the  $x_g$  axis and the  $y_g$  axis.
- (4) According to Figure 4.10 (d) and Figure 4.11, in this case, the displacement is vertical to the  $y_g$  axis at the operating time 1.66 s. Thus, no effect of tooth crack between 1.5 s to 2 s was distinguished in  $y_{signal}$ .

Similar to conclusion (1) through conclusion (4), the same conclusions are given in scenarios (e), (f), (g), and (h) in Figure 4.10, which are omitted here due to limited space.

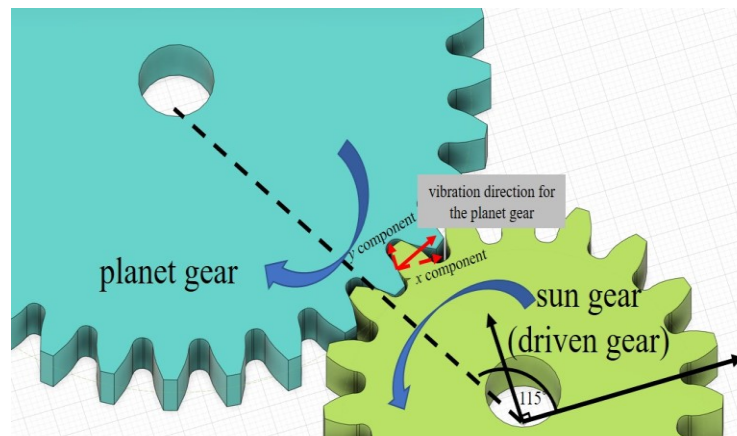


Figure 4.11 Schematic diagram of displacement decomposition when  $t = 0.47s$ .

Considering the scenario of a 50% gear crack (at the bottom) in Figures 4.9 (k, l), to illustrate the vibration directions (i.e., positive and negative) of displacement, the direction analysis with four quadrants during tooth meshing will be introduced to illustrate the vibration directions (i.e., positive and negative) of displacement. Figure 4.11 shows the schematic diagram of the direction analysis with four quadrants, where the quadrants are determined via the meshing location of the planet-gear and the sun-gear with a crack failure.

According to simulated results in Figures 4.9 (k, l) and the schematic diagram of the direction analysis in Figure 4.11, we have the following conclusions:

- (1) When the meshing location of the planet gear and the sun gear with a crack failure is placed in Quadrant I, the corresponding times in Figures 4.9 (k, l) are 0.07 s, 1.66 s, and 2.86 s, the displacement of planet gear in the  $x_g$  axis is positive. The displacement in the  $y_g$  axis is negative.
- (2) When the meshing location of the planet gear and the sun gear with a crack failure is placed in Quadrant II, the corresponding time in Figures 4.9 (k, l) is 0.48 s. The displacements of the planet gear in the  $x$  axis and  $y$  axis are positive.
- (3) When the meshing location of the planet gear and the sun gear with crack failure is placed in Quadrant III, the corresponding times in Figures 4.9 (k, l) are 0.87 s and 2.06 s. The displacement of the planet gear in the  $y$  axis is positive, while the displacement in the  $x$  axis is negative.
- (4) When the meshing location of the planet gear and the sun gear with a crack failure is placed in Quadrant IV, the corresponding times in Figures 4.9 (k, l) are 1.27 s and 2.46 s. The displacements of the planet gear in the  $x$  axis and  $y$  axis are negative.

Figure 4.12 replots the scenario of a 50% crack level that has been displayed in Figure 4.9. The marked points at Q1, Q2, Q3, and Q4 mean the tooth crack is encountered in Quadrants I, II, III, and IV, respectively.

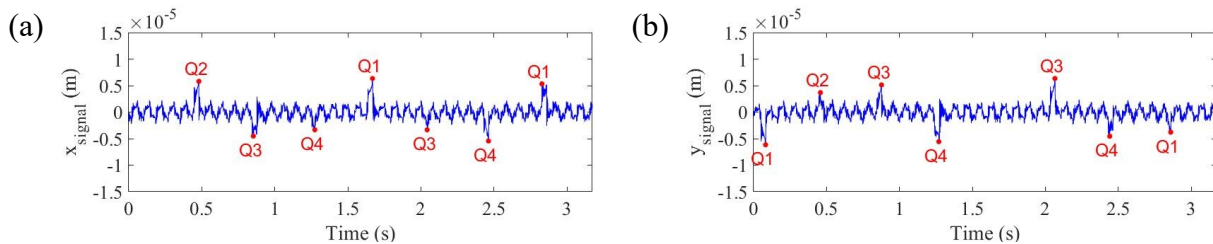


Figure 4.12 Vibration signal of the planet gear with a 50% sun-gear crack without clearance in (a) the  $x_g$  direction and (b) the  $y_g$  direction.

In addition, the deterioration indicators or crack levels in the frequency domain will be considered. Following Eq. (3.2), where  $f_s$  is the sun-gear rotating frequency, and coefficients  $Z_s$

and  $Z_p$  denote the numbers of teeth for the sun gear and the planet gear, respectively. Thus, the mesh frequency ( $f_m$ ) is obtained with the value 11.970 Hz. Figure 4.13 shows the frequency spectrums of vibration displacements with different crack levels without clearances. We observe the frequency spectrum in  $x_{signal}$  (left column) is similar to the frequency spectrum in  $y_{signal}$  (right column).

From Figure 4.13, it can be noted that the gear meshing frequency  $f_m$  and its harmonics  $3f_m$ ,  $7f_m$ , and  $9f_m$  can be clearly detected in the frequency domain. When the tooth crack level increases from 0% to 50%, we observe: (1) the magnitude of  $f_m$  is increased from  $0.96 \times 10^{-6}$  in Figure 4.13 (a) to  $1.09 \times 10^{-6}$  in Figure 4.13 (k); and (2) the noise from 0 to  $f_m$  is significantly increased with the growth of the crack level.

Furthermore, two health indicators, the RMS and kurtosis indices, will be employed to illustrate the degradation process of a tooth crack. Figure 4.14 illustrates the RMS and kurtosis indices of the vibration signal for the planetary gearbox when the crack level is 0%, 10%, 20%, 30%, 40%, and 50%, without considering bearing clearance. In Figure 4.14, the solid line represents the RMS and kurtosis indices in the  $x_g$  direction, while the dashed line represents the RMS and kurtosis indices in the  $y_g$  direction. It is observed (1) the RMS in the  $x_g$  and  $y_g$  directions are almost the same, and it is increased from  $1.02 \times 10^{-6}$  to  $1.35 \times 10^{-6}$  with the growth of the tooth crack level from 0% to 50% in the  $x_g$  direction; and (2) the Kurtosis index in the  $x_g$  and  $y_g$  directions are almost the same, and it increases from 2.05 to 5.41 with the growth of the tooth crack level from 0% to 50% in the  $x_g$  direction.

In summary, it can be concluded that the vibration direction; vibration amplitude, including displacement and basic frequency; and sideband distribution, as well as health indicators, are affected by the gear crack levels in the time domain and the frequency domain. The above section focuses on the dynamic analysis of the planetary gearbox without considering the bearing clearance. The following three sections will focus on the dynamic analysis of the planetary gearbox with bearing clearance.

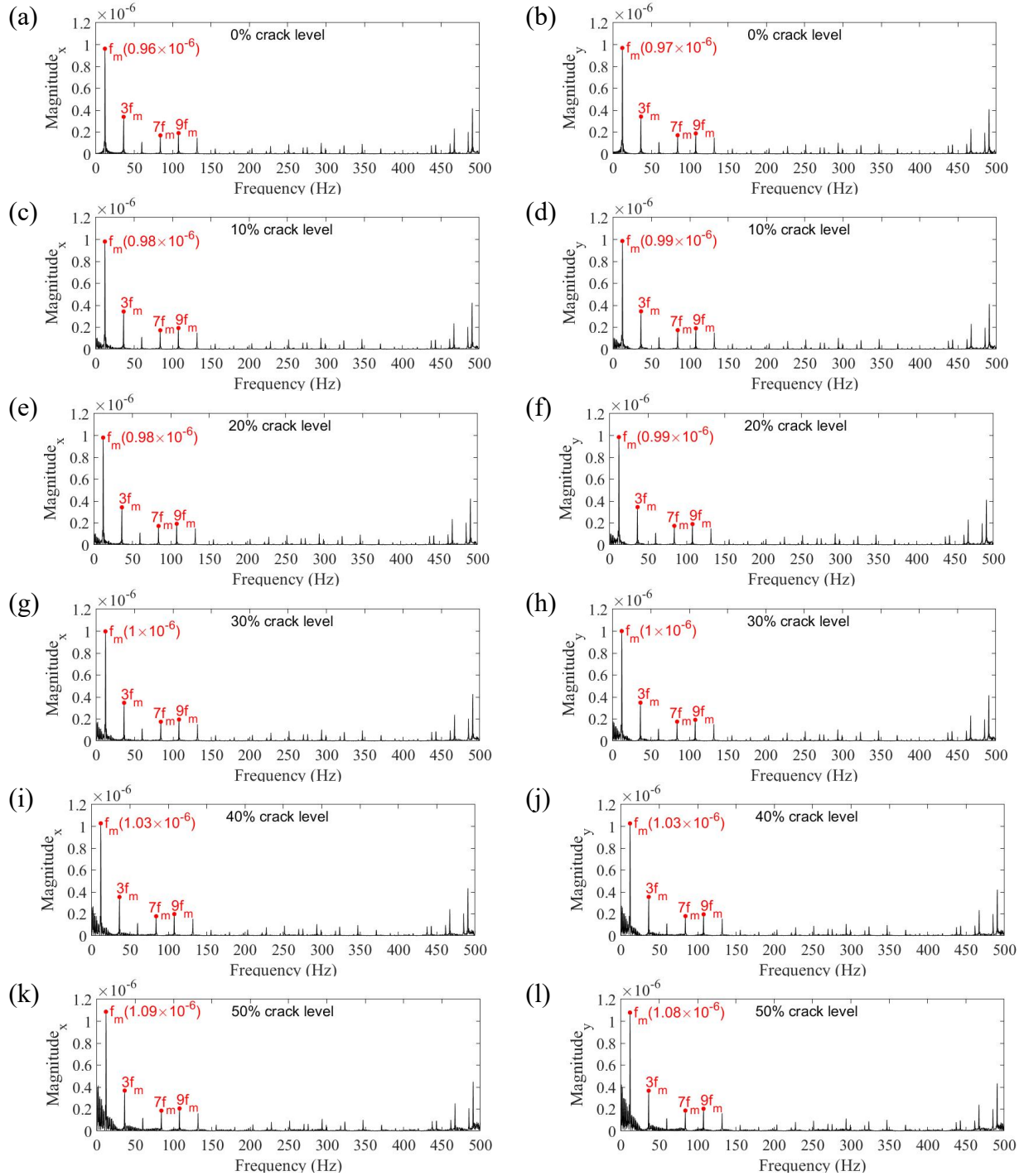


Figure 4.13 Frequency spectrum in  $x_g$  direction with (a) 0%, (c) 10%, (e) 20%, (g) 30%, (i) 40%, and (k) 50% sun-gear tooth crack; and in  $y_g$  direction with (b) 0%, (d) 10%, (f) 20%, (h) 30%, (j) 40%, and (l) 50% sun-gear tooth crack.

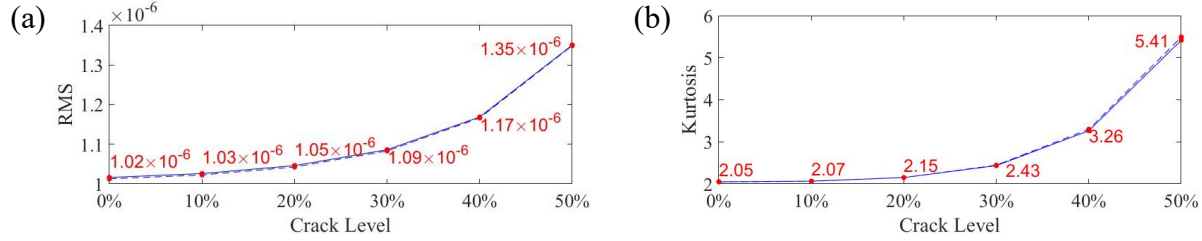


Figure 4.14 (a) RMS and (b) kurtosis of the vibration signal for the planetary gearbox with 0%, 10%, 20%, 30%, 40%, and 50% crack levels.

### 4.3. Dynamic Modeling with only One Type of Bearing Clearance

It should be highlighted that the dynamic response model is referred to the literature of Liang et al. [32]; however a significant factor, namely bearing clearance, was not considered in the literature of Liang et al. [32]. To fill this gap, in this chapter, we will consider the bearing clearance with regards to the main components of the planetary gearbox. We have described in Chapter 3 our improvements on reported differential equations addressing the bearing clearance effects and we have improved the Matlab code provided by Dr. Xihui Liang by taking into consideration of these bearing clearance effects. With the improved Matlab code, we have generated the dynamic responses when a single type of bearing clearance is non-zero under various length values of the sun gear crack in this section.

Section 4.2 analyses the effect of a sun-gear crack with a planetary gear model without any bearing clearance (i.e.,  $\Delta_c$ ,  $\Delta_s$ , and  $\Delta_p = 0$ ). In this subsection, the dynamic response effect with only one kind of bearing clearance (e.g., carrier bearing clearance of 0.08 mm, sun-gear bearing clearance of 0.08 mm, or planet-gear bearing clearance of 0.035 mm) will be discussed in detail.

#### 4.3.1. Case 2: Planet-Gear Bearing Clearance

In this section, we assume that only the four planet-gear bearings have non-zero clearance values. According to Table 3.3 and Table 3.4, the bearing clearance  $\Delta_p$  of the planet gear is determined with 0.035 mm (i.e., the minimum values in normal scenarios that follow the standards of NTN [71]). Figure 4.15 displays the schematic diagram of the relative displacement between the planet gear and the carrier. In this figure, the solid line shows the original location of the planet gear without any displacement. Point **A** is the contact center between the carrier and the planet gear, and point **B** is the center of the planet gear. If there is no displacement, the locations of points **A** and **B** will overlap at one point. During vibration, the location of these components will move to

the profile of the dash line. That is, point  $A$  moves to point  $A'$ , and point  $B$  moves to point  $B'$ , where the line between  $A'$  and  $B'$  shows the relative displacement  $\delta_{cp1}$ .

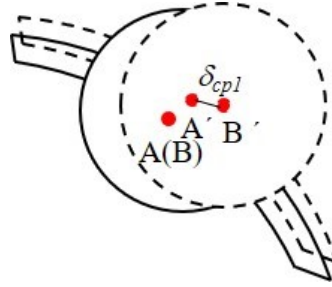


Figure 4.15 Schematic diagram of relative displacement between the planet gear and the carrier.

Figure 4.16 shows the relative displacements ( $\delta_{cp1}$ ,  $\delta_{cp2}$ ,  $\delta_{cp3}$ , and  $\delta_{cp4}$ ) between the carrier and each planet gear. The left figures (a, c, e, and g) illustrate the relative displacement under a 0% sun-gear crack condition, and the right figures (b, d, f, and h) show the relative displacement under a 50% sun-gear crack condition. The dashed line shows the clearance of the planet bearing, which is  $0.35 \times 10^{-4}$  m, and it is smaller than the stable relative displacement around  $1.1 \times 10^{-4}$  m. Furthermore, the trends of relative displacement in the same crack levels are similar to each other. Therefore, the next analysis only focuses on the planet 1 gear, and the other results for the planet 2, 3, and 4 gears are the same as the planet 1 gear. From Figure 4.16, we find the tooth crack level does not affect the average of the relative displacement, and the relative displacement for each planet gear is approximately  $1.1 \times 10^{-4}$  m.

Following the Eqs. (3.10) and (3.11), the bearing forces ( $F_{cpnx}$  and  $F_{cpny}$ ) are determined by the displacement differential  $l = \delta_{cp} - \Delta_p$ . In the scenario of Section 4.1, the  $l = \delta_{cp}$  is due to  $\Delta_p = 0$ . Only Figure 4.17 shows the displacement differential  $l$  for carrier–planet 1 under a 0% and 50% sun-gear crack in (a) and (b), respectively. The other displacement differential is similar to Figure 4.17, which is not shown in this chapter. The simulated results of the four planet-gears indicate the displacement differentials  $l$  are around  $0.75 \times 10^{-4}$  m after considering the planet-gear bearing clearances, which means the planet-gear bearing forces  $F_{cpnx}$  and  $F_{cpny}$  will be not changed with the planet-gear bearing clearances. Thus, the effect of the planet-gear bearing clearances being too small are ignored.

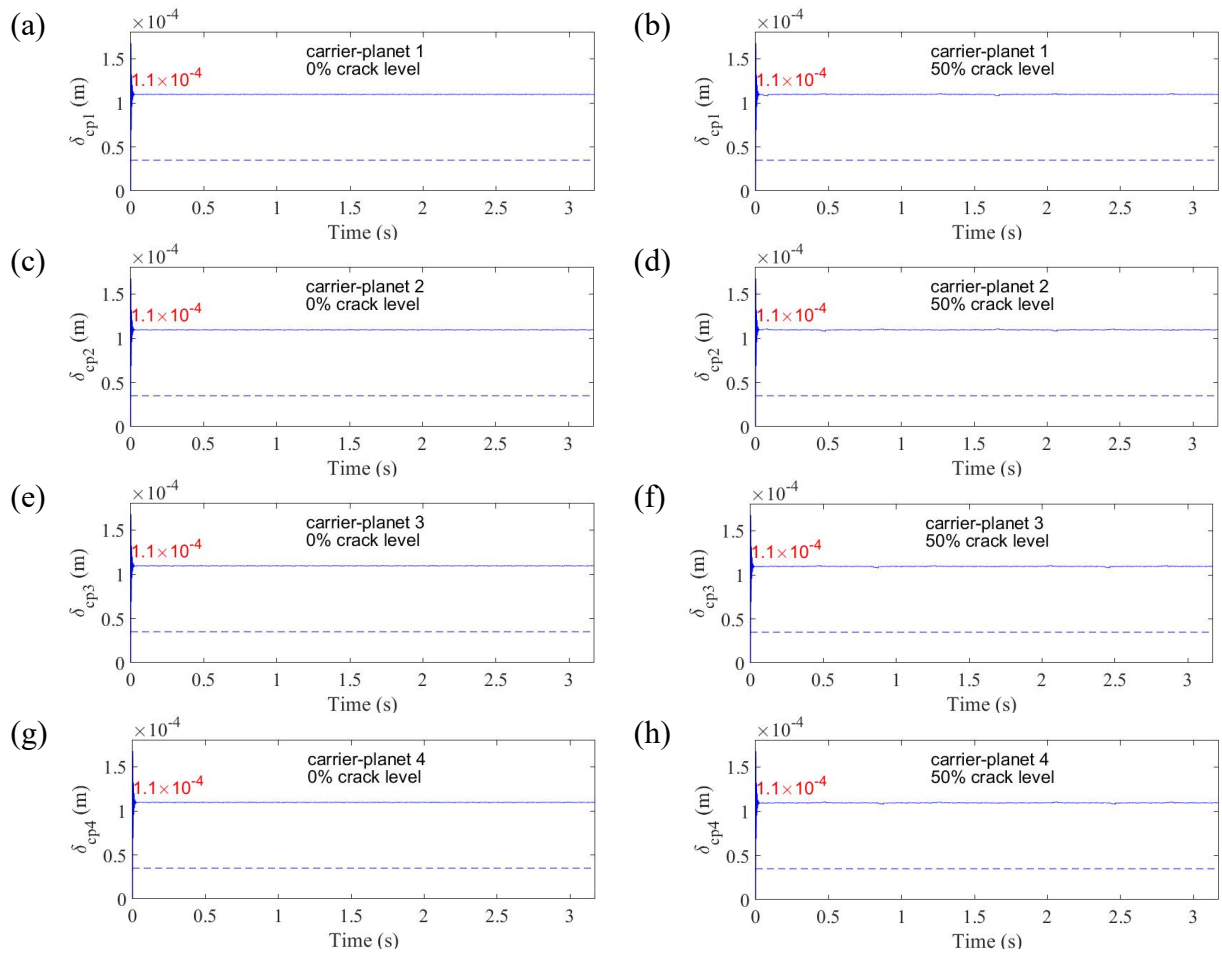


Figure 4.16 Relative displacement between the carrier and (a, b) planet 1, (c, d) planet 2, (e, f) planet 3, and (g, h) planet 4 with 0% and 50%.

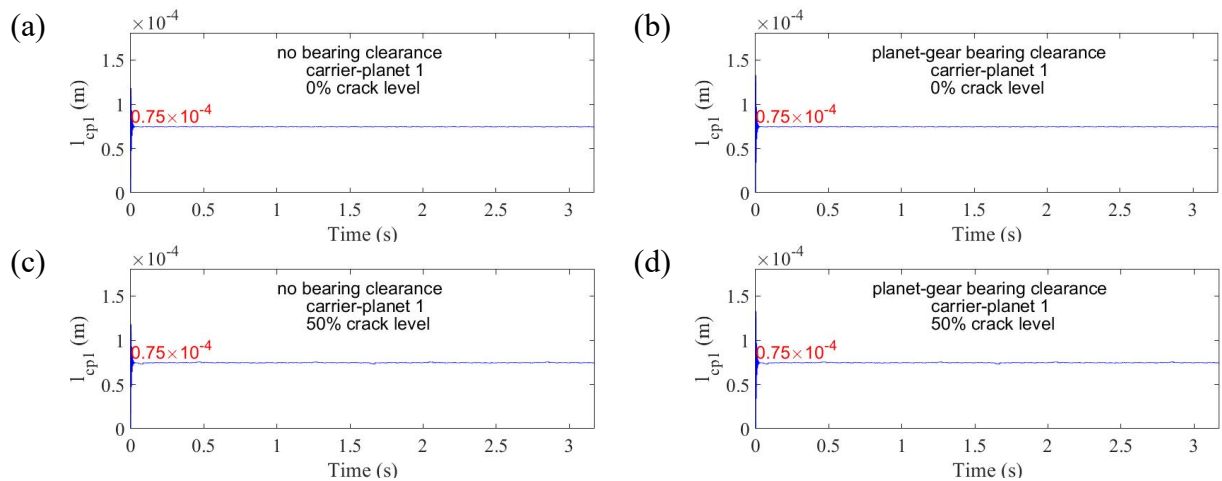


Figure 4.17 Simulated results of the displacement differential  $I$  for carrier-planet 1 considering no clearance with (a) 0% and (c) 50% crack levels; considering planet-gear bearing clearance with (b) 0% and (d) 50% crack levels.

Furthermore, Figure 4.18 shows the vibration signals of all components in the planet gearbox (i.e., carrier, sun-gear, ring-gear, and planet-gear) in a time domain and considering the planet-gear bearing clearance. Similar to the case without planet-gear bearing clearance, it is shown the vibration displacement in the planet gear is much higher than other components, compared to Figure 4.18(g, h) and the other figures (a, b, c, d, e, f). The red dashed line shows the highest displacement value in the  $x_g$  direction. Then, compared with the displacement vibration in Case 1, which does not consider the planet-gear bearing clearance in Figure 4.7, the vibration signals of the carrier, the ring gear, the sun gear, and the planet gear are similar in the  $x_g$  and  $y_g$  directions because the effect of the planet-gear bearing clearance is too small to be considered.

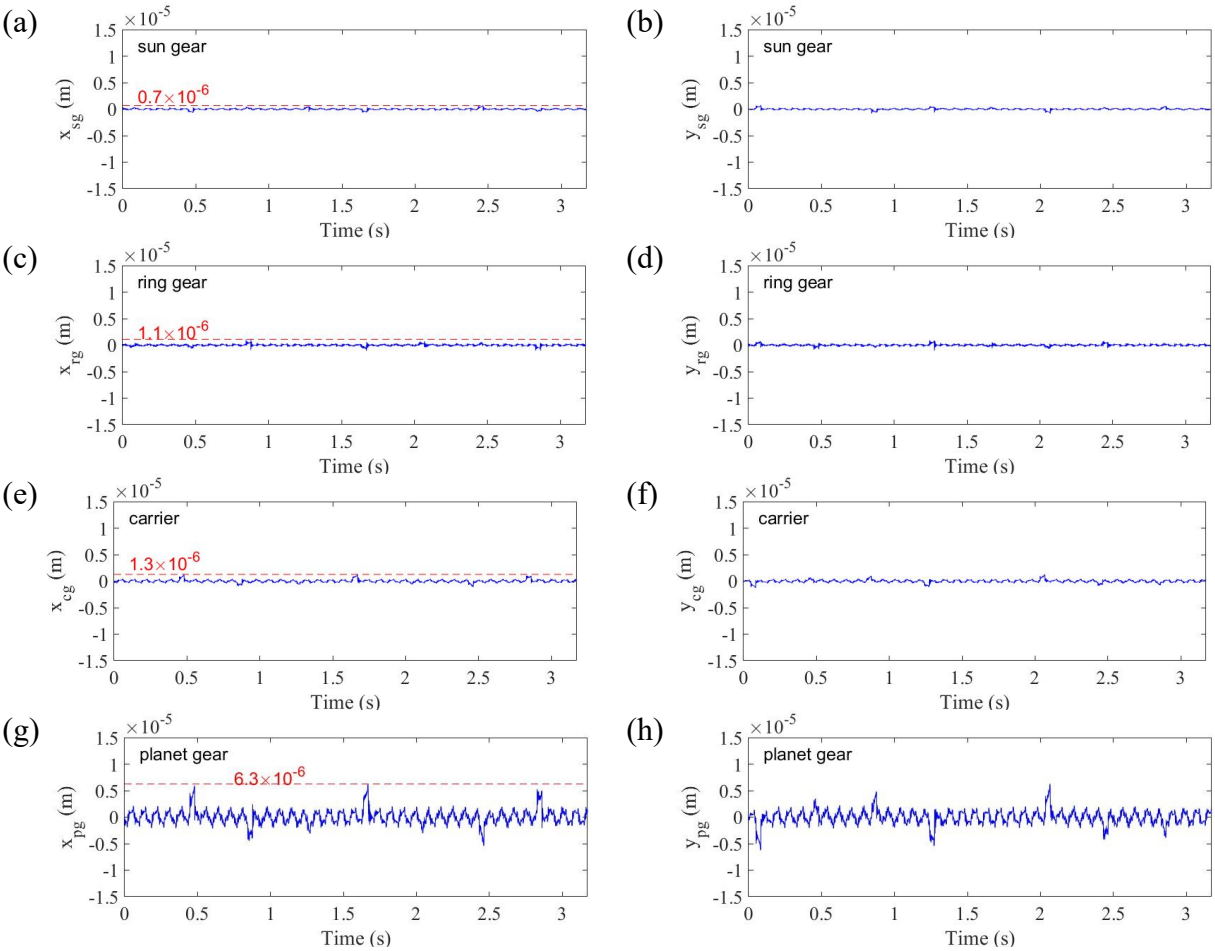


Figure 4.18 Vibration displacement signal of each component with a 50% sun-gear crack with a planet-gear bearing clearance.

Figure 4.19 illustrates the vibration displacement of each planet gear. Compared with Case 1, which did not consider the bearing clearance, we can see the planet-gear bearing clearance

increases the displacement of each planet gear. The maximum displacement is below  $1 \times 10^{-4}$  m in Figure 4.8 without a bearing clearance, while the maximum displacement is between  $1 \times 10^{-4}$  and  $1.5 \times 10^{-4}$  m in Figure 4.19 when considering the planet-gear bearing clearance. However, this phenomenon does not affect the vibration response of the planetary gear set shown in Figure 4.20, based on the limitation of the transmission path equation shown in Eqs. (3.34) and (3.35).

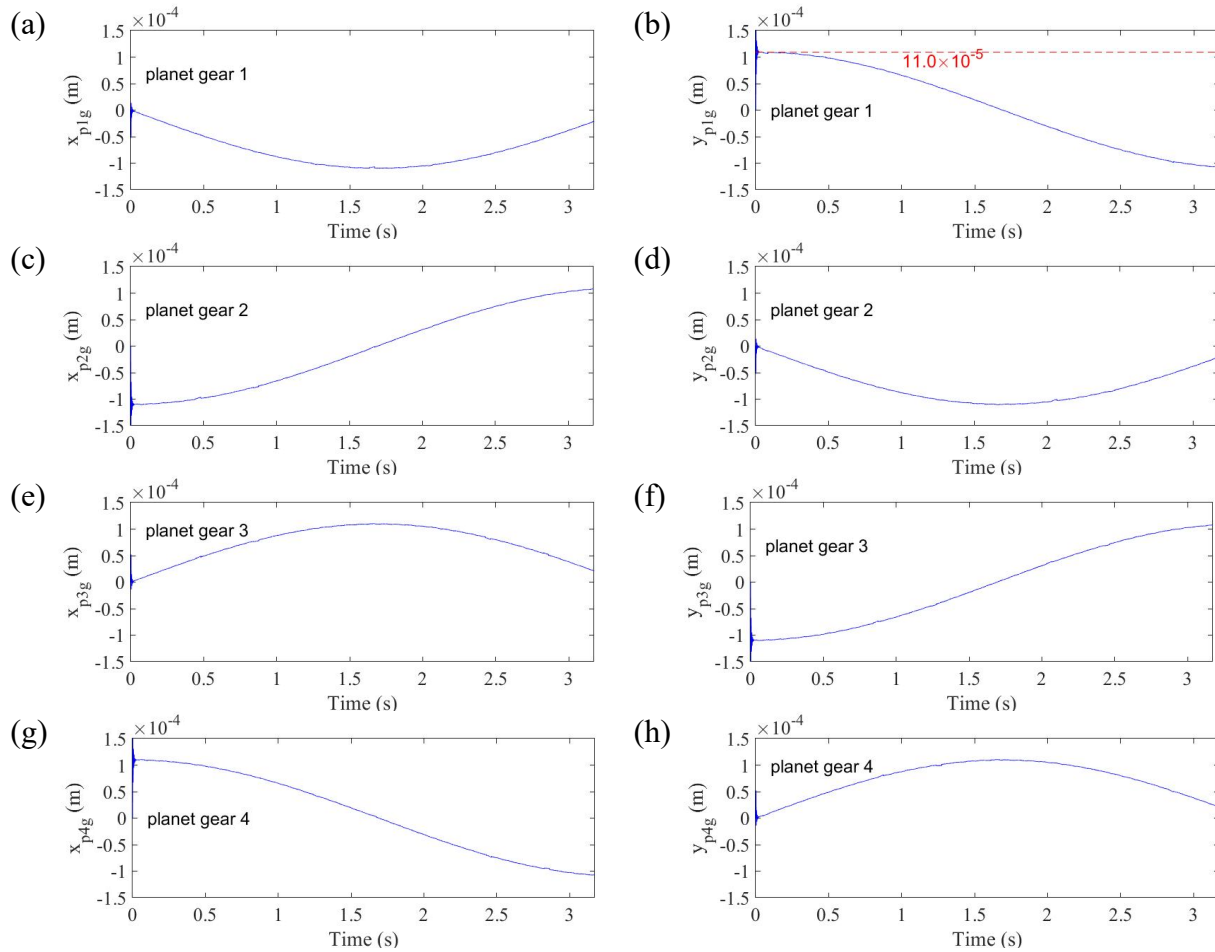


Figure 4.19 Vibration displacement signal in the  $x_g$  direction with a 50% sun-gear crack without clearance.

Furthermore, the simulated vibration response of the planetary gearbox is shown in Figure 20, which is the same as Case 1 without bearing clearance. The red dashed line shows the highest displacement in  $x_{signal}$  with a 50% crack level. The result are as follows: (1) impulse fault signals caused by a tooth crack are easily identified with the increase of a fault crack; (2) the fault impulse intervals are very obvious in  $x_{signal}$ , while the impulses between 1.5 s and 2 s in  $y_{signal}$  are not detected, as shown in Figure 4.9 (l), after considering the planet-gear bearing clearance.

Figure 4.21 shows the frequency spectrum of the planetary gearbox vibration signal with the planet-gear clearance, where the frequency spectrums in the  $x_g$  and  $y_g$  directions are similar to the results in Case 1. From this figure, we find (1) the magnitude of  $f_m$  is increased from  $0.96 \times 10^{-6}$  in Figure 4.21 (a) to  $1.09 \times 10^{-6}$  in Figure 4.21 (k); and (2) the noise from 0 to  $f_m$  is significantly increased with the growth of the crack level, which is similar to Case 1.

Furthermore, Figure 4.22 illustrates the RMS and kurtosis indices of the vibration signal for the planetary gearbox when the crack level is 0%, 10%, 20%, 30%, 40%, and 50% with a bearing clearance. The solid line is the value of RMS and kurtosis in the  $x_g$  direction, while the dashed line is the value of RMS and kurtosis in the  $y_g$  direction. It is obvious that (1) the RMSs in the  $x_g$  and  $y_g$  directions are almost the same, and the values have increased from  $1.04 \times 10^{-6}$  to  $1.36 \times 10^{-6}$  with the growth of the tooth crack level from 0% to 50% in the  $x_g$  direction; and (2) the kurtosis indexes in the  $x_g$  and  $y_g$  directions are almost the same, and the values have increased from 2.1 to 5.44 with the growth of the tooth crack level from 0% to 50% in the  $x_g$  direction. The RMS and kurtosis indices are slightly higher than the results produced in Case 1.

In conclusion, the planet-bearing clearance increases the displacement of each planet gear. The highest displacement of the first planet gear increases by 49% (from  $7.4 \times 10^{-5}$  m without a bearing clearance to  $11 \times 10^{-5}$  m with a planet-gear bearing clearance), comparing Figures 4.8(b) and 4.19(b). It also increases the sum of all displacements of all gearbox components, but it is quite small. The planet-gear bearing clearance only increases by 1.6%, the highest displacement value (from  $6.3 \times 10^{-6}$  m without a bearing clearance to  $6.4 \times 10^{-6}$  m with a planet-gear bearing clearance), comparing Figures 4.9(k) and 4.20(k). Therefore, the planet-gear bearing clearance does not affect the total vibration response very much. Therefore, this clearance factor (i.e., the planet-gear bearing clearance) may be ignored in future dynamic gearbox simulations. This omission will not affect the detection ability much because its influence has been found to be miniscule in this section.

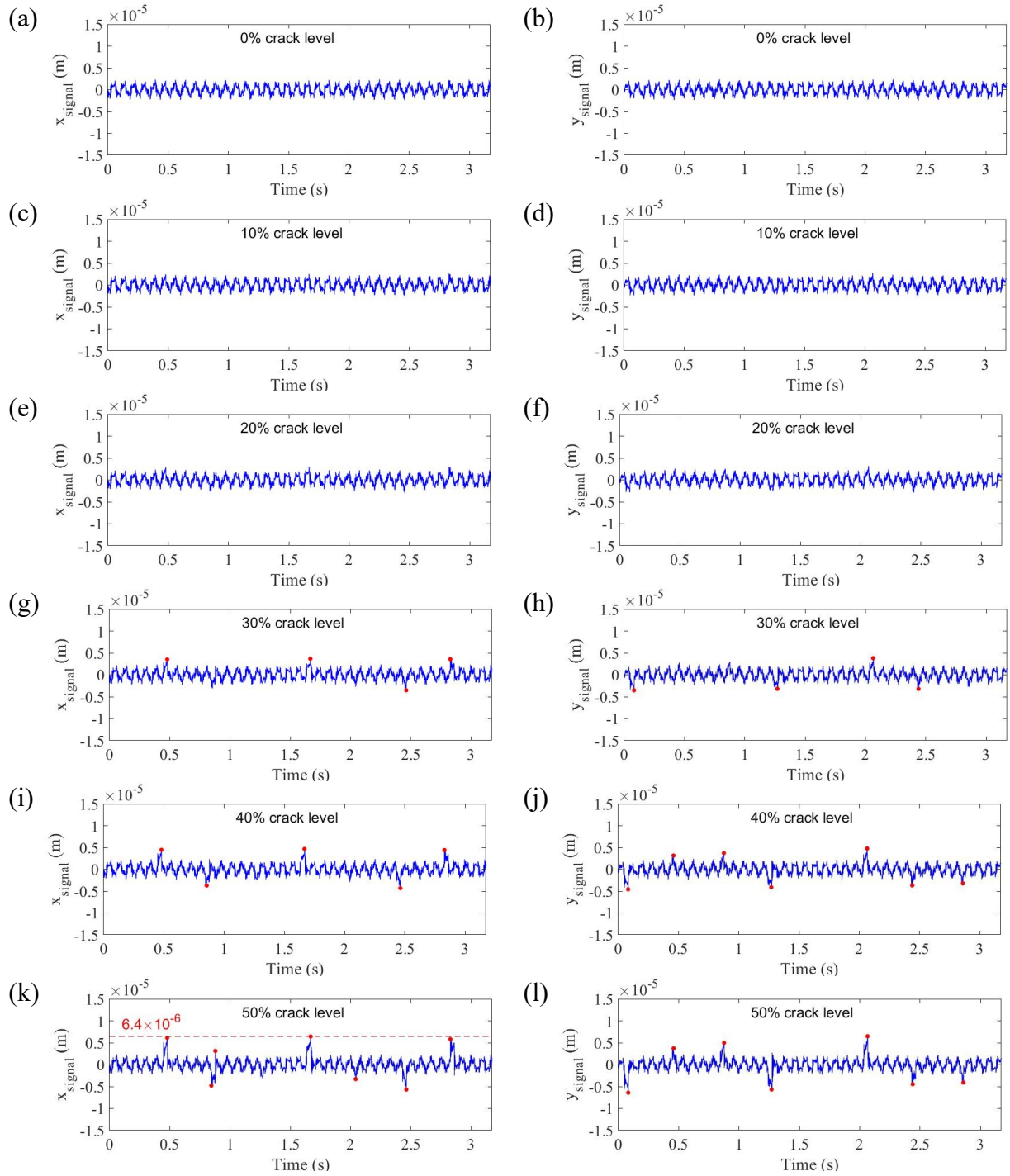


Figure 4.20 Vibration signal of the planetary gearbox in the  $x_g$  direction with (a) 0%, (c) 10%, (e) 20%, (g) 30%, (i) 40%, and (k) 50% sun-gear tooth crack; in the  $y_g$  direction with (b) 0%, (d) 10%, (f) 20%, (h) 30%, (j) 40%, and (l) 50% sun-gear tooth crack considering the planet-gear bearing clearance.

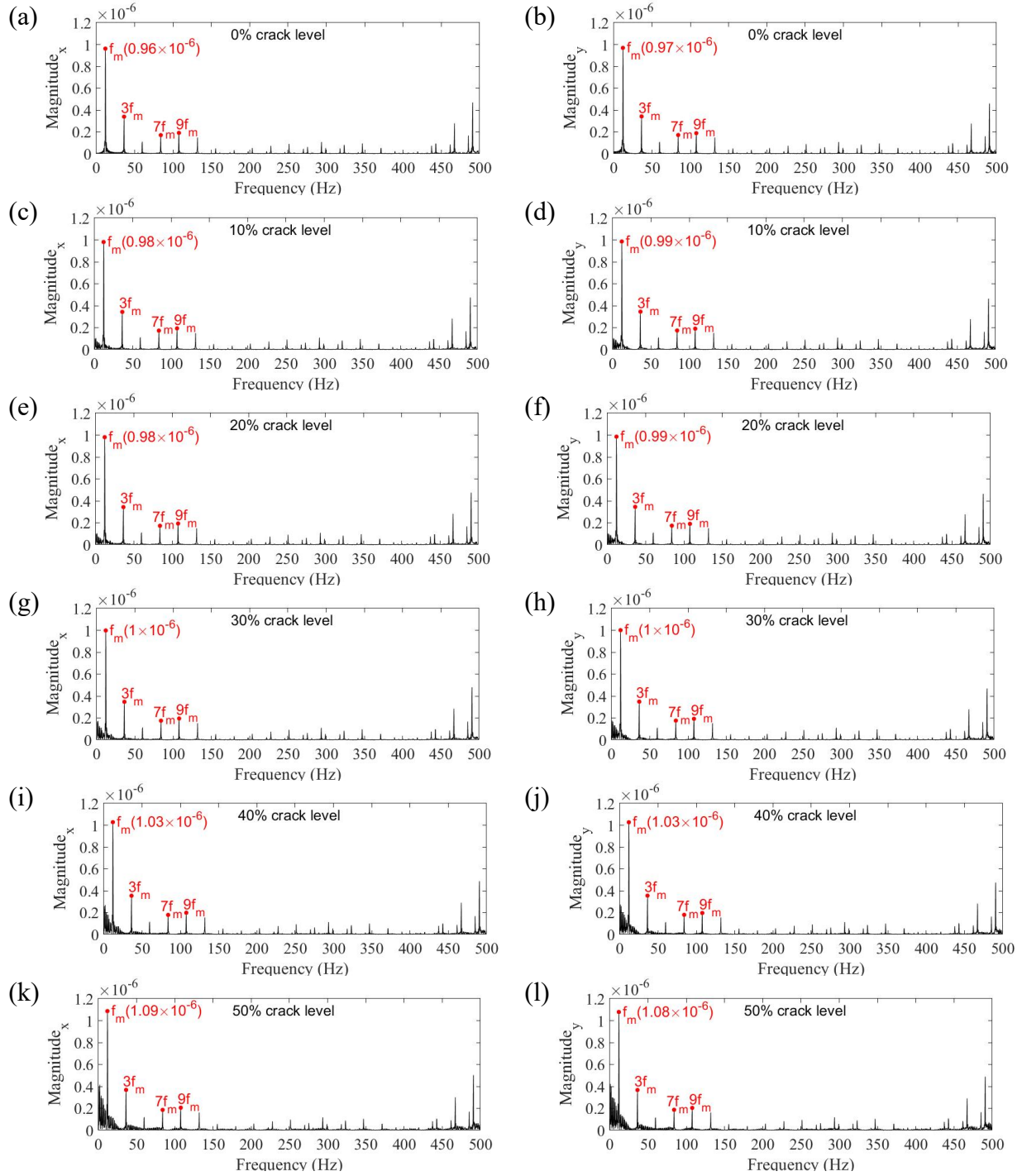


Figure 4.21 Frequency spectrum in the  $xg$  direction with (a) 0%, (c) 10%, (e) 20%, (g) 30%, (i) 40%, and (k) 50% sun-gear tooth crack; in the  $yg$  direction with (b) 0%, (d) 10%, (f) 20%, (h) 30%, (j) 40%, and (l) 50% sun-gear tooth crack.

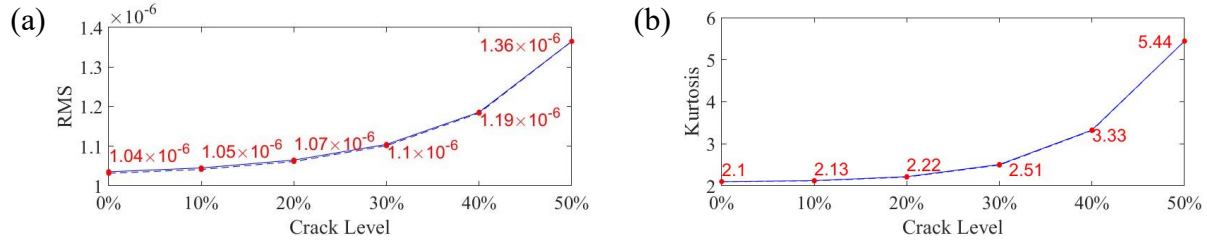


Figure 4.22 (a) RMS and (b) kurtosis of the planetary gearbox vibration signal with 0%, 10%, 20%, 30%, 40%, and 50% crack level considering the planet-gear bearing clearance.

### 4.3.2. Case 3: Sun-Gear Bearing Clearance

In this section, we assume that only the sun-gear bearing has a non-zero clearance. According to Table 3.3 and Table 3.4, the bearing clearance  $\Delta_s$  of the sun gear is 0.08 mm (i.e., the minimum value in normal scenarios following the standards of Timken [70]). Figure 4.23 displays the schematic diagram of the sun-gear displacement. In this figure, the solid line shows the original location of the sun gear without displacement. Point  $A$  is the center of the sun gear. During vibration, the sun gear's location moves to the dashed line (i.e., point  $A$  moves to point  $A'$ , the line between  $A$  and  $A'$  shows the displacement  $\delta_s$ ).

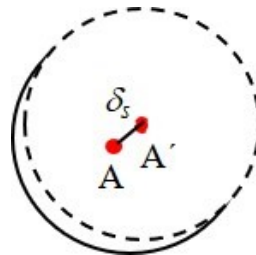


Figure 4.23 Schematic diagram of the relative displacement for the sun gear.

Figure 4.24(a) shows the relative displacements ( $\delta_s$ ) without a clearance for a 0% crack level, (b) shows the relative displacements ( $\delta_s$ ) with a sun-gear bearing clearance for a 0% crack level, (c) shows the relative displacements ( $\delta_s$ ) without clearance for a 50% crack level, and (d) shows the relative displacements ( $\delta_s$ ) with a sun-gear bearing clearance for a 50% crack level. From this figure, it is obvious (1) the sun-gear bearing clearance (0.08 mm) is larger than the displacement of the sun gear, and (2) the sun-gear bearing clearance increases the displacement. The average sun-gear displacement increases from  $0.1 \times 10^{-6}$  m to  $1 \times 10^{-6}$  m, and the highest displacement with a 50% crack level grows from  $0.81 \times 10^{-6}$  to  $4.94 \times 10^{-6}$ . Finally, (3) the tooth crack creates the impulse in the sun-gear displacement.

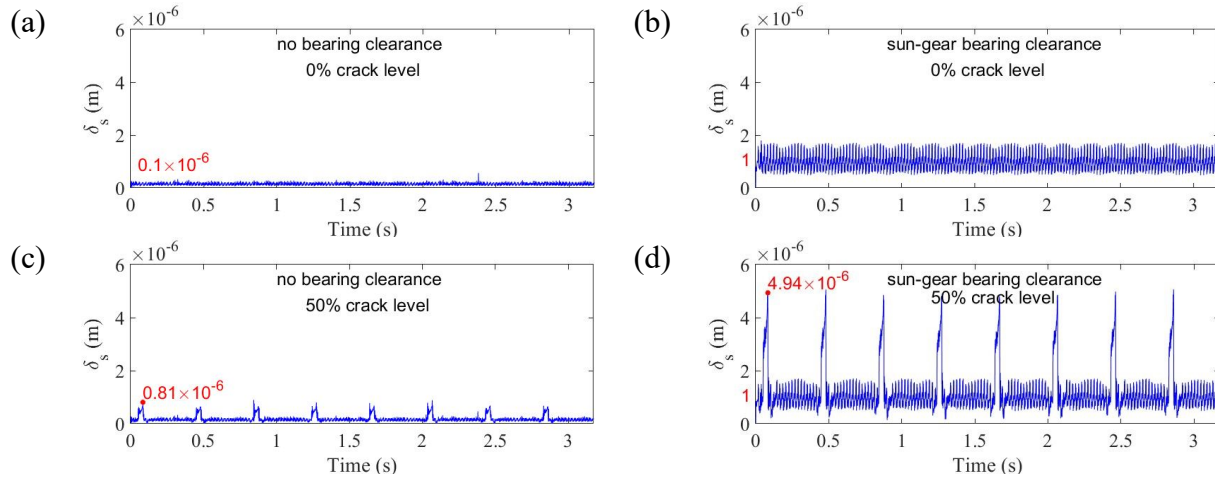


Figure 4.24 Relative displacement of the sun gear (a, c) without a bearing clearance for 0% and a 50% crack level and (b, d) with a sun-gear bearing clearance for 0% and 50% crack levels.

Figure 4.25(a, b) shows the sun-gear displacement in the  $x_g$  and  $y_g$  directions. Figure 4.25(c, d) shows the ring gear displacement in the  $x_g$  and  $y_g$  directions. Figure 4.25(e, f) shows the carrier displacement in the  $x_g$  and  $y_g$  directions. Finally, Figure 4.25(g, h) shows the total planet-gear displacement in the  $x_g$  and  $y_g$  directions. Furthermore, the red dashed line shows the highest displacement value in the  $x_g$  direction. From Figure 4.25, several interesting phenomena are found: (1) the sun-gear vibration displacement is larger than the displacements of the other components; (2) the directions of the sun-gear displacement are different during meshing time. For example, approximately 0.5 s, the direction of the sun gear in the  $x_g$  axis is negative, while approximately 2.5 s the direction in the  $x_g$  axis is positive. The causes of the different displacement vibrations are analysed in Case 1 without a bearing clearance. Finally, (3) Figures 4.7(a) and (c) in Case 1, without a bearing clearance, shows the ring-gear displacement is similar to the sun gear. Then, after considering the sun-gear bearing clearance, the ring-gear displacement is lower than the sun gear, as shown in Figures 4.18(a) and (c). The phenomena (3) is closer to the real system for the planetary gear set because the ring gear is fixed in this thesis, and the ring gear displacement should be lower than the vibration of the sun gear.

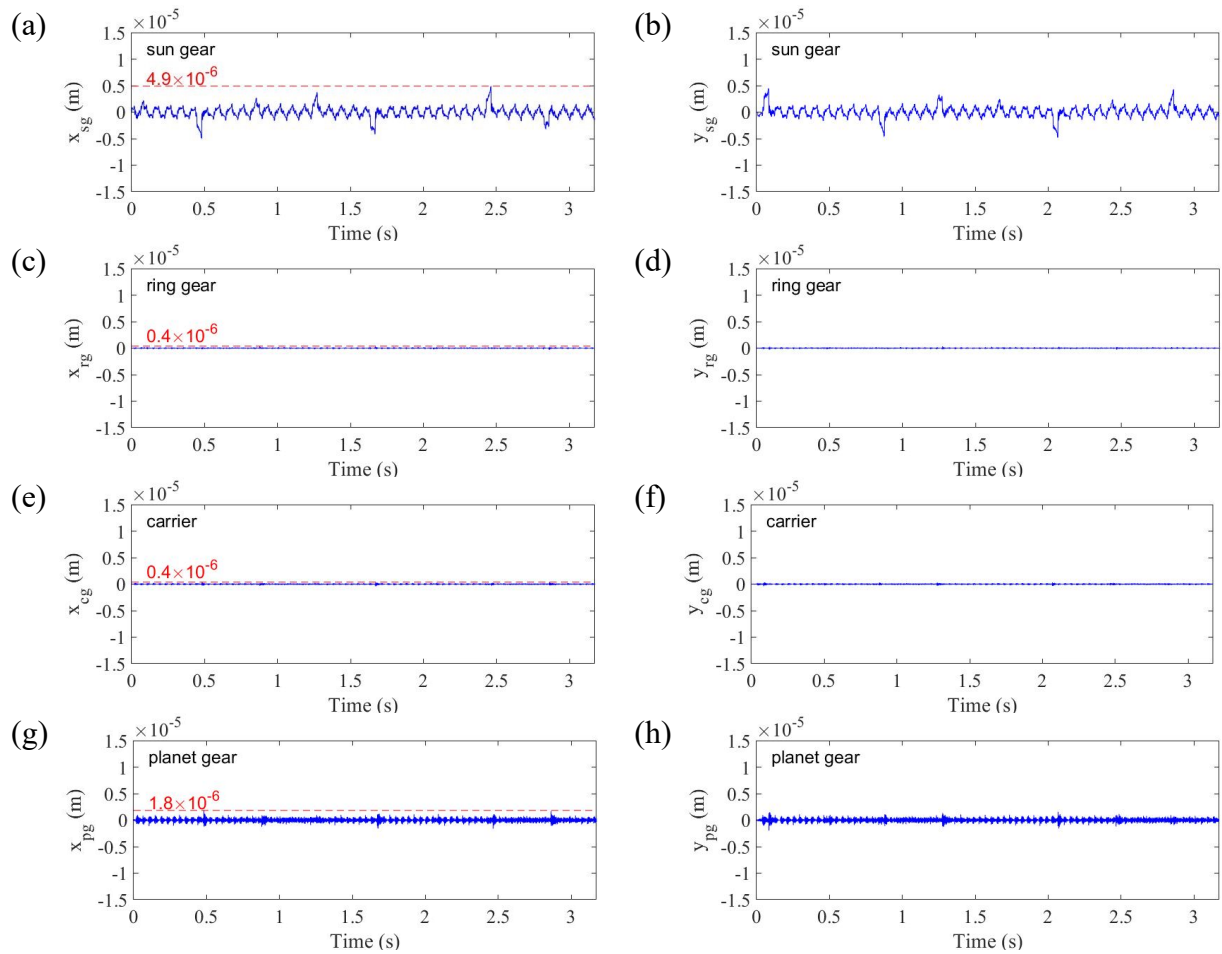


Figure 4.25 Vibration displacement of each component with a 50% sun-gear crack with a sun-gear bearing clearance.

Furthermore, the simulated vibration response of the planetary gearbox is shown in Figure 4.26, while the red dashed line shows the highest displacement in  $x_{signal}$  with a 50% crack level. The results are as follows: (1) impulse fault signals caused by a tooth crack are easily identified with the increase of a fault crack; and (2) a fault impulse between 0.5 s and 1 s in  $x_{signal}$  is not detected, compared with Figure 4.9(k) and 4.26(k), while a fault impulse between 1 s and 2 s in  $y_{signal}$  is not detected, compared with Figure 4.9(l) and 4.26(l) because of the sun-gear displacement decomposition, which is similar to the planet-gear displacement decomposition shown in Figure 4.11.

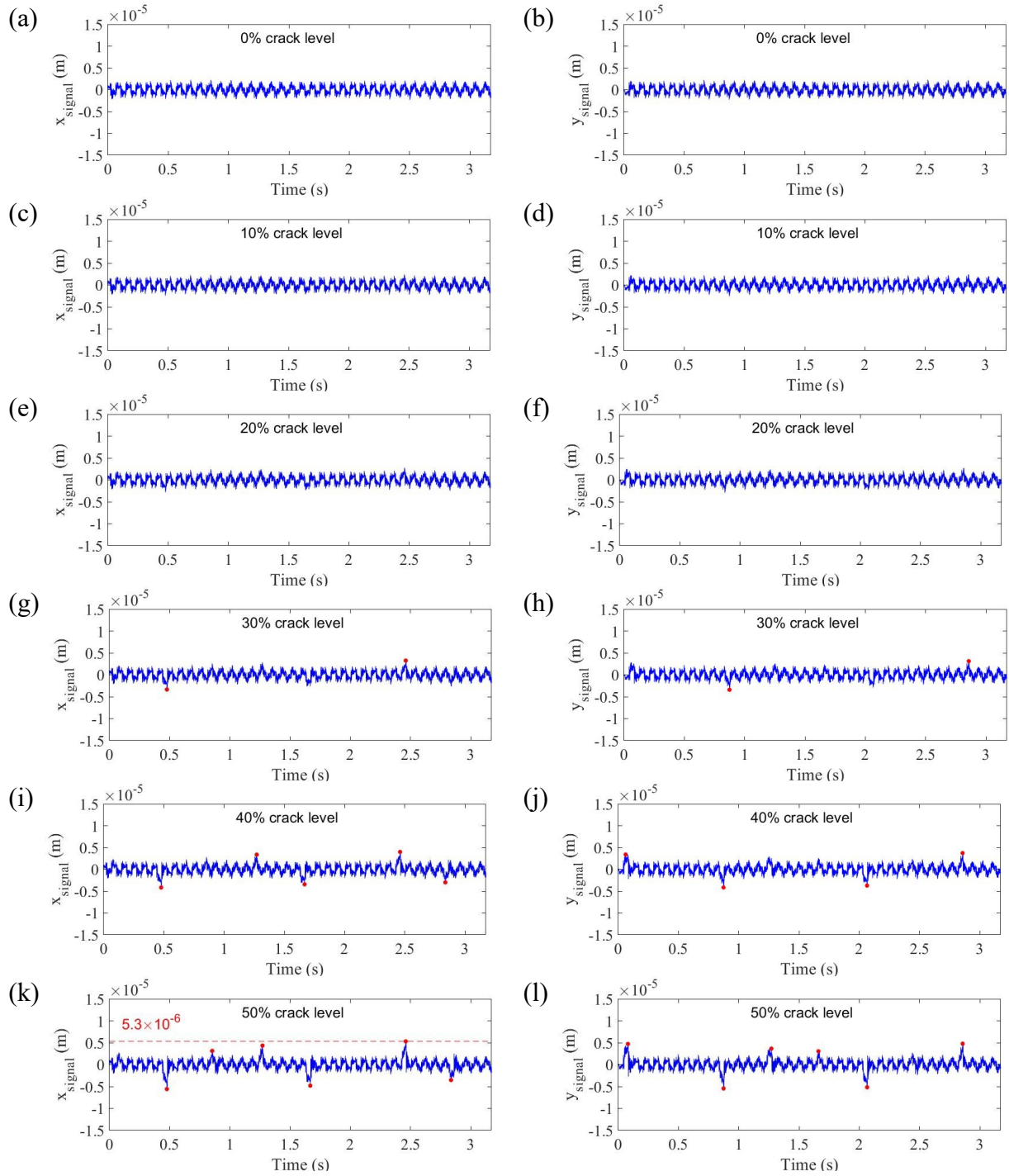


Figure 4.26 Vibration signal of the planetary gearbox in the  $x_g$  direction with (a) 0%, (c) 10%, (e) 20%, (g) 30%, (i) 40%, and (k) 50% sun-gear tooth crack; in the  $y_g$  direction with (b) 0%, (d) 10%, (f) 20%, (h) 30%, (j) 40%, and (l) 50% sun-gear tooth crack, considering a sun-gear bearing clearance.

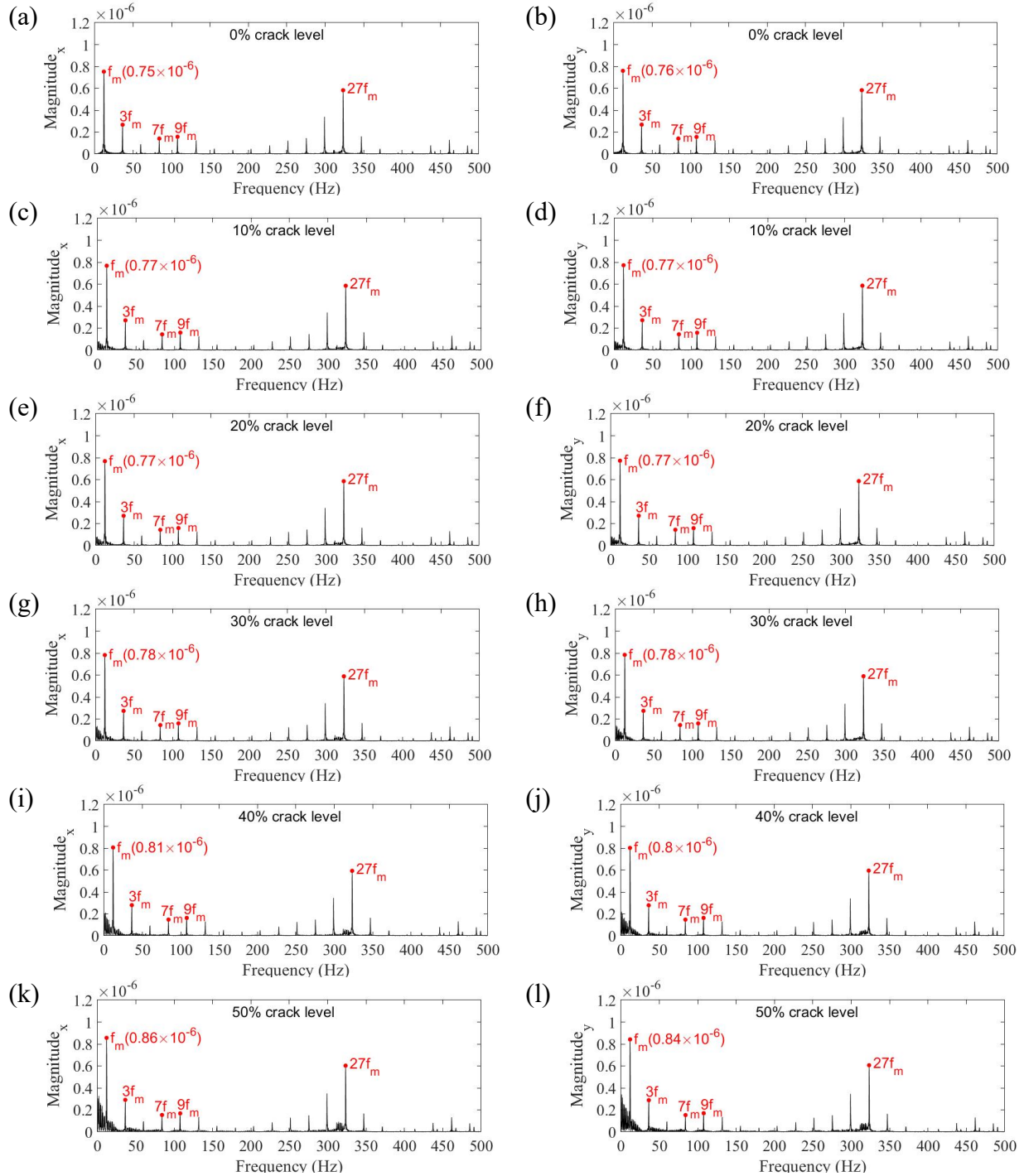


Figure 4.27 Frequency spectrum in the  $x_g$  direction with (a) 0%, (c) 10%, (e) 20%, (g) 30%, (i) 40%, and (k) 50% sun-gear tooth crack; in the  $y_g$  direction with (b) 0%, (d) 10%, (f) 20%, (h) 30%, (j) 40%, and (l) 50% sun-gear tooth crack.

The frequency spectrum with a sun-gear clearance in Figure 4.27 shows the frequencies in the  $x_g$  and  $y_g$  directions are similar. From this figure, we can observe (1) the magnitude of  $f_m$  is increased from  $0.75 \times 10^{-6}$  in Figure 4.27(a) to  $0.86 \times 10^{-6}$  in Figure 4.27(k), and (2) the noise around  $f_m$  and  $27 f_m$  is significantly increased with the growth of the crack level.

Furthermore, Figure 4.28 illustrates the RMS and kurtosis indices of the vibration signal for the planetary gearbox when the crack level is 0%, 10%, 20%, 30%, 40%, and 50% without a bearing clearance. The line is the RMS in the  $x_g$  direction, while the dashed line is the RMS in the  $y_g$  direction. It is obvious that (1) the RMS in the  $x_g$  and  $y_g$  directions is almost the same, and it increases from  $0.92 \times 10^{-6}$  to  $1.16 \times 10^{-6}$  with the growth of the tooth crack level from 0% to 50% in the  $x_g$  direction; and (2) the kurtosis indices in the  $x_g$  and  $y_g$  directions are almost the same below the 30% crack level. It increases from 2.27 to 4.54 in the  $x_g$  direction and from 2.27 to 4.71 in the  $y_g$  direction with the growth of the tooth crack level from 0% to 50%.

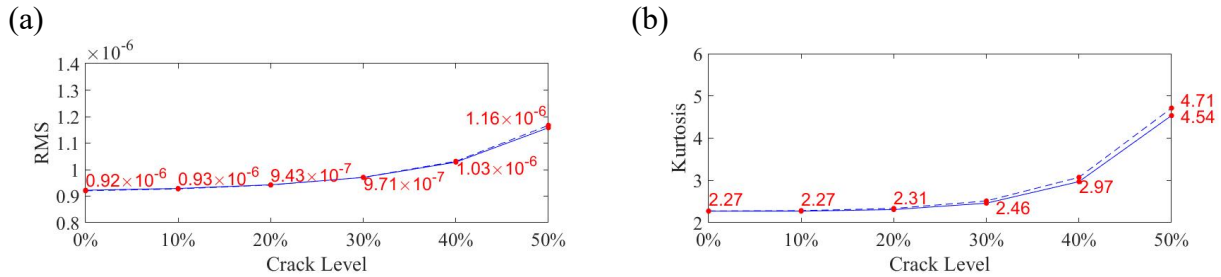


Figure 4.28 (a) RMS and (b) kurtosis of the vibration signal for the planetary gearbox with 0%, 10%, 20%, 30%, 40%, and 50% crack level considering the sun-gear bearing clearance.

In conclusion, the sun-gear bearing clearance increases the highest displacement for the sun gear by six times (from  $0.7 \times 10^{-6}$  m without any bearing clearance to  $4.9 \times 10^{-6}$  m with a sun-gear bearing clearance), while it reduces the highest ring-gear displacement by 60% (from  $1 \times 10^{-6}$  m to  $0.4 \times 10^{-6}$  m), the highest carrier displacement by 67% (from  $1.2 \times 10^{-6}$  m to  $0.4 \times 10^{-6}$  m), and the highest value for the sum displacement of planet gears by 70% (from  $6.2 \times 10^{-6}$  m to  $1.8 \times 10^{-6}$  m), as shown in Figures 4.7 and 4.25. It reduces the highest displacement by 16% (from  $6.3 \times 10^{-6}$  m to  $5.3 \times 10^{-6}$  m) for the sum of all displacements, comparing Figures 4.9(k) and 4.26(k). Therefore, the sun-gear bearing clearance can reduce the magnitude of  $f_m$  (a decrease from  $1.09 \times 10^{-6}$  to  $0.86 \times 10^{-6}$  with a 50% crack level), while it increases from  $0.9 \times 10^{-7}$  to  $6.0 \times 10^{-7}$  in magnitude for  $27 f_m$  (Figure 4.27) compared with Case 1 without any bearing clearance (Figure

4.13). Thus, a tooth crack can create noise around  $f_m$  and  $27 f_m$  (Figure 4.27). This means that the sun-gear bearing clearance factor cannot be ignored in future dynamic simulations of gearboxes.

#### 4.3.3. Case 4: Carrier Bearing Clearance

In this section, we assume that only the carrier bearing has a non-zero clearance. According to Table 3.3 and Table 3.4, the carrier bearing clearance  $\Delta_c$  is 0.08 mm (i.e., the minimum value in normal scenarios following the standards of Timken and NTN). Figure 4.29 displays the schematic diagram of the displacement for the carrier. In this figure, the solid line shows the original location of the sun gear without displacement. Point  $C$  is the center of the carrier. During vibration, the location of the carrier moves to the dashed line. (i.e., point  $C$  moves to point  $C'$ , the line between  $C$  and  $C'$  shows the displacement  $\delta_c$ ).

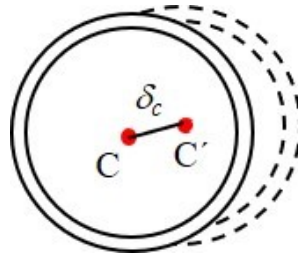


Figure 4.29 Relative displacement of the carrier.

Figure 4.30(a) shows the relative displacements ( $\delta_c$ ) without clearance for a 0% crack level, (b) shows the relative displacements ( $\delta_c$ ) with a carrier bearing clearance for a 0% crack level, (c) shows the relative displacements ( $\delta_c$ ) without clearance for a 50% crack level, and (d) shows the relative displacements ( $\delta_c$ ) with a carrier bearing clearance for a 50% crack level. From this figure, it is obvious (1) the carrier bearing clearance (0.08 mm) is larger than the displacement of the carrier; and (2) the carrier bearing clearance increases the displacement. The average displacement for the carrier increases from  $0.3 \times 10^{-6}$  m to  $0.6 \times 10^{-6}$  m, and the highest displacement with a 50% crack level grows from  $1.23 \times 10^{-6}$  to  $2.8 \times 10^{-6}$ . Finally, (3) the tooth crack creates the impulse in the displacement of the carrier.

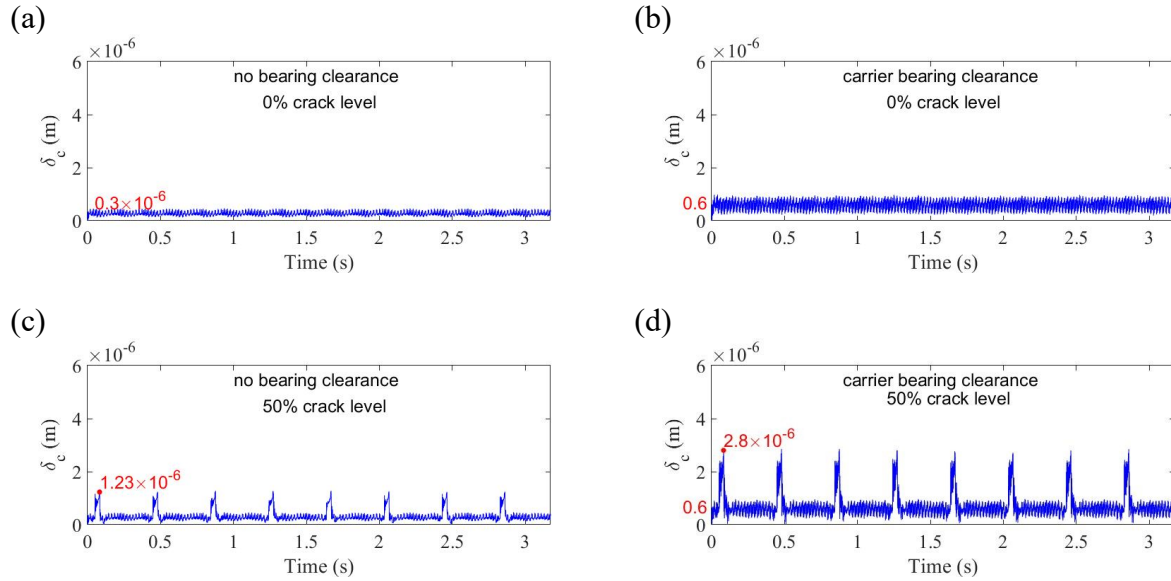


Figure 4.30 Relative displacement of the carrier (a, c) without a bearing clearance for 0% and 50% crack levels and (b, d) with a carrier bearing clearance for 0% and 50% crack levels.

Figure 4.31(a, b) shows the sun-gear displacement in the  $x_g$  and  $y_g$  directions, (c, d) shows the ring-gear displacement in the  $x_g$  and  $y_g$  directions, (e, f) shows the carrier displacement in the  $x_g$  and  $y_g$  directions, and (g, h) shows the total planet-gear displacement in the  $x_g$  and  $y_g$  directions. Furthermore, the red dashed line shows the highest displacement value in the  $x_g$  direction. From the figure, several interesting phenomena are found: (1) the vibration displacement of the planet gear is larger than the displacement of the other components; (2) the vibration displacement of the carrier in this case is larger than the displacement of the carrier in Case 1 without any bearing clearance; and (3) the directions of the carrier and planet-gear displacement are the same. For example, approximately 0.5 s, the vibration directions for the carrier and the planet gear are positive in the  $x_g$  axis.

Furthermore, the simulated vibration response of the planetary gearbox is shown in Figure 4.32, while the red dashed line shows the highest displacement in  $x_{signal}$  with a 50% crack level. The results are as follows: (1) impulse fault signals caused by a tooth crack are easily identified with the increase of a fault crack; and (2) the vibration response of the planetary gearbox is higher than the response in Case 1 without a bearing clearance, even when the crack level is 0%, compared with Figure 4.9(a) and Figure 4.32(a).

The frequency spectrum with a carrier clearance in Figure 4.33 shows the frequencies in the  $x_g$  and  $y_g$  directions are similar. From this figure, we can observe (1) the magnitude of  $f_m$  is increased from  $2.01 \times 10^{-6}$  in Figure 4.33(a) to  $2.27 \times 10^{-6}$  in Figure 4.33(k); and (2) the noise around  $f_m$ ,  $31 f_m$ , and  $33 f_m$  are significantly increased with the growth of the crack level.

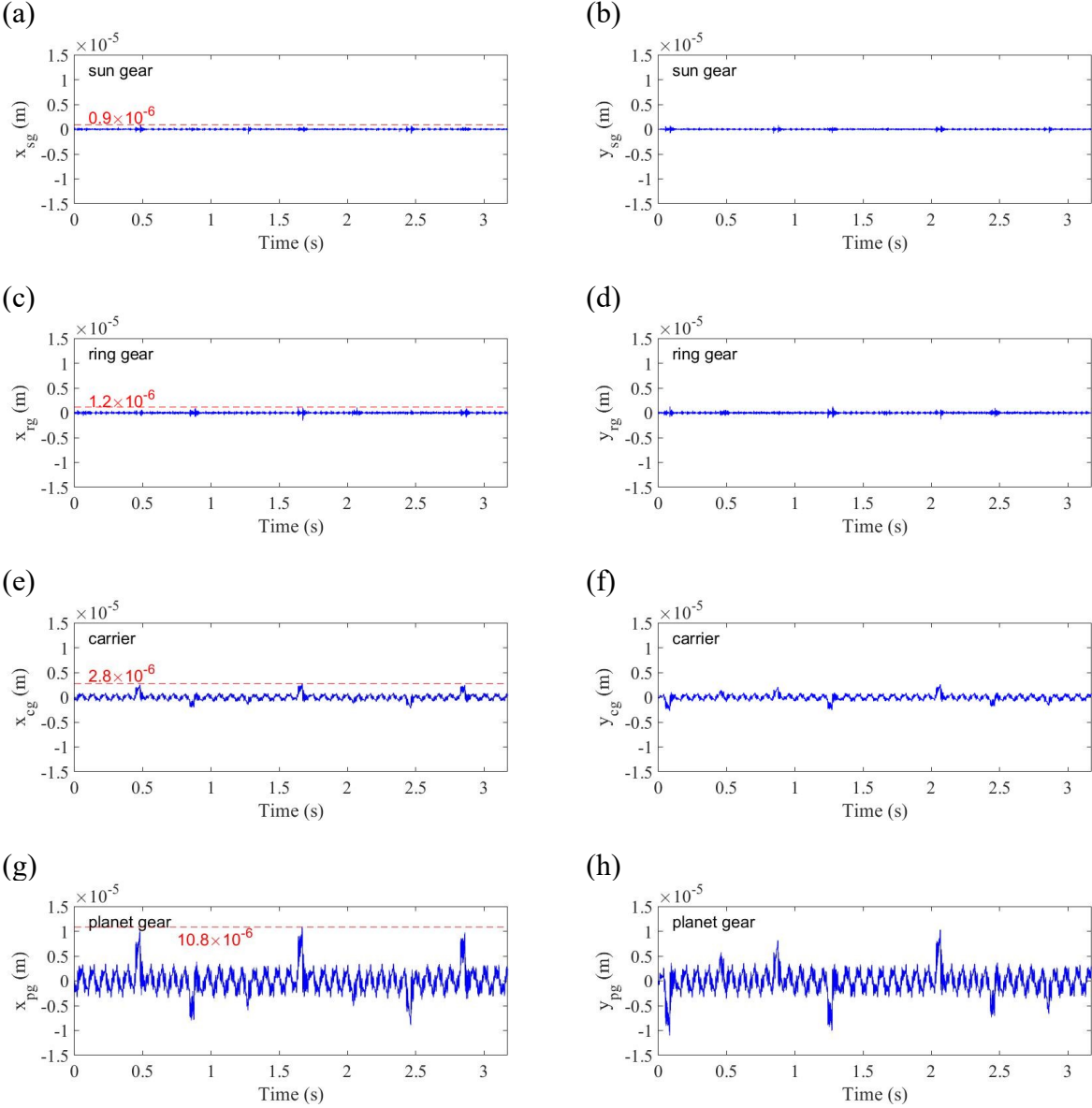


Figure 4.31 Vibration displacement signal of each component with a 50% sun-gear crack with a carrier bearing clearance.

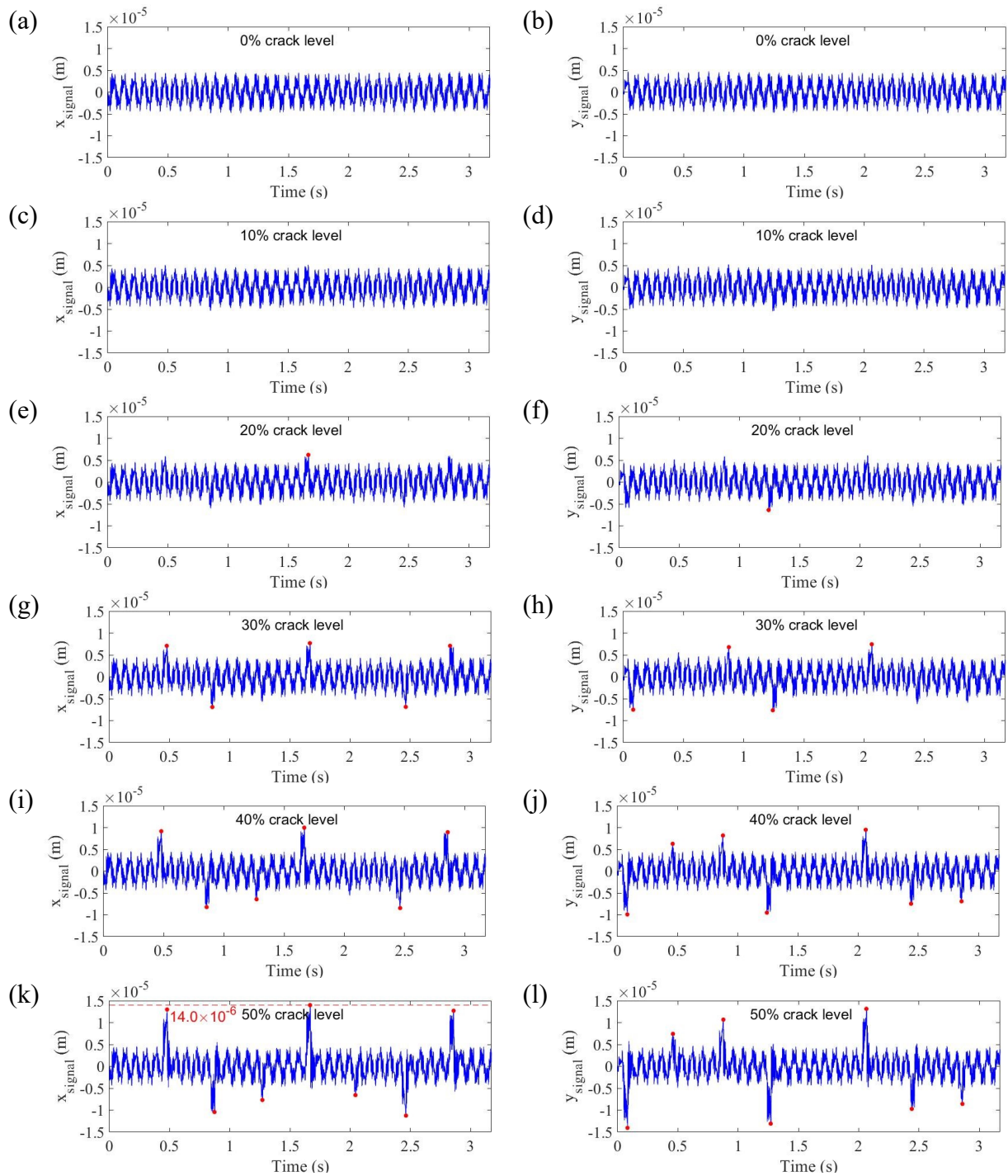


Figure 4.32 Vibration signal of the planetary gearbox in the  $x_g$  direction with (a) 0%, (c) 10%, (e) 20%, (g) 30%, (i) 40%, and (k) 50% sun-gear tooth crack; in the  $y_g$  direction with (b) 0%, (d) 10%, (f) 20%, (h) 30%, (j) 40%, and (l) 50% sun-gear tooth crack considering a carrier bearing clearance.

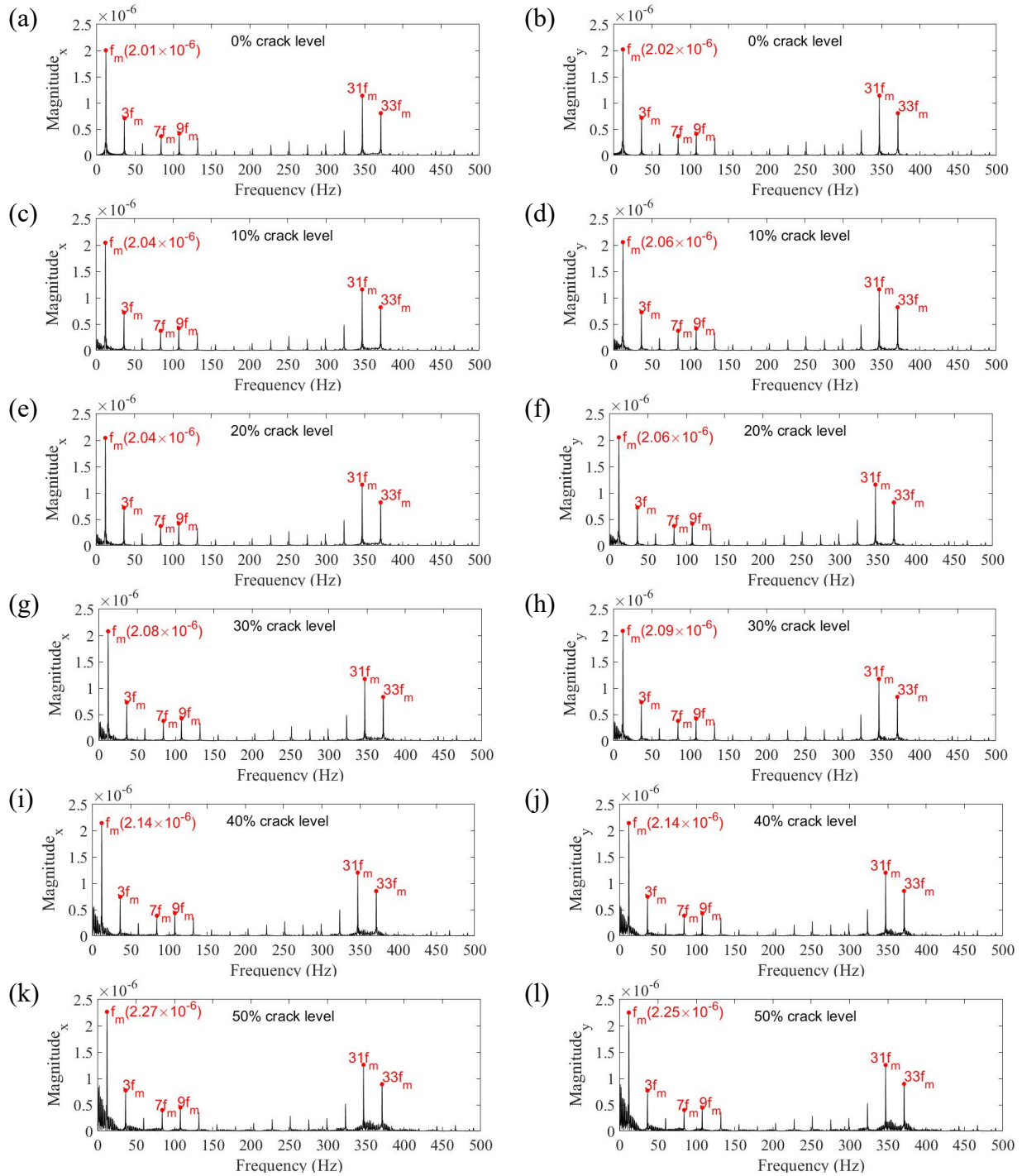


Figure 4.33 Frequency spectrum in the  $x_g$  direction with (a) 0%, (c) 10%, (e) 20%, (g) 30%, (i) 40%, and (k) 50% sun-gear tooth crack; in the  $y_g$  direction with (b) 0%, (d) 10%, (f) 20%, (h) 30%, (j) 40%, and (l) 50% sun-gear tooth crack.

Furthermore, Figure 4.34 illustrates the RMS and kurtosis indices of the vibration signal for the planetary gearbox when the crack level is 0%, 10%, 20%, 30%, 40%, and 50% without a bearing clearance. The line is the RMS and kurtosis in the  $x_g$  direction, while the dashed line is the RMS and kurtosis in the  $y_g$  direction. It is obvious (1) the RMS in the  $x_g$  and  $y_g$  directions is almost the same, and it is increased from  $2.26 \times 10^{-6}$  to  $2.99 \times 10^{-6}$  with the growth of the tooth crack level from 0% to 50% in the  $x_g$  direction; and (2) the kurtosis indices in the  $x_g$  and  $y_g$  directions are almost the same. It is increased from 2.05 to 5.47 in the  $x_g$  direction with the growth of the tooth crack level from 0% to 50%.

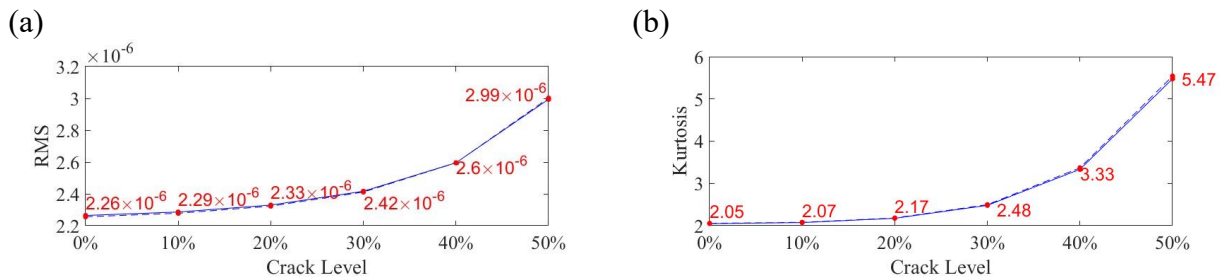


Figure 4.34 (a) RMS and (b) kurtosis of the vibration signal for the planetary gearbox with 0%, 10%, 20%, 30%, 40%, and 50% crack level considering the carrier bearing clearance.

In conclusion, the carrier bearing clearance can increase the highest displacement for the carrier by 1.3 times (from  $1.2 \times 10^{-6}$  m without a bearing clearance to  $2.8 \times 10^{-6}$  m with a carrier bearing clearance), the highest value for the sum displacement of the planet gear by 74% (from  $6.2 \times 10^{-6}$  m to  $10.8 \times 10^{-6}$  m), the highest displacement for the ring gear by 20% (from  $1.0 \times 10^{-6}$  m to  $1.2 \times 10^{-6}$  m), and the highest displacement for the sun gear by 29% (from  $0.7 \times 10^{-6}$  m to  $0.9 \times 10^{-6}$  m), as shown in Figures 4.7 and 4.31. It increases the highest value for the sum of all displacements by 1.2 times (from  $6.3 \times 10^{-6}$  m without a bearing clearance to  $14.0 \times 10^{-6}$  m with a carrier bearing clearance), comparing with Figures 4.9(k) and 4.32(k). Therefore, the carrier bearing clearance can significantly increase the  $f_m$  magnitude from  $1.09 \times 10^{-6}$  to  $2.27 \times 10^{-6}$  with a 50% crack level, compared with Figure 4.13(k) and Figure 4.33(k). Thus, a tooth crack can create noise around  $f_m$ ,  $31 f_m$ , and  $33 f_m$  (Figure 4.33). This means that this clearance factor, which is the carrier bearing clearance, cannot be ignored in future dynamic simulations of gearboxes.

The next section summarizes the effect of each single bearing clearance and compares it with the cases in the RMS and kurtosis indices.

#### 4.3.4. Summary

As mentioned above, in the time domain, (1) the planet-gear bearing clearance does not affect the vibration signal (it only increases the highest value for the sum of all displacements by 1.6%) because the planet-gear bearing clearance (0.035 mm) is lower than the relative displacement between the carrier and the planet gear; (2) the sun-gear bearing clearance significantly increases (by six times) the highest sun-gear displacement and reduces the other components' vibrations; and (3) the carrier bearing clearance increases the highest displacement for the carrier by 1.3 times. In the frequency domain, (1) the planet-gear bearing clearance does not affect the frequency; (2) the sun-gear bearing clearance reduces the magnitude of  $f_m$  from  $1.09 \times 10^{-6}$  to  $0.86 \times 10^{-6}$  with a 50% crack level; and (3) the carrier bearing clearance significantly increases the magnitude of  $f_m$  from  $1.09 \times 10^{-6}$  to  $2.27 \times 10^{-6}$  with a 50% crack level.

Figure 4.35 illustrates the RMS and kurtosis indices of Cases 1 to 4. As mentioned above, the RMS and kurtosis index are similar in the  $x_g$  and  $y_g$  directions, thus Figure 4.35 only analyses the  $x_g$  direction: the red line denotes Case 1 without any bearing clearance; the blue line is for Case 2, which considers the planet-gear bearing clearance (0.035 mm); the green line is for Case 3, which considers the sun-gear bearing clearance; and the black line is for Case 4, which considers the carrier bearing clearance. The results are as follows: (1) the effect of the planet-gear bearing clearance for the RMS index is small; (2) the sun-gear bearing clearance can reduce the RMS index (by approximately 14% with a 50% crack level), compared with 4.14(a) and 4.28(a); (3) the carrier bearing clearance significantly increases the RMS index (by approximately 1.2 times with a 50% crack level), compared with 4.14(a) and 4.34(a); (4) the kurtosis indices for Case 1 without a bearing clearance, Case 2 with a planet-gear bearing clearance, and Case 4 with a carrier bearing clearance are similar; and (5) the sun-gear bearing clearance increases the kurtosis index below the 30% crack level (by approximately 10% with 0% crack level), while it reduces the kurtosis index from the 30% to the 50% crack level (by approximately 16% with 50% crack level), compared with 4.14(b) and 4.28(b).

In conclusion, the sun-gear and carrier bearing clearance can affect the vibration signal of the planetary gearbox mentioned above, while the influence of the planet-gear bearing clearance is too small to be considered.

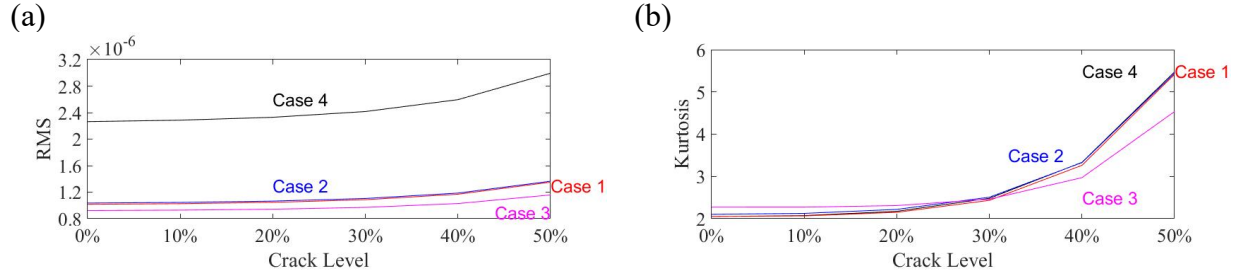


Figure 4.35 (a) RMS and (b) kurtosis of the vibration signal for the planetary gearbox with 0%, 10%, 20%, 30%, 40%, and 50% crack levels for Cases 1, 2, 3, and 4.

#### 4.4. Dynamic Modeling with Two Types of Bearing Clearance

Section 4.3 analyses the effect of a sun-gear crack with a planetary gear model with only one kind of bearing clearance ( $\Delta_c = 0.08$  mm,  $\Delta_s = 0.08$  mm, or  $\Delta_p = 0.035$  mm). In this subsection, with the improved differential equations in Chapter 3, the dynamic response effect with two kinds of bearing clearance will be generated and discussed in the next sections. The Sun-gear and planet-gear bearing clearances are considered in Case 5, the planet-gear and carrier bearing clearances are considered in Case 6, and the sun-gear and carrier bearing clearances are considered in Case 7.

##### 4.4.1. Case 5: Sun-Gear and Planet-Gear Bearing Clearance

In this section, we assume only the carrier bearing has a zero clearance. According to Table 3.3 and Table 3.4, the sun-gear bearing clearance  $\Delta_s$  is 0.08 mm, and the planet-gear bearing clearance  $\Delta_p$  is 0.035 mm (i.e., the minimum values in normal scenarios following the standards of Timken and NTN [70, 71]). As mentioned in Section 4.3, the effect of the planet-gear bearing clearance is very small; thus, the results of Case 5, which consider the sun-gear and planet-gear bearing clearances, are similar to Case 3, which considered the sun-gear bearing clearance.

The simulated vibration response of the planetary gearbox is shown in Figure 4.36, while the red dashed line shows the highest displacement in the  $x_{signal}$  with a 50% crack level. The result is the same as in Figure 4.26 in Case 3 with a sun-gear bearing clearance. The impulse fault signals caused by a tooth crack are easily identified with the increase of a fault crack.

The frequency spectrum with the sun-gear clearance in Figure 4.37 shows the frequencies in the  $x_g$  and  $y_g$  directions are similar to each other. From this figure, we find (1) the magnitude of  $f_m$

is increased from  $0.75 \times 10^{-6}$  in Figure 4.37(a) to  $0.86 \times 10^{-6}$  in Figure 4.37(k); and (2) the noise around  $f_m$  and  $27 f_m$  significantly increases with the growth of the crack level, which is similar to Case 3 that only considered a sun-gear bearing clearance.

Furthermore, Figure 4.38 illustrates the RMS and kurtosis indices of the vibration signal for the planetary gearbox when the crack level is 0%, 10%, 20%, 30%, 40%, and 50% without a bearing clearance. The line is the RMS and kurtosis in the  $x_g$  direction, while the dashed line is the RMS and kurtosis in the  $y_g$  direction. It is obvious (1) the RMS in the  $x_g$  and  $y_g$  directions is almost the same, and it increased from  $0.91 \times 10^{-6}$  to  $1.14 \times 10^{-6}$  with the growth of the tooth crack level from 0% to 50% in the  $x_g$  direction; and (2) the kurtosis indices in the  $x_g$  and  $y_g$  directions are almost the same below the 30% crack level. The index is increased from 2.26 to 4.61 in the  $x_g$  direction and from 2.26 to 4.77 in the  $y_g$  direction with the growth of the tooth crack level from 0% to 50%.

In conclusion, the sun-gear and planet-gear bearing clearances reduce the sum of all displacements of all gearbox components by about 17% at the most (from  $6.3 \times 10^{-6}$  to  $5.2 \times 10^{-6}$ ), compared with Figures 4.9(k) and 4.36(k). These two clearances can reduce the magnitude of  $f_m$  (decrease by 21% with a 50% crack level), as in Case 3, while increasing the magnitude of  $27 f_m$  (Figure 4.37) by 5.7 times, as in Case 3. The tooth crack can create noise around  $f_m$  and  $27 f_m$  (Figure 4.37). These results are similar to those of Case 3, in which only the sun-gear bearing clearance was considered. This means the planet-gear bearing clearance can be ignored, but the sun-gear bearing clearance cannot be ignored, in future dynamic simulations of gearboxes, because the effect of the planet-gear bearing clearance is very small (approximately 1.6% in sum of all displacements) compared to the effect of the sun-gear bearing clearance (approximately 16% in sum of all displacements).

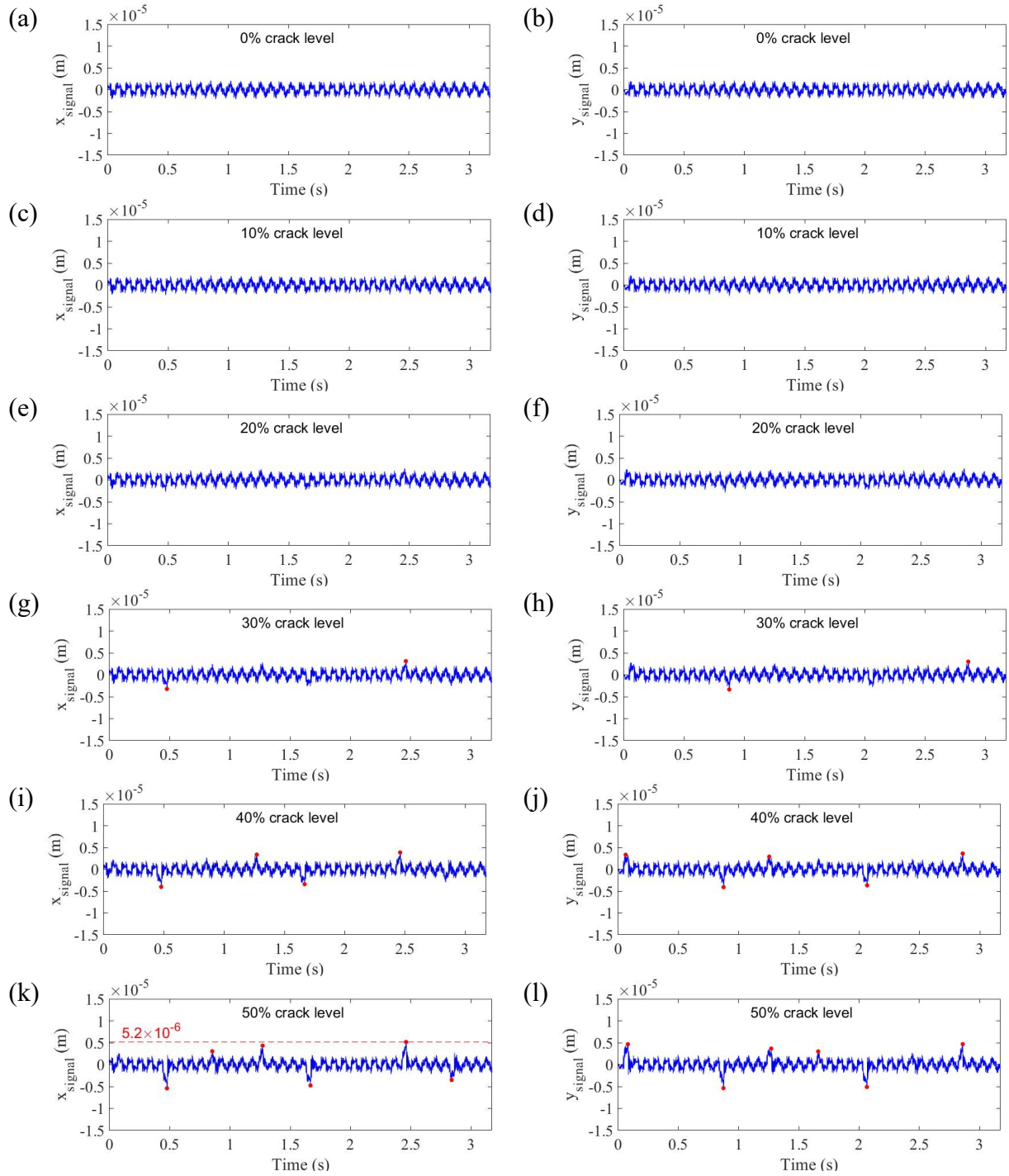


Figure 4.36 Vibration signal of the planetary gearbox in the  $x_g$  direction with (a) 0%, (c) 10%, (e) 20%, (g) 30%, (i) 40%, and (k) 50% sun-gear tooth crack; in the  $y_g$  direction with (b) 0%, (d) 10%, (f) 20%, (h) 30%, (j) 40%, and (l) 50% sun-gear tooth crack considering the sun-gear and planet-gear bearing clearances.

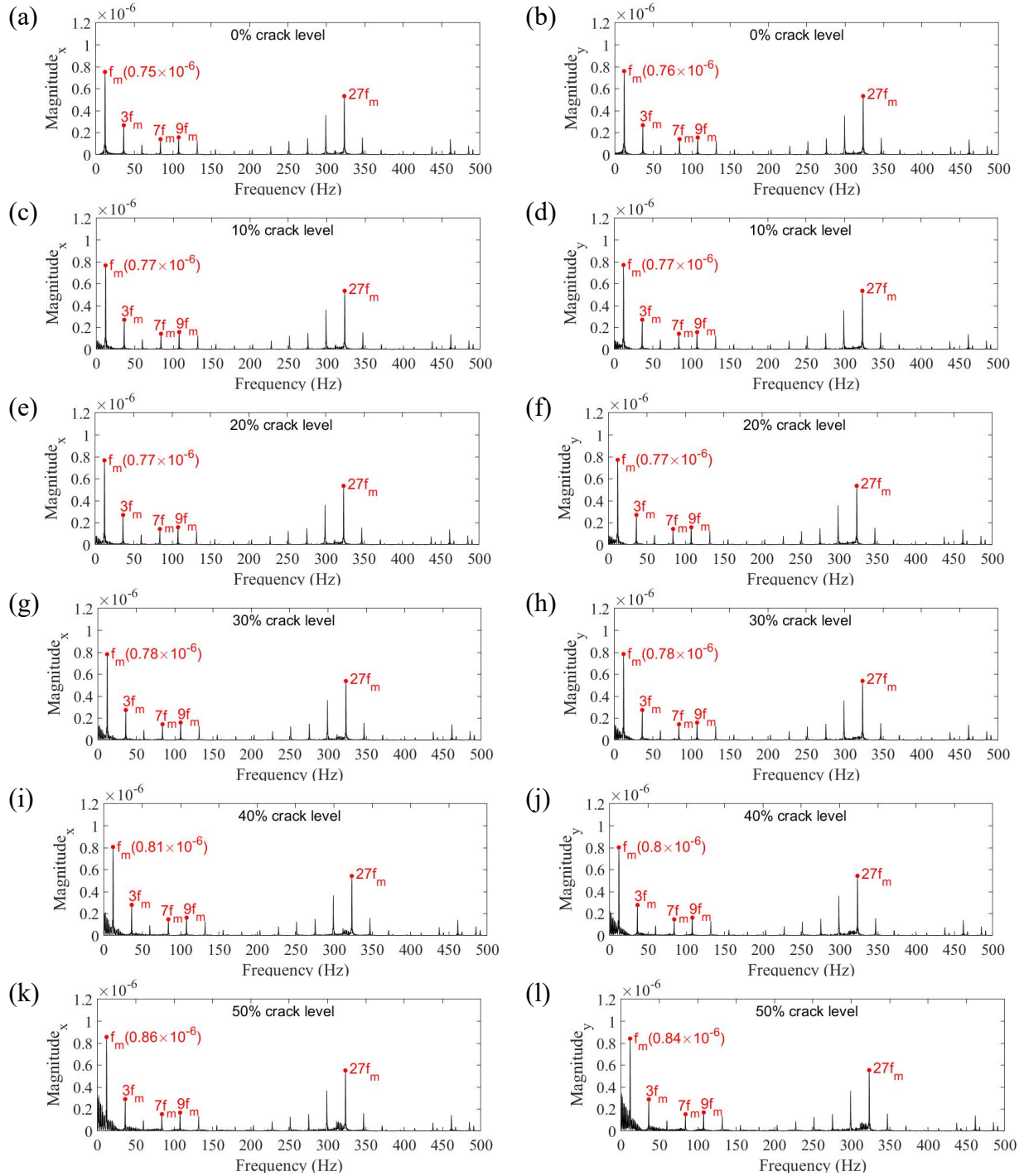


Figure 4.37 Frequency spectrum in the  $x_g$  direction with (a) 0%, (c) 10%, (e) 20%, (g) 30%, (i) 40%, and (k) 50% sun-gear tooth crack; in the  $y_g$  direction with (b) 0%, (d) 10%, (f) 20%, (h) 30%, (j) 40%, and (l) 50% sun-gear tooth crack.

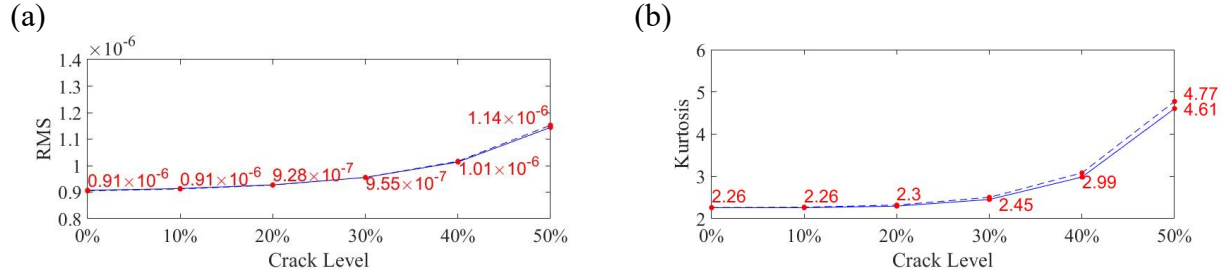


Figure 4.38 (a) RMS and (b) kurtosis of the vibration signal for the planetary gearbox with 0%, 10%, 20%, 30%, 40%, and 50% crack level considering the sun-gear and planet-gear bearing clearances

#### 4.4.2. Case 6: Planet-Gear and Carrier Bearing Clearance

In this section, we assume that only the sun-gear bearing has zero clearance. According to Table 3.3 and Table 3.4, the bearing clearance  $\Delta_c$  of the carrier is determined to be 0.08 mm, and the bearing clearance  $\Delta_p$  of the planet gear is determined to be 0.035 mm, (i.e. the minimum values in normal scenarios following the standards of Timken and NTN [70, 71].) As mentioned in Section 4.3, the effect of the planet-gear bearing clearance is small; thus, the results of Case 6, which consider the planet-gear and carrier bearing clearances, are similar to those of Case 4, which consider the carrier bearing clearance.

The simulation of the vibration response of the planetary gearbox is shown in Figure 4.39, where the red dashed line shows the highest displacement in the  $x_{signal}$  with a 50% crack level. The result is the same as in Figure 4.32 for Case 4 with a sun-gear bearing clearance. The impulse fault signals caused by a tooth crack are easily identified with the increase of a fault crack.

The frequency spectrum with a sun-gear clearance in Figure 4.40 shows the frequencies in the  $x_g$  and  $y_g$  directions are similar to each other. From this figure, we find (1) the magnitude of  $f_m$  is increased from  $2.01 \times 10^{-6}$  in Figure 4.40(a) to  $2.27 \times 10^{-6}$  in Figure 4.40(k); (2) the noise around  $f_m$ ,  $31 f_m$ , and  $33 f_m$  significantly increased with the increase in the crack level, similar to Case 4 in which only the carrier bearing clearance was considered.

Furthermore, Figure 4.41 illustrates the RMS and kurtosis indices of the vibration signal for the planetary gearbox when the crack level is 0%, 10%, 20%, 30%, 40%, and 50% without a bearing clearance. The solid line shows the RMS and kurtosis in the  $x_g$  direction, and the dashed line shows the RMS and kurtosis in the  $y_g$  direction. It is clear (1) the RMS values in the  $x_g$  and  $y_g$  directions

are almost the same, and it increased from  $2.28 \times 10^{-6}$  to  $3.02 \times 10^{-6}$  with the increase in the tooth crack level from 0% to 50% in the  $x_g$  direction; (2) the kurtosis indices in the  $x_g$  and  $y_g$  directions are almost the same. It increased from 2.05 to 5.44 in the  $x_g$  direction with the increase in the tooth crack level from 0% to 50%.

In conclusion, the planet-gear bearing clearance does not affect the vibration response, even when considering the carrier and planet-gear bearing clearances. The reason may be that the planet-gear bearing clearance is much smaller than the displacement of the planet gear, which is discussed in Case 2. The planet-gear and carrier bearing clearances can increase the highest value for the sum of all displacements by 1.3 times (from  $6.3 \times 10^{-6}$  to  $14.3 \times 10^{-6}$ ), compared with Figures 4.9(k) and 4.39(k). These two clearances can significantly increase the magnitude for  $f_m$  by 1.1 times (from  $1.09 \times 10^{-6}$  to  $2.27 \times 10^{-6}$  with a 50% crack level), compared with Case 1 in Figure 4.13(k) and this case in Figure 4.40(k). Then, the tooth crack can create noise around  $f_m$ ,  $31 f_m$ , and  $33 f_m$  (Figure 4.40). These results are similar to those of Case 4, in which only the sun-gear bearing clearance was considered. This means that the planet-gear bearing clearance can be ignored, but the carrier bearing clearance must be considered, in future dynamic simulations of gearboxes, because the effect of the planet-gear bearing clearance is very small (approximately 1.6% in sum of all displacements) in comparison to the effect of the carrier bearing clearance (approximately 120% in sum of all displacements).

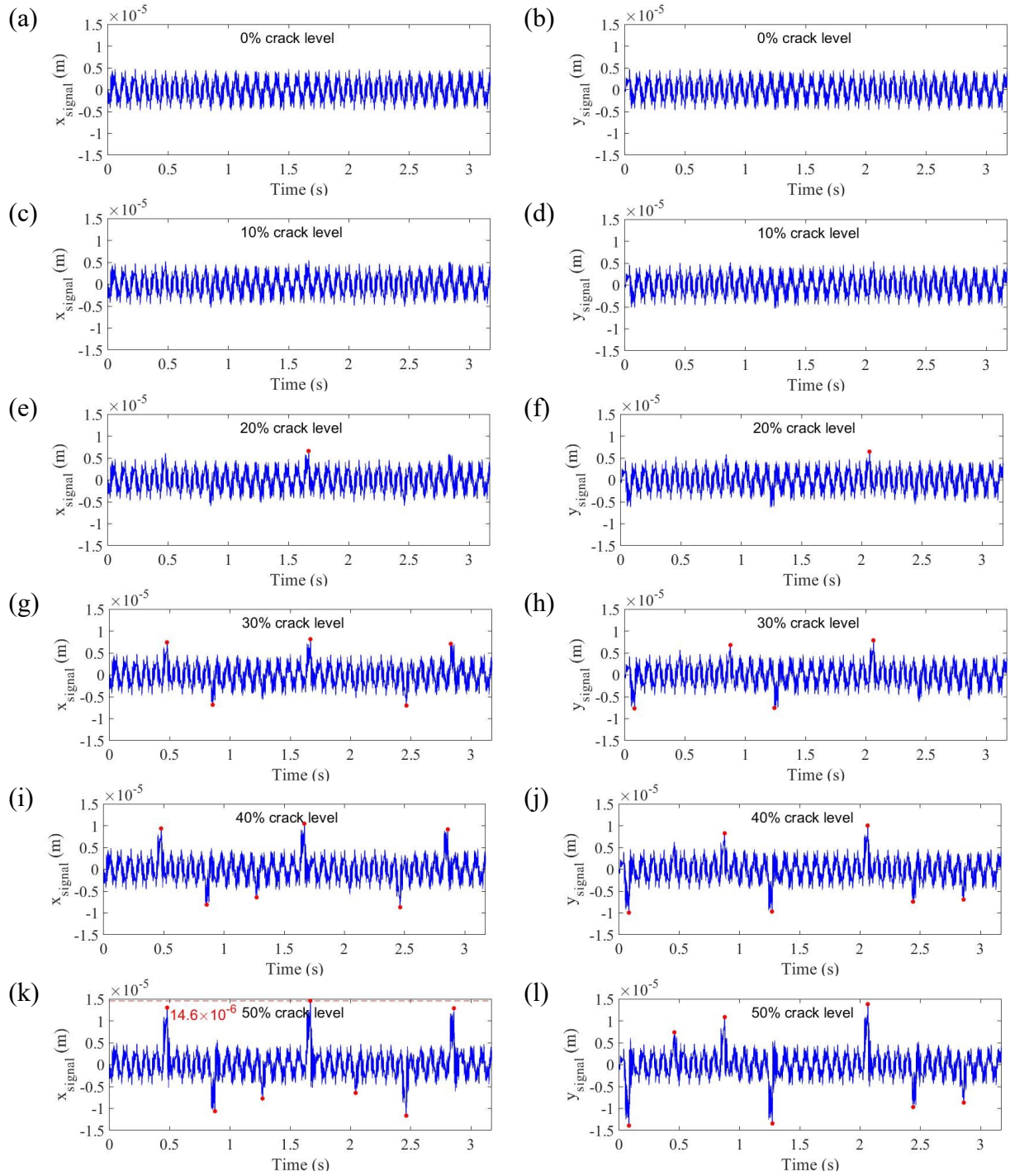


Figure 4.39 Vibration signal of the planetary gearbox in the  $x_g$  direction with (a) 0%, (c) 10%, (e) 20%, (g) 30%, (i) 40%, and (k) 50% sun-gear tooth crack; in the  $y_g$  direction with (b) 0%, (d) 10%, (f) 20%, (h) 30%, (j) 40%, and (l) 50% sun-gear tooth crack considering planet-gear and carrier bearing clearances.

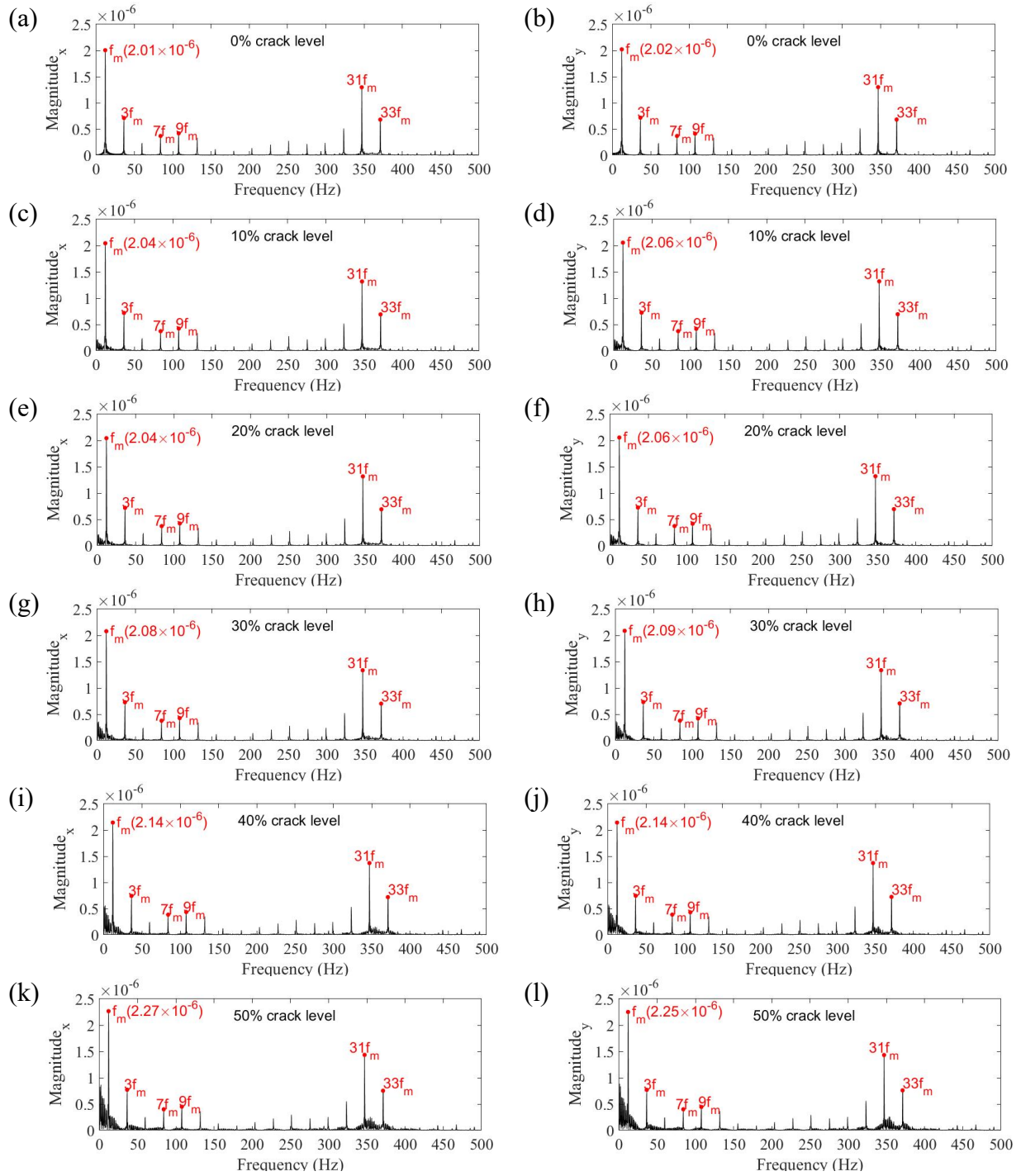


Figure 4.40 Frequency spectrum in the  $x_g$  direction with (a) 0%, (c) 10%, (e) 20%, (g) 30%, (i) 40%, and (k) 50% sun-gear tooth crack; in the  $y_g$  direction with (b) 0%, (d) 10%, (f) 20%, (h) 30%, (j) 40%, and (l) 50% sun-gear tooth crack.

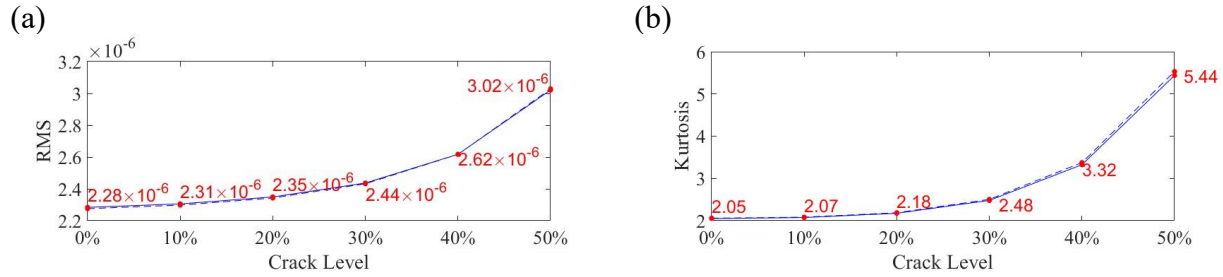


Figure 4.41 (a) RMS and (b) kurtosis of the vibration signal for the planetary gearbox with 0%, 10%, 20%, 30%, 40%, and 50% crack level considering the carrier and planet-gear bearing clearances.

#### 4.4.3. Case 7: Sun-Gear and Carrier Bearing Clearance

In this section, we assume only the planet-gear bearing has a zero clearance. According to Table 3.3 and Table 3.4, the bearing clearance  $\Delta_c$  of the carrier is determined to be 0.08 mm, and the bearing clearance  $\Delta_s$  of the sun gear is determined to be 0.08 mm, (i.e. the minimum values in normal scenarios following the standards of Timken and NTN).

Figure 4.42 (a, b) shows the displacement of the sun gear in the  $x_g$  and  $y_g$  directions, (c, d) shows the displacement of the ring gear in the  $x_g$  and  $y_g$  directions, (e, f) shows the displacement of the carrier in the  $x_g$  and  $y_g$  directions, and (g, h) shows the displacement of the total planet gear in the  $x_g$  and  $y_g$  directions. The red dashed line shows the highest displacement value in the  $x_g$  direction. From the figure, several interesting phenomena are found: (1) the displacement of the sun gear is higher than the other component vibrations; and (2) the displacement directions of the sun gear and planet gear are opposite. For example, approximately 0.5 s, the direction for the sun gear is negative, whereas it is positive for the planet gear in the  $x_g$  direction. This opposite direction can reduce the vibration response of the planetary gearbox, as shown in Figure 4.43, because of the transmission path limitation based on Eqs. (3.34) and (3.35).

The simulation of the vibration response of the planetary gearbox is shown in Figure 4.43, where the red dashed line shows the highest displacement in the  $x_{signal}$  with a 50% crack level. From the figure, several interesting phenomena are found: (1) the vibration displacement of the sun gear is larger than the displacements of the other components; (2) compared with other cases, the vibration response is reduced because of the transmission path limitation equations mentioned

above; and (3) from 0 to 3 s, eight different impulse cases by tooth crack can be found in Figure 4.43(k, l).

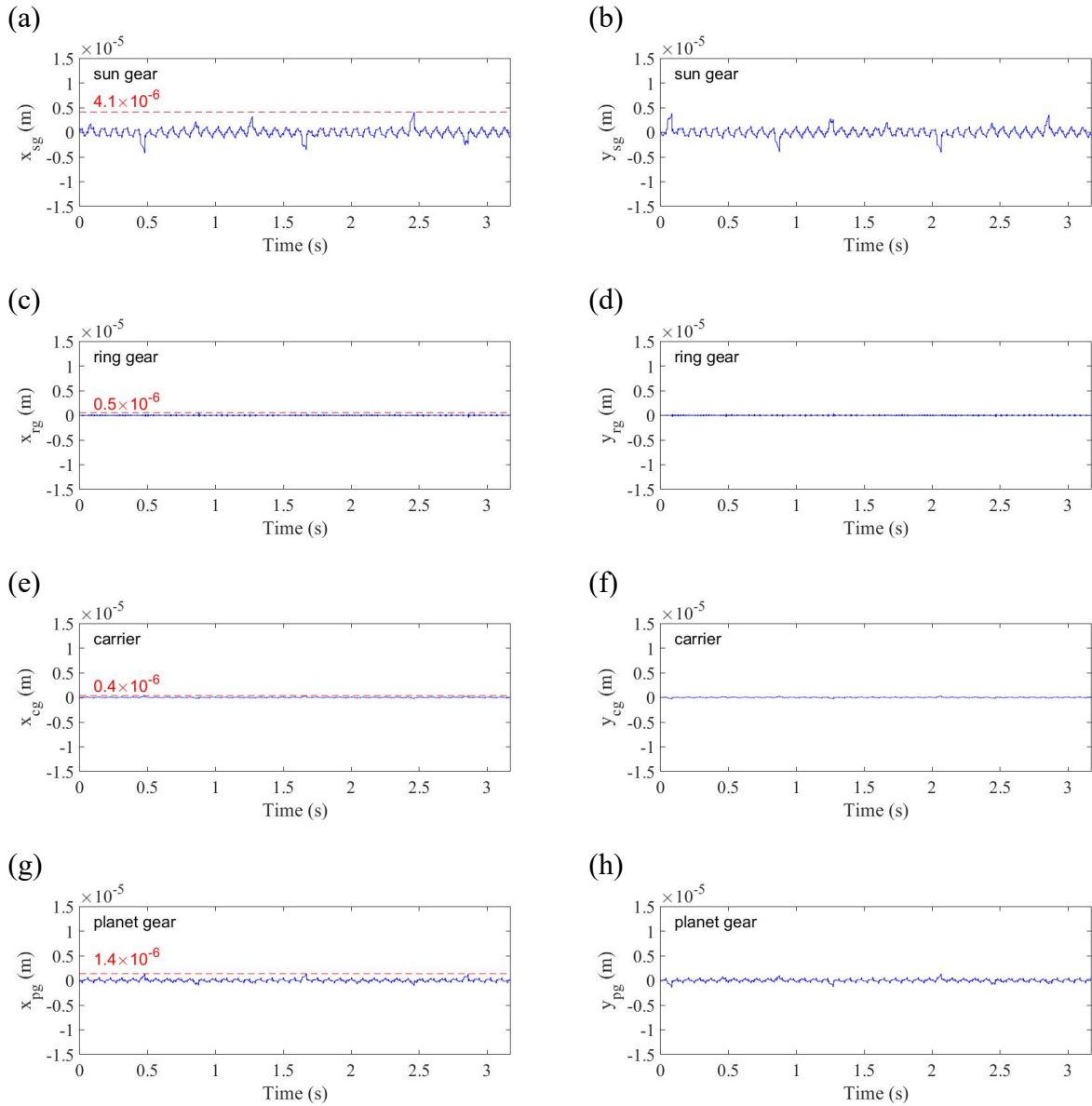


Figure 4.42 Vibration displacement signal of each component with a 50% sun-gear crack with the carrier and sun-gear bearing clearances.

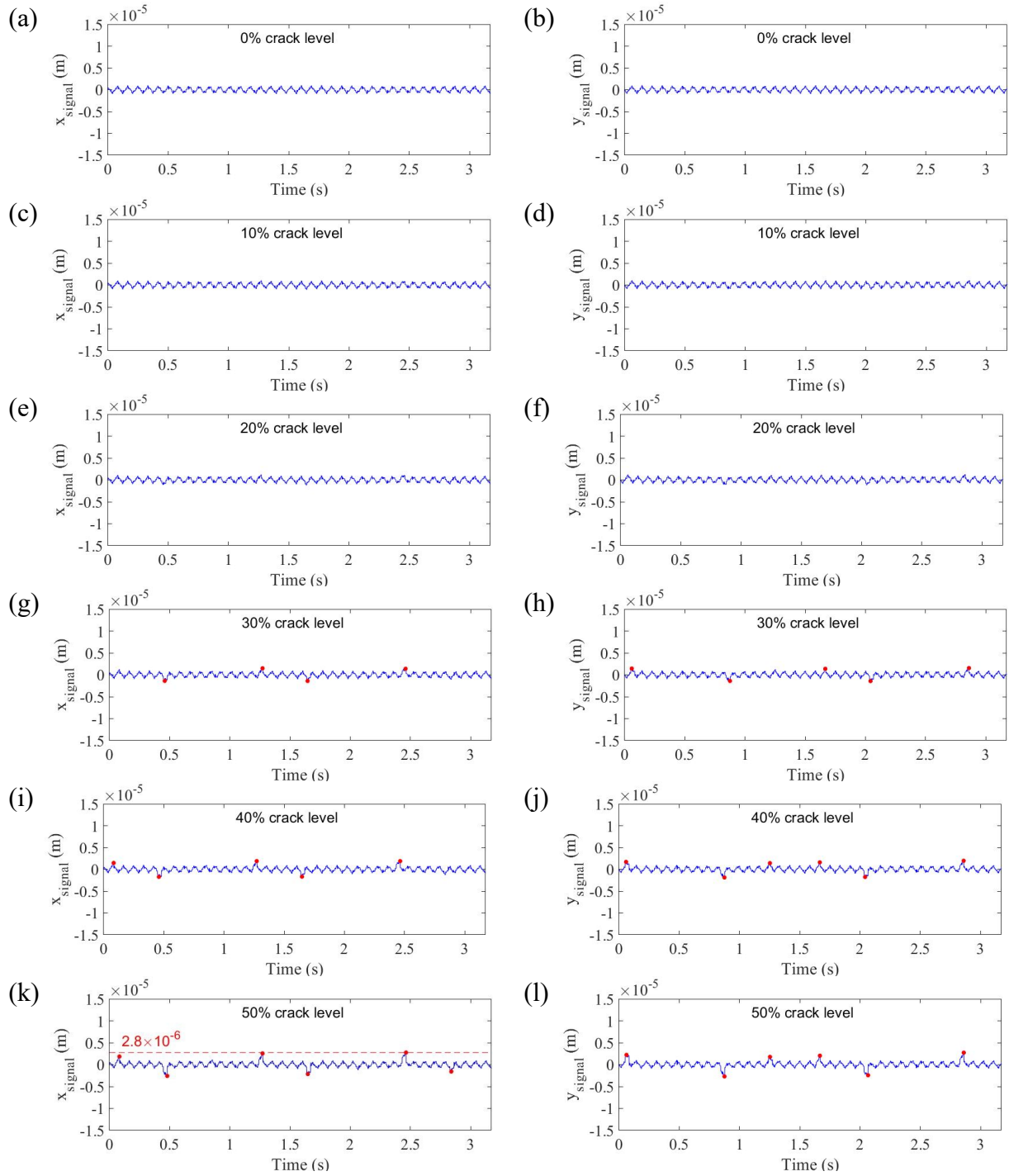


Figure 4.43 Vibration signal of the planetary gearbox in the  $x_g$  direction with (a) 0%, (c) 10%, (e) 20%, (g) 30%, (i) 40%, and (k) 50% sun-gear tooth crack; in the  $y_g$  direction with (b) 0%, (d) 10%, (f) 20%, (h) 30%, (j) 40%, and (l) 50% sun-gear tooth crack considering the sun-gear and carrier bearing clearances.

Figure 4.44 shows the frequencies in the  $x_g$  and  $y_g$  directions are similar to each other. From this figure, we find (1) the magnitude of  $f_m$  is increased from  $0.49 \times 10^{-6}$  in Figure 4.44 (a) to  $0.55 \times 10^{-6}$  in Figure 4.44(k); and (2) the noise around  $f_m$ .

Furthermore, Figure 4.45 illustrates the RMS and kurtosis indices of the vibration signal for the planetary gearbox when the crack level is 0%, 10%, 20%, 30%, 40%, and 50% without a bearing clearance. The solid line shows the RMS and kurtosis in the  $x_g$  direction, while the dashed line shows the RMS and kurtosis in the  $y_g$  direction. It is clear (1) the RMS values in the  $x_g$  and  $y_g$  directions are almost the same below a 30% crack level, and it increased from  $4.5 \times 10^{-7}$  to  $6.09 \times 10^{-7}$  in the  $x_g$  direction, and from  $4.5 \times 10^{-7}$  to  $6.18 \times 10^{-7}$  in the  $y_g$  direction, with the increase in the tooth crack level from 0% to 50%; (2) the kurtosis indices in the  $x_g$  and  $y_g$  directions are almost the same below a 30% crack level. It increased from 2.06 to 6.01 in the  $x_g$  direction and from 2.06 to 6.14 in the  $y_g$  direction, with the increase in the tooth crack level from 0% to 50%.

In conclusion, the sun-gear and carrier bearing clearances increase the highest displacement for the sun gear by 4.9 times (from  $0.7 \times 10^{-6}$  m without any bearing clearance to  $4.1 \times 10^{-6}$  m with the carrier and sun-gear bearing clearances), whereas they reduce the highest displacement for the ring gear by 50% (from  $1 \times 10^{-6}$  m to  $0.5 \times 10^{-6}$  m), the highest displacement for the carrier by 67% (from  $1.2 \times 10^{-6}$  m to  $0.4 \times 10^{-6}$  m), and the highest value for the sum displacement of the planet gears by 77% (from  $6.2 \times 10^{-6}$  m to  $1.4 \times 10^{-6}$  m), as shown in Figures 4.7 and 4.42. They significantly reduce the sum of all displacements of all gearbox components by about 56% compared with Figures 4.9(k) and 4.43(k) (from  $6.3 \times 10^{-6}$  m to  $2.8 \times 10^{-6}$  m). The sun-gear bearing clearance can reduce the magnitude of  $f_m$  by about 50% with a 50% crack level, from  $1.09 \times 10^{-6}$  to  $0.55 \times 10^{-6}$ . This means that these clearance factors, the sun-gear and carrier bearing clearances, cannot be ignored in future dynamic simulations of gearboxes, because their influence has been found to be considerable in this section. The effect of the carrier and sun-gear bearing clearances is around 50% in the sum of all displacements.

The next section summarizes the effect of considering two kinds of bearing clearance. The following section only compares Cases 5, 6, and 7 with Case 1, in terms of RMS and kurtosis index, because Case 2 is similar to Case 1, Case 3 is similar to Case 5, and Case 4 is similar to Case 6.

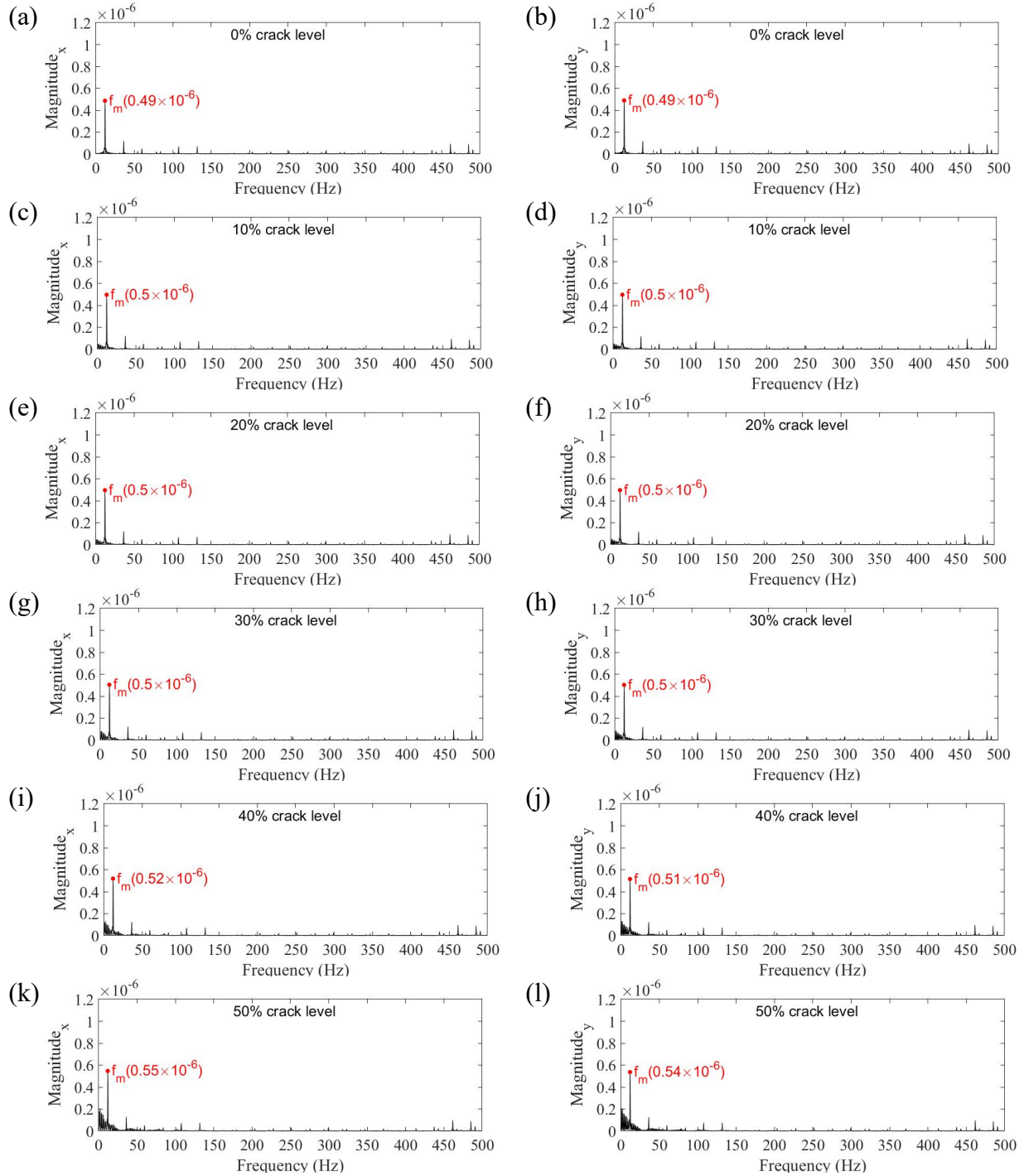


Figure 4.44 Frequency spectrum in the  $x_g$  direction with (a) 0%, (c) 10%, (e) 20%, (g) 30%, (i) 40%, and (k) 50% sun-gear tooth crack; in the  $y_g$  direction with (b) 0%, (d) 10%, (f) 20%, (h) 30%, (j) 40%, and (l) 50% sun-gear tooth crack.

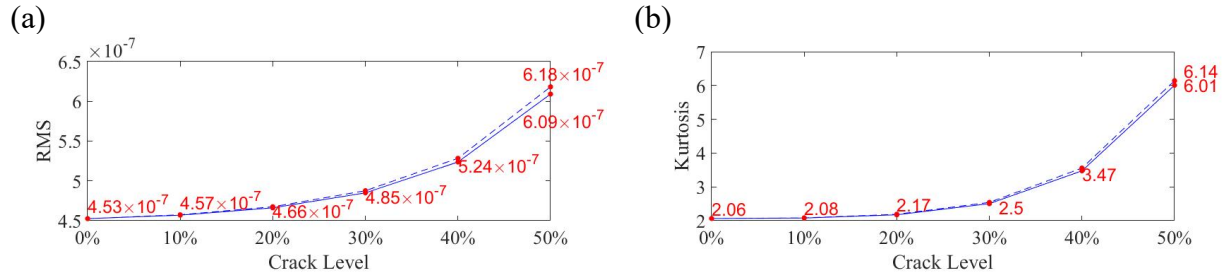


Figure 4.45 (a) RMS and (b) kurtosis of the vibration signal for the planetary gearbox with 0%, 10%, 20%, 30%, 40%, and 50% crack level considering the carrier and sun-gear bearing clearances.

#### 4.4.4. Summary

As mentioned above, in the time domain, (1) the planet-gear bearing clearance does not affect the vibration signal, even considering two kinds of bearing clearance; (2) although the sun-gear or the carrier bearing clearance can increase the vibration response (by around 17% and 120% for the highest value in the sum of all displacements), considering the sun-gear and carrier will reduce the vibration displacement of the planetary gearbox (by around 50% for the highest value in the sum of all displacements). In the frequency domain, (1) the planet-gear bearing clearance does not affect the frequency; and (2) considering the sun-gear bearing clearance and the carrier bearing clearance reduce the magnitude of  $f_m$  from  $0.96 \times 10^{-6}$  to  $0.48 \times 10^{-6}$  with a 0% crack level.

Figure 4.46 illustrates the RMS and kurtosis index of Case 1, Case 5, Case 6, and Case 7. As mentioned above, the RMS and kurtosis index are similar in the  $x_g$  and  $y_g$  directions, and thus Figure 4.46 only analyses the  $x_g$  direction. The red line denotes Case 1 without any bearing clearance, the blue line is for Case 5 considering the sun-gear and planet-gear bearing clearances, the green line is for Case 6 considering the planet-gear and carrier bearing clearances, and the black line is for Case 7 considering the carrier and sun-gear bearing clearances. The results are as follows: (1) the effect of Case 5 with the sun-gear and planet-gear bearing clearances for the RMS index is small (from  $1.35 \times 10^{-6}$  to  $1.14 \times 10^{-6}$  with a 50% crack level); (2) the sun-gear and carrier bearing clearances (Case 7) can reduce the RMS index (by around 54% with a 50% crack level), compared with Figure 4.14(a) and Figure 4.45(a); (3) the carrier and planet-gear bearing clearances (Case 6) significantly increase the RMS index by around 1.2 times, compared with Figure 4.14(a) and Figure 4.41(a); (4) the kurtosis indices for Case 1 without a bearing clearance and Case 6 with the planet-gear and carrier bearing clearances are almost same; (5) the sun-gear and planet-gear

(Case 5) bearing clearances increase the kurtosis index below a 30% crack level (by around 10% with a 0% crack level), whereas they reduce the kurtosis index from a 30% to 50% crack level (by around 15% with a 50% crack level), compared with Figure 4.14(b) and Figure 4.38(b); and (6) considering the sun-gear and carrier bearing clearances (Case 7) can increase the kurtosis index from a 30% to 50% crack level (by around 11% with a 50% crack level), compared with Figure 4.14(b) and Figure 4.45(b).

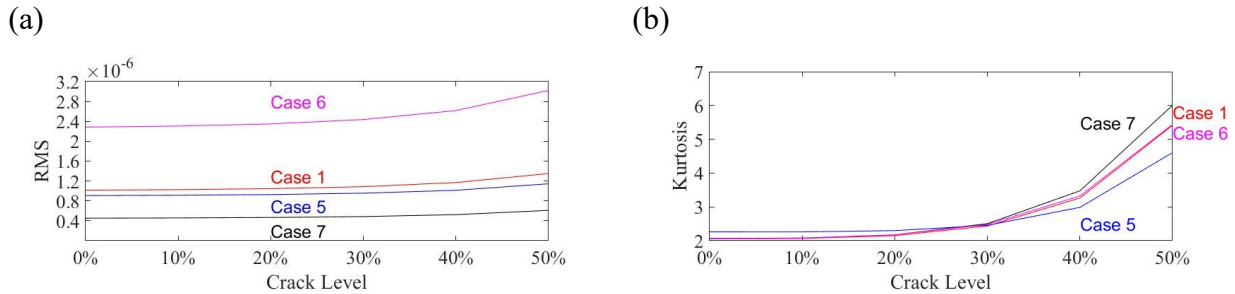


Figure 4.46 (a) RMS and (b) kurtosis of the vibration signal for the planetary gearbox with 0%, 10%, 20%, 30%, 40%, and 50% crack level for Cases 1, 5, 6, and 7.

In conclusion, the planet-gear bearing clearance can be ignored, even if other bearing clearances are considered, because its influence was found to be very small in this section. Therefore, it is important to consider the sun-gear and carrier bearing clearances in future dynamic simulations of gearboxes because these two clearances can affect the vibration signal of the planetary gearbox mentioned above.

## 4.5. Dynamic Modeling with Three Types of Bearing Clearance

In this section, we consider the scenario wherein all three types of bearing clearances take non-zero values. This is referred to as Case 8.

### 4.5.1. Case 8: Sun-Gear, Planet-Gear, and Carrier Bearing Clearances

In this section, we assume there is no zero clearance. According to Table 3.3 and Table 3.4, the bearing clearance  $\Delta_s$  of the sun gear is determined to be 0.08 mm, the bearing clearance  $\Delta_c$  of the carrier is determined to be 0.08 mm, and the bearing clearance  $\Delta_p$  of the planet gear is determined to be 0.035 mm, that is, the minimum values in normal scenarios following the standards of Timken and NTN. As mentioned in Section 4.3, the effect of the planet-gear bearing clearance is small; thus, the results of Case 8 considering all bearing clearances are similar to those of Case 7

considering the carrier and sun-gear bearing clearances. The simulation of the vibration response of the planetary gearbox is shown in Figure 4.47, where the red dashed line shows the highest displacement in the  $x_{signal}$  with a 50% crack level. The result is similar to what is shown in Figure 4.43 in Case 7 with the carrier and sun-gear bearing clearances. The impulse fault signals caused by the tooth crack are easily identified with the increase in the fault crack.

The frequency spectrum with the carrier, sun-gear, and planet-gear bearing clearances in Figure 4.48 shows the frequencies in the  $x_g$  and  $y_g$  directions are similar to each other. From this figure, we find (1) the magnitude of  $f_m$  is increased from  $0.49 \times 10^{-6}$  in Figure 4.48(a) to  $0.55 \times 10^{-6}$  in Figure 4.48(k); and (2) the noise around  $f_m$  is similar to Case 7, which considered the carrier and sun-gear bearing clearances.

Figure 4.49 illustrates the RMS and kurtosis index of the vibration signal for the planetary gearbox when the crack level is 0%, 10%, 20%, 30%, 40%, and 50% without a bearing clearance. The solid line shows the RMS and kurtosis in the  $x_g$  direction, and the dashed line shows the RMS and kurtosis in the  $y_g$  direction. It is clear (1) the RMS values in the  $x_g$  and  $y_g$  directions are almost the same under a 30% crack level, and it increased from  $4.53 \times 10^{-7}$  to  $6.1 \times 10^{-7}$  in the  $x_g$  direction, and from  $4.53 \times 10^{-7}$  to  $6.18 \times 10^{-7}$  in the  $y_g$  direction, with the increase in the tooth crack level from 0% to 50%; and (2) the kurtosis indices in the  $x_g$  and  $y_g$  directions are almost the same below a 30% crack level. It increased from 2.06 to 5.97 in the  $x_g$  direction, and from 2.06 to 6.1 in the  $y_g$  direction, with the increase in the tooth crack level from 0% to 50%.

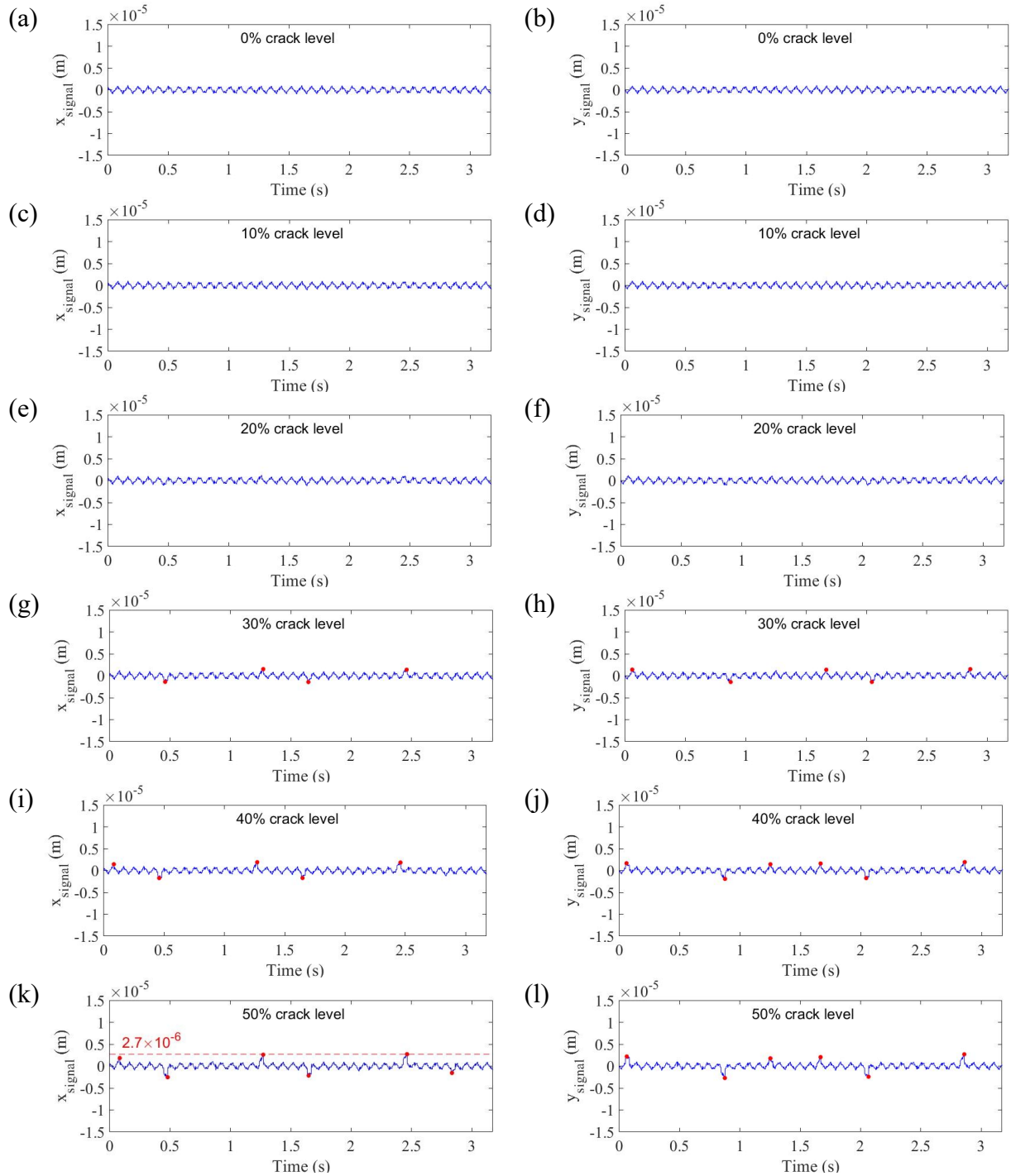


Figure 4.47 Vibration signal of the planetary gearbox in the  $x_g$  direction with (a) 0%, (c) 10%, (e) 20%, (g) 30%, (i) 40%, and (k) 50% sun-gear tooth crack; in the  $y_g$  direction with (b) 0%, (d) 10%, (f) 20%, (h) 30%, (j) 40%, and (l) 50% sun-gear tooth crack considering the carrier, sun-gear, and planet-gear bearing clearances.

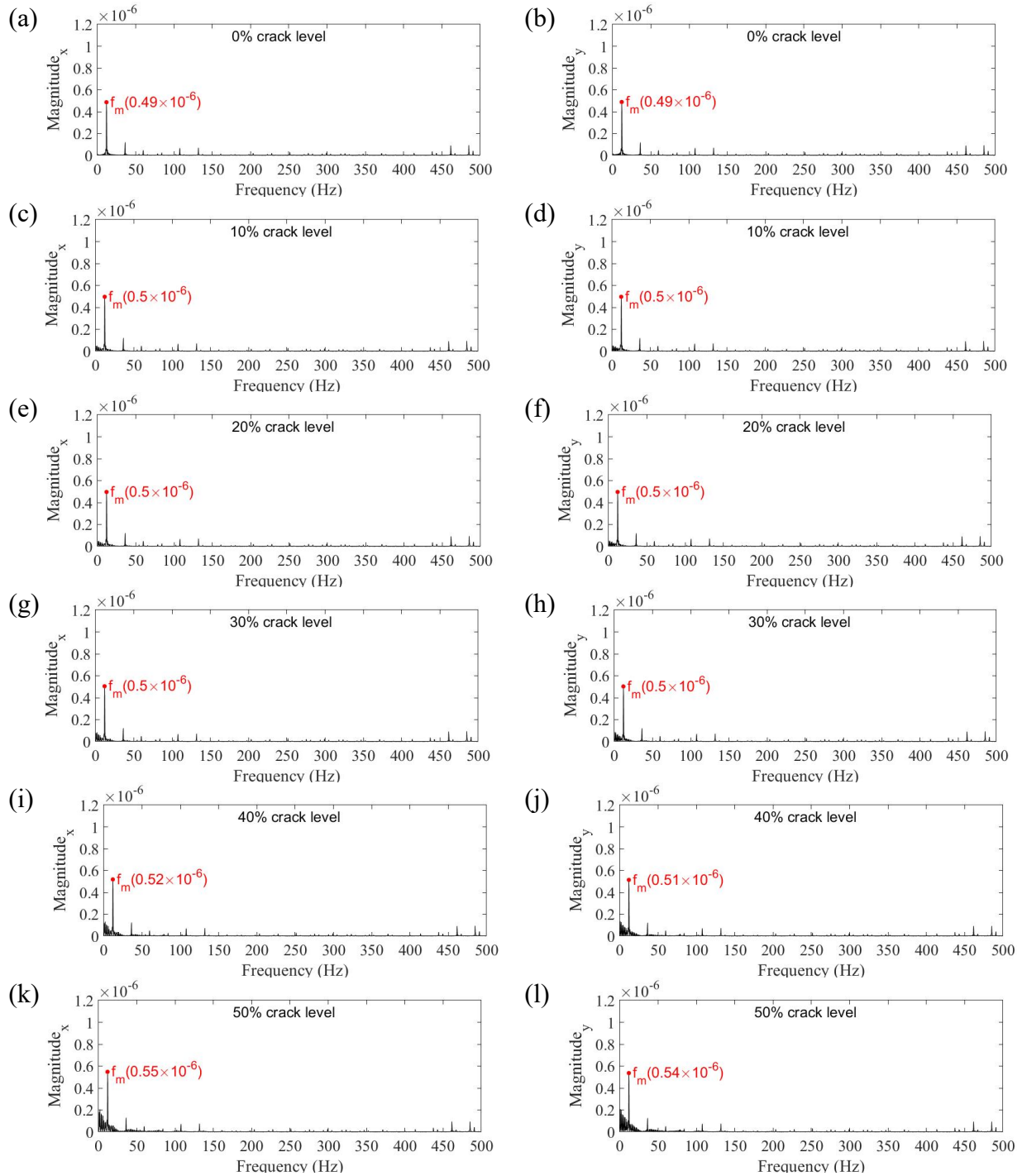


Figure 4.48 Frequency spectrum in the  $x_g$  direction with (a) 0%, (c) 10%, (e) 20%, (g) 30%, (i) 40%, and (k) 50% sun-gear tooth crack; in the  $y_g$  direction with (b) 0%, (d) 10%, (f) 20%, (h) 30%, (j) 40%, and (l) 50% sun-gear tooth crack.

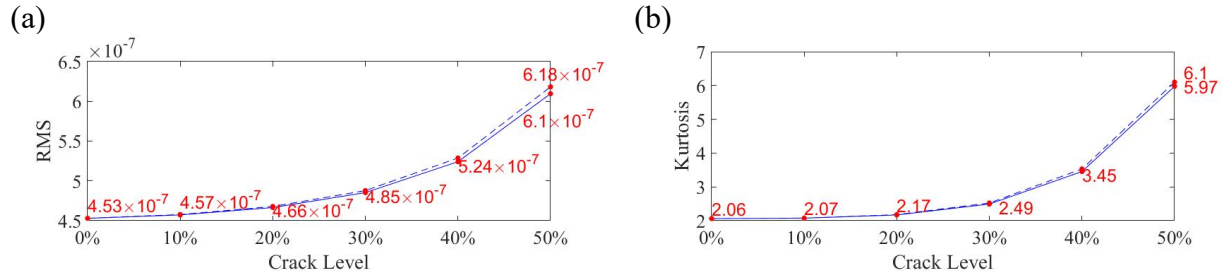


Figure 4.49 (a) RMS and (b) kurtosis of the vibration signal for the planetary gearbox with 0%, 10%, 20%, 30%, 40%, and 50% crack level considering the carrier, sun-gear, and planet-gear bearing clearances.

In conclusion, the effect of the planet-gear bearing clearance can be ignored—only increased by 4% in the sum displacement compared with Figure 4.43(k) and Figure 4.47(k), even considering the sun-gear and planet-gear bearing clearances. The reason is the planet-bearing clearance is much smaller than the displacement of the planet gear, which is discussed in Case 2. The planet-gear, sun-gear, and carrier bearing clearances significantly reduce the highest value of the sum of all displacements by about 57% compared with Figures 4.9(k) and 4.47(k). The sun-gear bearing clearance reduces the magnitude of  $f_m$  by around 50% (from  $1.09 \times 10^{-6}$  to  $0.55 \times 10^{-6}$ ). These results are similar to those of Case 7, in which only the sun-gear and carrier bearing clearances were considered. This means that the planet-gear bearing clearance can be ignored, whereas the carrier and sun-gear bearing clearances must be considered, in future dynamic simulations of gearboxes because the effect of the planet-gear bearing clearance is very small (around 4% in the sum of all displacements, compared with Cases 7 and 8) compared with the effects of the carrier and sun-gear bearing clearances (around 50% in the sum of all displacements, as shown in Case 7).

The next section summarizes the effect of considering all bearing clearances. Then, the following section only compares Case 8 with Case 1 in terms of the RMS and kurtosis index, because the other cases were shown above, and Case 8 is similar to Case 7.

#### 4.5.2. Summary

As mentioned above, the vibration response considering all bearing clearances is similar to the response considering the carrier and sun-gear bearing clearances.

Figure 4.50 illustrates the RMS and kurtosis index of Case 1 and Case 8. As mentioned above, the RMS and kurtosis index are similar in the  $x_g$  and  $y_g$  directions; thus, Figure 4.50 only analyses the  $x_g$  direction. The red line denotes Case 1 without any bearing clearance, and the blue line is for Case 8, which considers the carrier, sun-gear, and planet-gear bearing clearances. The results are as follows: (1) considering all bearing clearances can reduce the RMS index from a 0% to 50% sun-gear crack level (around 55% with a 50% crack level), compared with Figures 4.14(a) and 4.49(a); and (2) considering all bearing clearances can increase the kurtosis index from a 30% to 50% sun-gear crack level (around 10% with a 50% crack level), compared with Figures 4.14(b) and 4.49(b).

In conclusion, the planet-gear bearing clearance can be ignored, even if the carrier and sun-gear bearing clearances are considered, because its influence was found to be very small in this section. Therefore, it is important to consider the sun-gear and carrier bearing clearances in future dynamic simulations of gearboxes because these two clearances can affect the vibration signal of the planetary gearbox mentioned above. Thus, the RMS value is not a suitable index for fault diagnosis of planetary gearboxes considering bearing clearances because it is hard to find an increase trend compared with the kurtosis index shown in Figure 4.50.

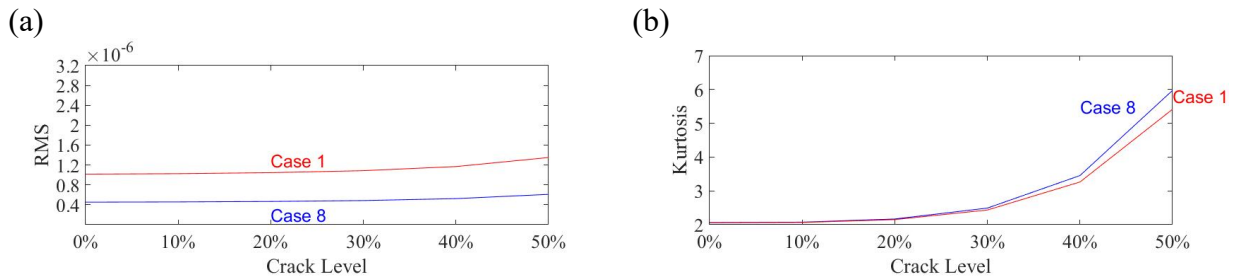


Figure 4.50 (a) RMS and (b) kurtosis of the vibration signal for the planetary gearbox with 0%, 10%, 20%, 30%, 40%, and 50% crack level for Cases 1, 5, 6, and 7.

#### 4.6. Summary and Conclusion

The effects of the bearing clearance of the carrier, sun gear, and planet gear were analysed in this thesis using time-series vibration displacement, vibration frequency, RMS values, and kurtosis indices. This chapter compared different bearing clearance combinations. There are clearances of the sun-gear, planet-gear, or carrier bearings; bearing clearances of the sun gear and planet gear;

bearing clearances of the sun gear and carrier; bearing clearances of the planet gear and carrier; and bearing clearances of the carrier, sun gear, and planet gear. Four results were found, as follows:

- (1) The effect of the bearing clearance for the planet gear, sun gear, and carrier on the vibration displacement was investigated. The planet-gear bearing clearance (0.035 mm) is lower than its displacement (around 0.11 mm); thus, the effect of the planet-gear bearing clearance can be ignored because the highest value for the sum of all displacements of the four planet gears in the  $x$  direction is  $6.2 \times 10^{-6}$  m without a planet-gear bearing clearance and  $6.3 \times 10^{-6}$  m with a planet-gear bearing clearance when the crack level is 50% (only increased by around 1.6%). The sun-gear bearing clearance (0.08 mm) is higher than its displacement (around 0.0001 mm); thus, the sun-gear bearing clearance can affect the vibration displacement. The highest value of the sun-gear displacement in the  $x$  direction increased from  $0.7 \times 10^{-6}$  to  $4.9 \times 10^{-6}$  m after considering the sun-gear bearing clearance. The carrier bearing clearance (0.08 mm) is higher than its displacement (around 0.0003 mm); thus, the carrier bearing clearance can affect the vibration displacement. The highest value of the carrier displacement in the  $x$  direction increased from  $1.2 \times 10^{-6}$  to  $2.8 \times 10^{-6}$  m after considering the carrier bearing clearance.
- (2) The sum of all displacements of all gearbox components at a 50% crack level was investigated. According to the displacement for each component in the planetary gearbox, the sum of all displacements could be increased or reduced. The sun-gear bearing clearance reduces the highest value of the sum displacement by 16%, compared with the cases with the sun-gear bearing clearance and no bearing clearance; the carrier bearing clearance increases the highest value of the sum displacement 1.2 times, compared with the cases considering the carrier bearing clearance and no bearing clearance; the sun-gear and carrier bearing clearances reduce the value of the sum displacement by around 56%, compared with the cases considering the carrier and sun-gear bearing clearances and no bearing clearance.
- (3) The effect of the bearing clearance for the planet gear, sun gear, and carrier in the frequency domain for the sum displacement at a 50% crack level was investigated. The magnitude of  $f_m$  increased 1.2 times after considering the carrier bearing clearance, while the magnitude

of  $f_m$  reduced by 21%. Furthermore, in the dynamic model considering the carrier and sun-gear bearing clearances, the magnitude of  $f_m$  reduced by 56%.

- (4) The RMS and kurtosis indices for the sum displacement were investigated for fault diagnosis. When the crack level increased from 0% to 50%, the RMS and kurtosis indices also increased. The kurtosis index for the carrier and planet-gear bearing clearances is similar to the index of a case without any bearing clearance; the sun-gear bearing clearance increased the kurtosis index before a 30% crack level, while it reduced it from 30% to 50% compared with the cases without any bearing clearance (by around 10% with a 0% crack level); the kurtosis index for the carrier and sun-gear bearing clearances is similar to the index for the case without any bearing clearance before a 30% crack level, while it is increased after a 30% crack level compared with the case without any bearing clearance (by around 10% with a 50% crack level).

In this chapter, we only consider the simulated vibration data of the planetary gearbox, and the bearing clearance is fixed with a constant. In the future, experimental data collected by sensors under different working conditions will be investigated, and we hope the corresponding observations can help researchers gain a better understanding of the vibration mechanism of planetary gearboxes and develop new fault diagnosis strategies.

## Chapter 5

### Summary and Future Work

In this chapter, the summary of the research results regarding the dynamic model of a planetary gearbox considering the sun-gear crack and its effects of clearance for the carrier, planet and sun gear bearings will be drawn firstly, then several potential issues and future work will be described later.

#### 5.1. Summary

This thesis focuses on dynamic modeling for the planetary gearbox with bearing clearance. The main contribution of this thesis includes (1) dynamic modeling for the planetary gearbox considering bearing clearances, (2) the motion equations for the planetary gearbox test-rig used in the Reliability Research Lab at the University of Alberta, and (3) the dynamic effect of sun-gear with different tooth crack levels. The key work done in this research is summarized as follows:

- (1) The planetary gearbox test rig consists of two planetary gearboxes: stage 1 with three planet gears, and stage 2 with four planet gears. The input shaft of both stages of the planetary gearbox are the sun-gear shaft, and the output shaft is a carrier shaft. The ring gears in stage 1 and stage 2 are fixed. In the test rig, the carrier in stage 1 and the sun gear in stage 2 are fixed together, which means they use the same shaft. Therefore, the carrier bearing in stage 1 is seen as the sun-gear bearing in stage 2. In addition, three kinds of bearings in stage 2 are used: carrier bearing, sun-gear bearing, and planet-gear bearing. Furthermore, the operating frequency of the driving motor is fixed at 1200 rpm, which means the rotating frequency of the sun gear in stage 2 is 0.778 Hz, and the mesh frequency in stage 2 is 11.970 Hz, respectively.
- (2) The bearing clearances with respect to carrier bearing, sun-gear bearing, and planet-gear bearing are investigated. The carrier and sun-gear bearings are from Timken, and the planet-gear bearing is from NTN. This thesis only focuses on the minimum value of C0/CN bearing code because the C0/CN is the standard clearance for applications under normal operating conditions. Specifically, the carrier bearing clearance and the sun-gear bearing

clearance are both chosen as 0.035 mm, and the planet-gear bearing clearance is chosen as 0.08 mm.

- (3) The sun-gear tooth crack is investigated. Different crack levels from 0% to 50% with an increment of 0.5% are considered. The 0% means the planetary gearbox is healthy, 0.5% is equal to 0.039 mm crack length, and 50% is equal to 3.90 mm crack length. The sun-gear crack can reduce the sun-planet mesh stiffness, which affects the dynamic modeling.
- (4) The dynamic effect of planetary gearbox associated with bearing clearances is investigated. The bearing clearance (0.035 mm) of the planet gear is approximately 3.2% of the average displacement of the planet gear (1.1 mm), which means that the effect of planet-gear bearing clearance is very low, and only increases by 1.6% highest value for the sum displacement. Then, the clearance of carrier and sun-gear bearing will increase the displacement of the carrier and the sun gear. From this, the carrier bearing clearance increases the highest value of the sum displacement by 1.2 times, and sun-gear bearing reduces by 16% of the highest value for the sum displacement. Therefore, the planet-gear bearing clearance can be ignored, while the carrier and sun-gear bearing clearance should be considered in dynamic modeling. Furthermore, the bearing clearance increases the kurtosis of the sum displacement when the crack level is greater than 30%, specifically from 2.43 to 2.49 for 30% crack level, 3.26 to 3.45 for 40% crack level, and 5.41 to 5.97 for 50% crack level. This means that the kurtosis is an effective condition indicator of fault diagnosis for the planetary gearbox with bearing clearance.

## 5.2. Future work

This thesis investigated the dynamic responses of a planetary gearbox considering the effects of bearing clearances. However, several drawbacks and technical issues of this thesis in the field of dynamic simulation may be investigated and addressed in the future.

- (1) The vibration displacement of the planetary gearbox in stage 1 was not considered in this work. Usually the displacement of the carrier in stage 1 may also affect the displacement of the sun gear in stage 2. Future research may focus on the vibration displacement of the planetary gearbox in stage 1.

- (2) The bearing fault model should be considered. The bearing clearance was typically impacted from the bearing with localized failures, including single fault and multiple faults, thus future studies could focus on simulating the vibration data of the planetary gearbox considering localized failures of bearing through changing the values of bearing clearance.
- (3) The complex transmission path should be considered. The transmission path in the planetary gearbox is more complex than the scope of this thesis. The interior of the gear set contains the air and lubricating oil. When the displacement signal is collected by the sensor mounted on the casing of the gearbox, these substances, such as lubricating oil, make the transmission path complex. Therefore, the research with regards to the transmission path is needed in the future to generate the simulation signal with a complex transmission path.
- (4) The real-world vibration data of the planetary gearbox may be collected and then analysed in the future to make a comprehensive comparison with the simulated vibration data to ensure the validity and engineering practicality of this work.

Beyond the research of dynamic simulation of planetary gearboxes, lab experimental work may be conducted to address the following issues:

- (1) Physical experiments may be conducted to collect vibration responses on a planetary gearbox that has the same parameter values as simulated in this thesis under the same operating conditions simulated in this thesis work. From such future studies, either the validity of the dynamic simulation models reported in this thesis may be confirmed or modification parameters may be discovered to enable the matching between dynamic simulation results and lab experimental results in terms of the responses of a planetary gearbox.
- (2) The findings of the simulation studies reported in this thesis may be used to guide the design of lab experiments so that effective indicators and/or signal processing methods may be developed to help detect early stages of sun gear crack growth.

## Appendix

$$\mathbf{C} = \begin{bmatrix} \mathbf{C}_c \\ \mathbf{C}_r \\ \mathbf{C}_s \\ \mathbf{C}_{p1} \\ \vdots \\ \mathbf{C}_{pn} \\ \vdots \\ \mathbf{C}_{pN} \\ \text{Planet } n \text{ for } n \text{ from } 1 \text{ to } N \end{bmatrix}$$

$$\mathbf{C}_c = \begin{bmatrix} [\mathbf{C}_{cc}]_{3 \times 3} & [0]_{3 \times 6} & \underbrace{[\mathbf{C}_{cp1}]_{3 \times 3} \cdots [\mathbf{C}_{cpn}]_{3 \times 3} \cdots [\mathbf{C}_{cpN}]_{3 \times 3}}_{\text{Planet } n \text{ for } n \text{ from } 1 \text{ to } N} \end{bmatrix}$$

$$\mathbf{C}_r = \begin{bmatrix} [0]_{3 \times 3} & [\mathbf{C}_{rr}]_{3 \times 3} & [0]_{3 \times (3+3N)} \end{bmatrix}$$

$$\mathbf{C}_s = \begin{bmatrix} [0]_{3 \times 6} & [\mathbf{C}_{ss}]_{3 \times 3} & [0]_{3 \times 3N} \end{bmatrix}$$

$$\mathbf{C}_{pn} = \begin{bmatrix} [\mathbf{C}_{ppn}]_{3 \times 3} & [0]_{3 \times 6} & \underbrace{[\mathbf{C}_{cp1}]_{3 \times 3} \cdots [\mathbf{C}_{cpn}]_{3 \times 3} \cdots [\mathbf{C}_{cpN}]_{3 \times 3}}_{\text{Planet } n \text{ for } n \text{ from } 1 \text{ to } N} \end{bmatrix}$$

$$\mathbf{C}_{cc} = \begin{bmatrix} c_{cx} + \sum_{n=1}^N c_{pnx} & 0 & 0 \\ 0 & c_{cy} + \sum_{n=1}^N c_{pny} & 0 \\ 0 & 0 & c_{cu} + \sum_{n=1}^N c_{pnu} \end{bmatrix}$$

$$\mathbf{C}_{cpn} = \begin{bmatrix} -c_{pnx} & 0 & 0 \\ 0 & -c_{pny} & 0 \\ 0 & 0 & -c_{pnu} \end{bmatrix}$$

$$\mathbf{C}_{rr} = \begin{bmatrix} c_{rx} & 0 & 0 \\ 0 & c_{ry} & 0 \\ 0 & 0 & c_{ru} \end{bmatrix}$$

$$\mathbf{C}_{ss} = \begin{bmatrix} c_{sx} & 0 & 0 \\ 0 & c_{sy} & 0 \\ 0 & 0 & c_{su} \end{bmatrix}$$

$$\mathbf{C}_{ppn} = \begin{bmatrix} \sum_{n=1}^N c_{pnx} & 0 & 0 \\ 0 & \sum_{n=1}^N c_{pny} & 0 \\ 0 & 0 & \sum_{n=1}^N c_{pnu} \end{bmatrix}$$

$$\mathbf{K} = \begin{bmatrix} \mathbf{K}_c \\ \mathbf{K}_r \\ \mathbf{K}_s \\ \mathbf{K}_{p1} \\ \vdots \\ \mathbf{K}_{pn} \\ \vdots \\ \mathbf{K}_{pN} \end{bmatrix}$$

Planet  $n$  for  $n$  from 1 to  $N$

$$\mathbf{K}_c = \begin{bmatrix} [\mathbf{K}_{cc}]_{3 \times 3} & [0]_{3 \times 6} & \underbrace{[\mathbf{K}_{cp1}]_{3 \times 3} \cdots [\mathbf{K}_{cpn}]_{3 \times 3} \cdots [\mathbf{K}_{cpN}]_{3 \times 3}}_{\text{Planet } n \text{ for } n \text{ from 1 to } N} \end{bmatrix}$$

$$\mathbf{K}_r = \begin{bmatrix} [0]_{3 \times 3} & [\mathbf{K}_{rr}]_{3 \times 3} & [0]_{3 \times (3+3N)} \end{bmatrix}$$

$$\mathbf{K}_s = \begin{bmatrix} [0]_{3 \times 6} & [\mathbf{K}_{ss}]_{3 \times 3} & [0]_{3 \times 3N} \end{bmatrix}$$

$$\mathbf{K}_{pn} = \begin{bmatrix} [\mathbf{K}_{ppn}]_{3 \times 3} & [0]_{3 \times 6} & \underbrace{[\mathbf{K}_{cp1}]_{3 \times 3} \cdots [\mathbf{K}_{cpn}]_{3 \times 3} \cdots [\mathbf{K}_{cpN}]_{3 \times 3}}_{\text{Planet } n \text{ for } n \text{ from 1 to } N} \end{bmatrix}$$

$$\mathbf{K}_{cc} = \begin{bmatrix} k_{cx} + \sum_{n=1}^N k_{pnx} & 0 & 0 \\ 0 & k_{cy} + \sum_{n=1}^N k_{pny} & 0 \\ 0 & 0 & k_{cu} + \sum_{n=1}^N k_{pnu} \end{bmatrix}$$

$$\mathbf{K}_{cpn} = \begin{bmatrix} -k_{pnx} & 0 & 0 \\ 0 & -k_{pny} & 0 \\ 0 & 0 & -k_{pnu} \end{bmatrix}$$

$$\mathbf{K}_{rr} = \begin{bmatrix} k_{rx} & 0 & 0 \\ 0 & k_{ry} & 0 \\ 0 & 0 & k_{ru} \end{bmatrix}$$

$$\mathbf{K}_{ss} = \begin{bmatrix} k_{sx} & 0 & 0 \\ 0 & k_{sy} & 0 \\ 0 & 0 & k_{su} \end{bmatrix}$$

$$\mathbf{K}_{ppn} = \begin{bmatrix} \sum_{n=1}^N k_{pnx} & 0 & 0 \\ 0 & \sum_{n=1}^N k_{pny} & 0 \\ 0 & 0 & \sum_{n=1}^N k_{pnu} \end{bmatrix}$$

## Bibliography

1. García Márquez, F.P., et al., *Condition monitoring of wind turbines: Techniques and methods*. Renewable Energy, 2012. **46**: p. 169-178.
2. Barszcz, T. and R.B. Randall, *Application of spectral kurtosis for detection of a tooth crack in the planetary gear of a wind turbine*. Mechanical Systems and Signal Processing, 2009. **23**(4): p. 1352-1365.
3. Asian, S., et al., *Wind Turbine Accidents: A Data Mining Study*. IEEE Systems Journal, 2017. **11**(3): p. 1567-1578.
4. Zhi-Ling, Y., et al., *Expert System of Fault Diagnosis for Gear Box in Wind Turbine*. Systems Engineering Procedia, 2012. **4**: p. 189-195.
5. Márquez, F.P.G., et al., *Identification of critical components of wind turbines using FTA over the time*. Renewable Energy, 2016. **87**: p. 869-883.
6. Gray, C.S. and S.J. Watson, *Physics of Failure approach to wind turbine condition based maintenance*. Wind Energy, 2010. **13**(5): p. 395-405.
7. Arabian-Hoseynabadi, H., H. Oraee, and P.J. Tavner, *Failure Modes and Effects Analysis (FMEA) for wind turbines*. International Journal of Electrical Power & Energy Systems, 2010. **32**(7): p. 817-824.
8. Zhou, A., D. Yu, and W. Zhang, *A research on intelligent fault diagnosis of wind turbines based on ontology and FMECA*. Advanced Engineering Informatics, 2015. **29**(1): p. 115-125.
9. Spinato, F., et al. *Reliability of wind turbine subassemblies*. IET Renewable Power Generation, 2009. **3**, 387-401.
10. Igba, J., et al., *Performance assessment of wind turbine gearboxes using in-service data: Current approaches and future trends*. Renewable and Sustainable Energy Reviews, 2015. **50**: p. 144-159.
11. Bouwer Utne, I., *Maintenance strategies for deep - sea offshore wind turbines*. Journal of Quality in Maintenance Engineering, 2010. **16**(4): p. 367-381.
12. Besnard, F. and L. Bertling, *An Approach for Condition-Based Maintenance Optimization Applied to Wind Turbine Blades*. IEEE Transactions on Sustainable Energy, 2010. **1**(2): p. 77-83.
13. Yang, W., et al., *Wind turbine condition monitoring: technical and commercial challenges*. Wind Energy, 2014. **17**(5): p. 673-693.
14. Yang, W., R. Court, and J. Jiang, *Wind turbine condition monitoring by the approach of SCADA data analysis*. Renewable Energy, 2013. **53**: p. 365-376.
15. Qiao, W. and D. Lu, *A Survey on Wind Turbine Condition Monitoring and Fault Diagnosis—Part II: Signals and Signal Processing Methods*. IEEE Transactions on Industrial Electronics, 2015. **62**(10): p. 6546-6557.
16. Tang, B., W. Liu, and T. Song, *Wind turbine fault diagnosis based on Morlet wavelet transformation and Wigner-Ville distribution*. Renewable Energy, 2010. **35**(12): p. 2862-2866.
17. Leahy, K., et al. *Diagnosing wind turbine faults using machine learning techniques applied to operational data*. in *2016 IEEE International Conference on Prognostics and Health Management (ICPHM)*. 2016.

18. Stetco, A., et al., *Machine learning methods for wind turbine condition monitoring: A review*. Renewable Energy, 2019. **133**: p. 620-635.
19. Chen, C., et al. *Fault diagnosis for large-scale wind turbine rolling bearing using stress wave and wavelet analysis*. in *2005 International Conference on Electrical Machines and Systems*. 2005.
20. Teng, W., et al., *Multi-fault detection and failure analysis of wind turbine gearbox using complex wavelet transform*. Renewable Energy, 2016. **93**: p. 591-598.
21. Yang, W., et al., *Bivariate empirical mode decomposition and its contribution to wind turbine condition monitoring*. Journal of Sound and Vibration, 2011. **330**(15): p. 3766-3782.
22. Kusiak, A. and W. Li, *The prediction and diagnosis of wind turbine faults*. Renewable Energy, 2011. **36**(1): p. 16-23.
23. Bartelmus, W., et al., *Modelling of gearbox dynamics under time-varying nonstationary load for distributed fault detection and diagnosis*. European Journal of Mechanics - A/Solids, 2010. **29**(4): p. 637-646.
24. *Automatic Transmissions*. Available from: <http://leakylugnut.com/driveline/automatic-transmissions/>.
25. Rassokha, V. and V. Isaychev, *New Design of the Automobile Automatic Gearbox Providing Driving Simplification and Driver Fatigue Decrease*. Transportation Research Procedia, 2017. **20**: p. 544-549.
26. Guo, Y. and R.G. Parker, *Dynamic modeling and analysis of a spur planetary gear involving tooth wedging and bearing clearance nonlinearity*. European Journal of Mechanics - A/Solids, 2010. **29**(6): p. 1022-1033.
27. Guo, Y., J. Keller, and R.G. Parker, *Nonlinear dynamics and stability of wind turbine planetary gear sets under gravity effects*. European Journal of Mechanics - A/Solids, 2014. **47**: p. 45-57.
28. Chaari, F., T. Fakhfakh, and M. Haddar, *Analytical modelling of spur gear tooth crack and influence on gearmesh stiffness*. European Journal of Mechanics - A/Solids, 2009. **28**(3): p. 461-468.
29. Guo, Y., et al., *Vibration separation technique based localized tooth fault detection of planetary gear sets: A tutorial*. Mechanical Systems and Signal Processing, 2019. **129**: p. 130-147.
30. Gelman, L., et al., *Adaptive vibration condition monitoring technology for local tooth damage in gearboxes*. Insight - Non-Destructive Testing and Condition Monitoring, 2005. **47**: p. 461-464.
31. Chaari, F., T. Fakhfakh, and M. Haddar, *Dynamic analysis of a planetary gear failure caused by tooth pitting and cracking*. Journal of Failure Analysis and Prevention, 2006. **6**(2): p. 73-78.
32. Liang, X., M.J. Zuo, and M.R. Hoseini, *Vibration signal modeling of a planetary gear set for tooth crack detection*. Engineering Failure Analysis, 2015. **48**: p. 185-200.
33. Liu, X., Y. Yang, and J. Zhang, *Resultant vibration signal model based fault diagnosis of a single stage planetary gear train with an incipient tooth crack on the sun gear*. Renewable Energy, 2018. **122**: p. 65-79.
34. Liang, X., M. Zuo, and T. Patel, *Evaluating the Time-Varying Mesh Stiffness of a Planetary Gear Set Using the Potential Energy Method*. Proceedings of the Institution of Mechanical Engineers, Part C: Journal of Mechanical Engineering Science, 2014. **228**: p. 535-547.

35. Liu, L., X. Liang, and M.J. Zuo, *Vibration signal modeling of a planetary gear set with transmission path effect analysis*. Measurement, 2016. **85**: p. 20-31.
36. Guo, Y. and R.G. Parker, *Dynamic Analysis of Planetary Gears With Bearing Clearance*. Journal of Computational and Nonlinear Dynamics, 2012. **7**(4).
37. Dietl, P., J. Wensing, and G.C. van Nijen, *Rolling bearing damping for dynamic analysis of multi-body systems—experimental and theoretical results*. Proceedings of the Institution of Mechanical Engineers, Part K: Journal of Multi-body Dynamics, 2000. **214**(1): p. 33-43.
38. Kim, W., J.Y. Lee, and J. Chung, *Dynamic analysis for a planetary gear with time-varying pressure angles and contact ratios*. Journal of Sound and Vibration, 2012. **331**(4): p. 883-901.
39. Gu, X. and P. Velex, *A dynamic model to study the influence of planet position errors in planetary gears*. Journal of Sound and Vibration, 2012. **331**(20): p. 4554-4574.
40. Chaari, F., et al., *Effect of spalling or tooth breakage on gearmesh stiffness and dynamic response of a one-stage spur gear transmission*. European Journal of Mechanics - A/Solids, 2008. **27**(4): p. 691-705.
41. Liang, X., M.J. Zuo, and M. Pandey, *Analytically evaluating the influence of crack on the mesh stiffness of a planetary gear set*. Mechanism and Machine Theory, 2014. **76**: p. 20-38.
42. Ma, H., et al., *Time-varying mesh stiffness calculation of cracked spur gears*. Engineering Failure Analysis, 2014. **44**: p. 179-194.
43. Lin, J. and R.G. Parker, *Planetary gear parametric instability caused by mesh stiffness variation*. Journal of Sound and Vibration, 2002. **249**(1): p. 129-145.
44. Fernandez del Rincon, A., et al., *A model for the study of meshing stiffness in spur gear transmissions*. Mechanism and Machine Theory, 2013. **61**: p. 30-58.
45. Ambarisha, V.K. and R.G. Parker, *Nonlinear dynamics of planetary gears using analytical and finite element models*. Journal of Sound and Vibration, 2007. **302**(3): p. 577-595.
46. Jia, S. and I. Howard, *Comparison of localised spalling and crack damage from dynamic modelling of spur gear vibrations*. Mechanical Systems and Signal Processing, 2006. **20**(2): p. 332-349.
47. Pandya, Y. and A. Parey, *Failure path based modified gear mesh stiffness for spur gear pair with tooth root crack*. Engineering Failure Analysis, 2013. **27**: p. 286-296.
48. Song, C., C. Zhu, and L. Liu, *Mesh characteristics for marine beveloid gears with crossed axes*. Hsi-An Chiao Tung Ta Hsueh/Journal of Xi'an Jiaotong University, 2012. **46**: p. 64-68+105.
49. Tian, X., M.J. Zuo, and K.R. Fyfe, *Analysis of the Vibration Response of a Gearbox With Gear Tooth Faults*. 2008. p. 785-793.
50. Mathur, T., et al., *Load Distribution and Mesh Stiffness Analysis of an Internal-External Bevel Gear Pair in a Pericyclic Drive*. 2016.
51. Pintz, A., et al., *Dynamic effects of internal spur gear drives*, in NASA. 1983, NASA: Washingto, United States.
52. Kawalec, A., J. Wiktor, and D. Ceglarek, *Comparative Analysis of Tooth-Root Strength Using ISO and AGMA Standards in Spur and Helical Gears With FEM-based Verification*. Journal of Mechanical Design, 2005. **128**(5): p. 1141-1158.

53. Tsai, M.-H. and Y.-C. Tsai, *A method for calculating static transmission errors of plastic spur gears using FEM evaluation*. Finite Elements in Analysis and Design, 1997. **27**(4): p. 345-357.
54. Jian, L., et al., *Comparison of Coaxial Magnetic Gears With Different Topologies*. IEEE Transactions on Magnetics, 2009. **45**(10): p. 4526-4529.
55. Ramamurti, V., N.H. Vijayendra, and C. Sujatha, *Static and dynamic analysis of spur and bevel gears using FEM*. Mechanism and Machine Theory, 1998. **33**(8): p. 1177-1193.
56. Xue, S. and I. Howard, *Torsional vibration signal analysis as a diagnostic tool for planetary gear fault detection*. Mechanical Systems and Signal Processing, 2018. **100**: p. 706-728.
57. Chen, Z., Z. Zhu, and Y. Shao, *Fault feature analysis of planetary gear system with tooth root crack and flexible ring gear rim*. Engineering Failure Analysis, 2015. **49**: p. 92-103.
58. Yang, D.C.H. and J.Y. Lin, *Hertzian Damping, Tooth Friction and Bending Elasticity in Gear Impact Dynamics*. Journal of Mechanical Design, 1987. **109**(2): p. 189-196.
59. Meagher, J., et al. *A Comparison of Gear Mesh Stiffness Modeling Strategies*. 2011. New York, NY: Springer New York.
60. Zhou, X., W. Wu, and H. Ma, *A Contraction Fixed Point Theorem in Partially Ordered Metric Spaces and Application to Fractional Differential Equations*. Abstract and Applied Analysis, 2012. **2012**: p. 11.
61. Liu, L., X. Liang, and M.J. Zuo, *A dependence-based feature vector and its application on planetary gearbox fault classification*. Journal of Sound and Vibration, 2018. **431**: p. 192-211.
62. Wu, S., M.J. Zuo, and A. Parey, *Simulation of spur gear dynamics and estimation of fault growth*. Journal of Sound and Vibration, 2008. **317**(3): p. 608-624.
63. Yang, D.C.H. and Z.S. Sun, *A Rotary Model for Spur Gear Dynamics*. Journal of Mechanical Design, 1985. **107**(4): p. 529-535.
64. Kahraman, A., *Load sharing characteristics of planetary transmissions*. Mechanism and Machine Theory, 1994. **29**(8): p. 1151-1165.
65. *NTN Bearing Internal Clearance and Preload*. Available from: [https://www.ntnglobal.com/en/products/catalog/pdf/2202E\\_a08.pdf](https://www.ntnglobal.com/en/products/catalog/pdf/2202E_a08.pdf).
66. Kahraman, A. and R. Singh, *Interactions between time-varying mesh stiffness and clearance non-linearities in a geared system*. Journal of Sound and Vibration, 1991. **146**(1): p. 135-156.
67. Guo, Y., J. Keller, and W. LaCava, *Combined Effects of Gravity, Bending Moment, Bearing Clearance, and Input Torque on Wind Turbine Planetary Gear Load Sharing: Preprint*. Conference: To be presented at the American Gear Manufacturers Association; (AGMA) Fall Technical Meeting, 28-30 October 2012, Dearborn, Michigan. 2012: ; National Renewable Energy Lab. (NREL), Golden, CO (United States). Medium: ED; Size: 21 pp.
68. *SKF internal clearance*. Available from: <https://www.skf.com/ca/en/products/bearings-units-housings/roller-bearings/spherical-roller-bearings/split-spherical-roller-bearings/internal-clearance/index.html>.
69. Qiu, X., Q. Han, and F. Chu, *Load-sharing characteristics of planetary gear transmission in horizontal axis wind turbines*. Mechanism and Machine Theory, 2015. **92**: p. 391-406.
70. *Timken spherical roller bearing catalog*. Available from: [https://www.timken.com/pdf/10446\\_SRB%20Catalog.pdf](https://www.timken.com/pdf/10446_SRB%20Catalog.pdf).

71. *NTN Technical Information Series*. Available from: <http://www.ntnamericas.com/en/pdf/2200/brgclear.pdf>.
72. Mohammed, O.D., *Dynamic Modelling and Vibration Analysis for Gear Tooth Crack Detection*, in *Doctoral thesis*. 2015, Luleå tekniska universitet.
73. Protter, M.H. and C.B. Morrey, *College calculus with analytic geometry*. 1977: Addison-Wesley.